




This is to certify that the
thesis entitled
ULTRASONIC BLOOD FLOW IMAGING
USING CORRELATION PROCESSING

presented by

Michael De Olinger

has been accepted towards fulfillment
of the requirements for

Ph.D. degree in Elec. Engr. &
Sys. Sci.


Major professor

Date March 12, 1981



OVERDUE FINES:

25¢ per day per item

RETURNING LIBRARY MATERIALS:

Place in book return to remove
charge from circulation records

ULTRASONIC BLOOD FLOW IMAGING
USING CORRELATION PROCESSING

By
Michael De Olinger

A DISSERTATION

Submitted to
Michigan State University
in partial fulfillment of the requirements
for the degree of

DOCTOR OF PHILOSOPHY

Department of Electrical Engineering and Systems Science

ABSTRACT

ULTRASONIC BLOOD FLOW IMAGING USING CORRELATION PROCESSING

By

Michael De Olinger

A general investigation of those fundamental processes affecting the design of ultrasonic blood flow imaging instruments is presented. First, known physical attributes of the various biological tissues are combined to formulate a simple model which describes the interaction of ultrasound with the human body. Using this model, it is shown that a periodic pulse train is the preferred transmitted signal and that significant performance improvement may be realized by implementing "true" correlation as opposed to the conventional correlation processing.

The desirability of having the true correlation receiver operate in a near optimum manner is demonstrated and the constraints imposed on signal bandwidth, effective signal duration, achievable velocity resolution and transducer angle are presented. In order to present the complex interrelationships which exist between these constraints, a unique set of design curves were generated. These curves indicate those combinations which insure near optimality. Also, the constraints imposed by transducer limitations are discussed. The transducers which are examined include the traditional piston type (both focused and unfocused) and the array type, as well as a newly developed dual element transducer.

Finally, these results are utilized in an example system design where implementation difficulties and system limitations are discussed.

To make this dissertation as self contained as practical, a rather complete tutorial on detection and estimation theory, as it applies to the blood flow measurement problem, is presented in the Appendices.

ACKNOWLEDGMENTS

So many people have contributed in so many ways that it is difficult to acknowledge all of them. However, it is a pleasure to acknowledge those few individuals whose valuable contributions deserve special recognition.

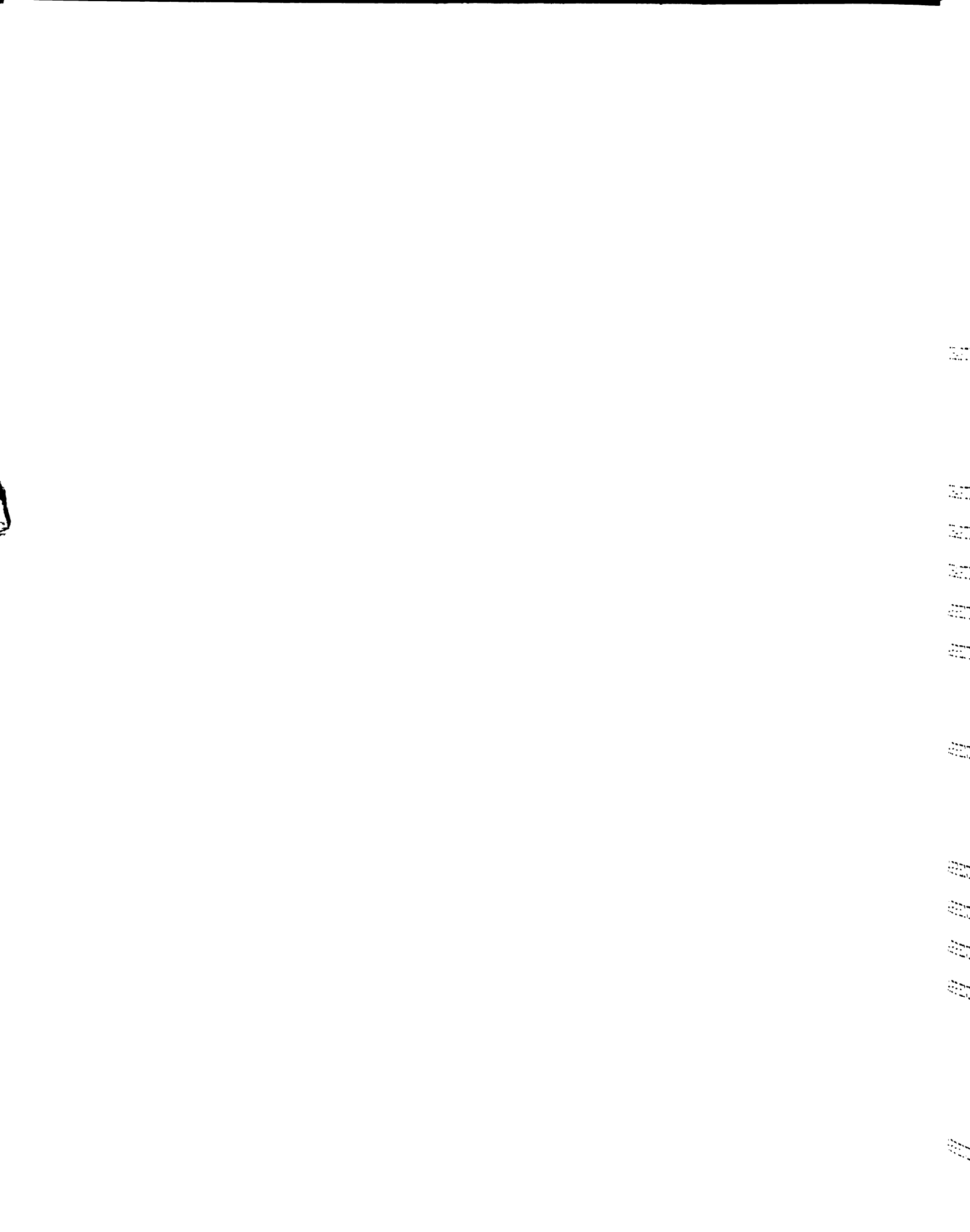
The academic guidance and technical criticism provided by Dr. Marvin Siegel is especially appreciated as is the continual encouragement of Dr. Bong Ho.

Much of the initial draft was typed by Cindy Turner while the final manuscript was type by Donna Ahrens. Their efforts are sincerely appreciated.

Finally, I would like to thank the members of my family for their patience and support. Especially my mother, father, and my wife Marcia.

TABLE OF CONTENTS

CHAPTER I. INTRODUCTION	1
CHAPTER II. BACKGROUND	6
Transmission Type Ultrasonic Flowmeters	6
Conventional Reflection Type Ultrasonic Flowmeters	7
Conventional Pulsed Doppler Systems	8
Random Signal System	9
Conventional Reflection Type Visualization Systems	10
Velocity Imaging Systems	10
Early Experimental Results	12
CHAPTER III. TARGET MODEL	18
Measurement Objective	19
General Measurement Method	19
Physical Structure	21
Target Definition and Characterization	29
Simple Tissue Model	40
CHAPTER IV. SIGNAL CONSIDERATIONS	48
Desirable Signal Characteristics	48
Signal Selection	49
CHAPTER V. PROCESSING CONSIDERATIONS	73
Transit Time Effects	73
Derivation of the Optimum Detector in the Presence of Transit Time Effects	79



Performance of the Optimum Detector in the Presence of Transit Time Effects	89
Performance of the Correlation Detector in the Presence of Transit Time Effects	95
Constraints on the Correlation Receiver for Near Optimality	101
Resolving Capability of Both True and Conventional Correlation Receivers	107
CHAPTER VI. RESOLUTION CONSTRAINTS AND RECEIVER PERFORMANCE	119
Resolution Constraints	119
Receiver Performance	130
CHAPTER VII. TRANSDUCER CONSIDERATIONS	136
CHAPTER VIII. SYSTEM IMPLEMENTATION	149
CHAPTER IX. SUMMARY AND CONCLUSIONS	161
APPENDIX A. Vector Representation of Signals	168
APPENDIX B. Complex Signal Notation for Narrowband Processes	171
Complex Representation of Transfer Functions	177
APPENDIX C. Bandpass Random Processes	179
Complex White Process	184
Complex Gaussian Process	185
APPENDIX D. Hypothesis Testing for Bloodflow Imaging	189
APPENDIX E. Estimation Theory	207
APPENDIX F. Detection of a Point Target	210
APPENDIX G. Ambiguity Functions	216
Generalized Ambiguity Functions	216
Doppler Approximation	218
Ambiguity Function	222
APPENDIX H. Acoustic Wave Propagation	229

APPENDIX I. Blood Flow in Cylindrical Vessels	236
APPENDIX J. Computation of the Elements of A	239
LIST OF REFERENCES	243
GENERAL REFERENCES	247

LIST OF FIGURES

Figure 2.1	Simplified Blood Flow Imaging System	11
Figure 2.2	The Blood Flow Simulation System	13
Figure 2.3	Experimental Velocity Measuring System	14
Figure 2.4	Flow Profile Across Unobstructed 7mm Tube	15
Figure 2.5	Actual Spectrum Analyzer Output at Selected Positions Along the Diameter of a 7mm Tube	16
Figure 3.1	General Measurement Method	20
Figure 3.2	Stratified Squamous Epithelial Tissue	22
Figure 3.3	Muscle Tissue	22
Figure 3.4	Typical Flow vs Time in the Aorta	27
Figure 3.5	Target Definition	32
Figure 3.6	System Geometry	33
Figure 3.7	Typical Relative Range Scattering Function	45
Figure 4.1	Ambiguity Function for a Single Pulse	51
Figure 4.2	Ambiguity Function for Random Noise	53
Figure 4.3	A Typical Feedback Shift Register	54
Figure 4.4	Average Ambiguity Function for a PN Sequence	56
Figure 4.5	Periodic Pulse Train	58
Figure 4.6	Approximate Ambiguity Function for a Periodic Pulse Train	60
Figure 4.7	Periodic Train of PN Sequences	62
Figure 4.8	Geometry for Clutter Computations	65
Figure 5.1	Target and Beam Geometry	75

Figure 5.2	Optimum Detector	80
Figure 5.3	Approximate $\Lambda_p(\beta \frac{\lambda}{T})$	84
Figure 5.4	Correlation Detector	95
Figure 5.5	Correlated Energy Function	99
Figure 5.6	Maximum Normalized Eigenvalue of A	103
Figure 5.7	Conventional Correlation Receiver Operation	108
Figure 5.8	True Correlation Receiver Operation	113
Figure 5.9	Typical Doppler Resolution Plot	116
Figure 6.1	System Signal Processor	120
Figure 6.2	Bloodflow Doppler Profile Target Interaction	123
Figure 6.3	Design Curves for $f_c = 5$ MHz, $D = 1$ cm	128
Figure 6.4	Design Curves for $f_c = 3$ MHz, $D = 1$ cm	128
Figure 6.5	Design Curves for $f_c = 5$ MHz, $D = .5$ cm	129
Figure 6.6	Design Curves for $f_c = 3$ MHz, $D = .5$ cm	129
Figure 6.7	Probability of Error Curves	135
Figure 7.1	Basic Piezoelectric Transducer	137
Figure 7.2	Typical Beam Profile	140
Figure 7.3	A Focused Beam Profile	142
Figure 7.4	Dual Element Transducer	143
Figure 7.5	Annular Ring Beam Pattern	145
Figure 7.6	Typical Transducer Array	146
Figure 7.7	Generalized Array Beam Pattern	147
Figure 8.1	Expected Output of a Two Correlator System	151
Figure 8.2	Effect of Doubling the Number of Correlators	151
Figure 8.3	Bandpass Correlator	154
Figure 8.4	Blood Flow Imaging System	157

Figure A1.	Typical Sample Function From a Random Process	168
Figure B1.	Typical Signal Spectrum	173
Figure B2.	Spectrum of Complex Envelope	174
Figure B3.	Sample On/Off Sequence	175
Figure B4.	Sample Binary-Phase Sequence	176
Figure B5.	Symmetric $[S(f - f_c)]_{LP}$	176
Figure B6.	Example of a Narrowband Transfer Function	177
Figure C1.	Example of a Complex Envelope Spectrum	180
Figure C2.	Example of Band Limited White Noise	184
Figure C3.	Spectrum of $w_B(t)$	184
Figure D1.	Correlator Implementation	191
Figure D2.	Matched Filter Implementation	191
Figure D3.	Typical Receiver Operating Characteristics	195
Figure D4.	Optimum Detector Implementation	202
Figure D5.	Filter Correlator Optimum Receiver	203
Figure D6.	Optimum Receiver for N_0 Near Zero	205
Figure D7.	Optimum Receiver for Random Amplitude and Phase	206
Figure D8.	Bandpass Processing for Case 2	206
Figure G1.	Example of Compression in Binary Phase Signals	219
Figure G2.	Approximate General Ambiguity Surface	226
Figure H1.	One Quarter Wave Matching Layer	234
Figure I1.	Section of Cylindrical Vessel	236

LIST OF TABLES

Table 4.1	$\theta'(0, fT)$ For a Periodic Pulse Train	72
-----------	---	----

CHAPTER I

INTRODUCTION

Currently there is widespread interest in developing instrumentation capable of non-invasively measuring various cardiovascular system parameters. Included are such parameters as mean volume flow rate, blood velocity, condition of the blood vessel walls and the presence of partial or complete occlusions.

In the past, such techniques as Fick and other dilution methods, angiographic techniques, and attaching electromagnetic flowmeters directly to the vessel of interest have been employed. These methods have severe limitations since they are physically invasive, expensive to perform, limited in the number of repeated applications, and there exists an attendant risk. Ultrasound has been suggested as a non-invasive alternative to these methods.

Specifically, an ultrasonic system capable of displaying and/or measuring the velocity of the flowing blood as a function of position within the vessel could provide the physician with important quantitative, as well as qualitative, information on the condition of the patient's cardiovascular system. Many ultrasonic systems which will be

described in the next chapter have been proposed to provide this information. The primary difference between these systems is in the particular choice of transmitted signal, or in the technique employed to implement the signal processing. Fundamentally however, each of these systems employ some form of correlation detection. The research reported in this dissertation theoretically examines the feasibility of implementing a practical Blood Flow Imaging System employing correlation processing.

In the large majority of cases, research can be grossly classified as basic or applied, with a poorly defined line dividing the two. Paradoxically, however, the research reported herein may be best classified as both. In the most general terms, this research examines the fundamental nature of those physical attributes and signal processing techniques which significantly affect the design of a correlation type blood flow imaging system. Because this research covers relatively uncharted ground and because of its complex nature and scope, it is difficult to separate those processes and procedures which should be investigated from those that should not. Therefore, in an effort to prevent the scope of this investigation from becoming unmanageable, the central theme of designing a practical system has been adopted. Although this is a highly visible theme in this dissertation, it is also superficial to a more subtle underlying purpose. The true value of this research lies in the insight gained into the fundamental processes affecting the system design

so that readers might be better equipped to make their own engineering judgement in designing their own system.

The various phases of the research are listed below in the order that they are presented in the text. Each phase constitutes a major portion of work in the investigation of ultrasonic blood velocity imaging.

1. Background: This section presents a brief history of previous work relevant to the work presented in this dissertation. A simplified block diagram of the velocity imaging system is presented and discussed in this section.
2. Development of a Model: In this section a model for the flowing blood as a "target" is developed. Additionally, a characterization of the surrounding tissue (target environment) is presented.
3. Signal considerations: An investigation of the potential advantages and limitations of utilizing various large time bandwidth product signals is carried out in this section. Based on these results and practical considerations, a particular signal is selected.
4. Processing Considerations: Under certain constraints on the transmitted signal, the correlation receiver can be considered near optimum. These constraints are derived and discussed in this chapter.

5. Resolution Constraints and Receiver Performance:

Various complex resolution interrelationships which affect the design of an optimum flow measurement system are derived and discussed in this chapter. Additionally, theoretical receiver performance is evaluated.

6. Transducer Considerations: At this point, a discussion of various transducer designs is included. This discussion includes results of a specially designed dual element transducer developed by Jethwa, as well as more conventional focused and unfocused transducers.

7. System Implementation: In this chapter, real world considerations are included in an example system design. Most of the ideas presented in the example are the result of experience gained in the actual hardware construction of a similar system.

8. Finally, a brief conclusion section is included to summarize the research and comment on the implications of some of the results.

Additionally, the required detection/estimation theory background is developed in Appendices A through G. Since the theory is developed in the context of the blood flow imaging problem, the reader is strongly advised to at least skim these Appendices before reading the main text. They are very

much a part of the total effort, and it will be assumed in
the main body that the reader has developed the necessary
familiarity.

CHAPTER II

BACKGROUND

In the past, several different techniques from plethysmography to NMR (nuclear magnetic resonance) have been used for the detection and measurement of blood flow. The major difficulty with these methods is the lack of ability to measure flow in a specific region. Ultrasonic techniques do not experience this problem and are only limited by the resolution and accuracy designed into the instrumentation and processing. Hence, ultrasound is ideally suited for medical diagnosis and treatment, as well as, medical research. A number of excellent surveys of various ultrasonic blood flowmeters have been published by Franklin,¹ Wells,² Baker,³ and Fry⁹.

Transmission Type Ultrasonic Flowmeters

Many transmission-type flowmeters have been designed.¹⁰⁻¹⁸ These flowmeters are based on the principal that a sound beam passed diagonally through a blood vessel exhibits a difference in the time required to traverse the vessel alternately in the upstream and downstream directions. A major disadvantage associated with these flow detectors is that surgery must be performed to locate the transducer close to the blood vessel

being examined. Thus, these flowmeters are not suitable for transcutaneous blood velocity measurements.

Conventional Reflection Type Ultrasonic Flowmeters

The conventional reflection-type flowmeters, which are in common use, are based on the principle of the Doppler effect. When ultrasound is transmitted into the blood stream a portion of the signal is scattered by the moving blood particles and is Doppler shifted. The relationship between the average Doppler difference frequency f_d and the average blood flow velocity v , is given by the following equation^{2,19}

$$v = \frac{c f_d}{f_c \{\cos \alpha + \cos \beta\}} \quad 2.1$$

where c is the velocity of ultrasound in blood, f_c is the transmitted ultrasonic frequency, and α and β are the angles between the transmitting and receiving ultrasonic transducers and the velocity vector of the blood stream.

Reflection type devices may operate in the continuous wave mode or the more sophisticated pulsed Doppler mode. Satomura²⁰ was the first to demonstrate continuous wave Doppler motion detection in 1956. Franklin, et al²¹ used this technique for blood velocity detection in animals. Baker²² developed a practical instrument for the transcutaneous detection of blood flow in humans.

Conventional Pulsed Doppler Systems

The early continuous wave flowmeters were not capable of detecting the direction of the blood velocity vector with respect to the transducer. In 1966, McLeod²³⁻²⁴ used a version of quadrature phase detection to demonstrate the first successful direction sensing Doppler device. One of the shortcomings of the continuous wave (CW) sinusoidal systems is its inability to obtain a measurement of range. This lack of range sensitivity prevents the measurements of vessel diameter and velocity profiles. The current pulsed Doppler systems by Baker, Perroneau, and others³⁻⁸ and the Random Signal Systems by Newhouse²⁵ and Jethwa²⁶ were developed in an attempt to make transcutaneous blood flow measurements.

In the pulsed Doppler system, a burst of ultrasound is transmitted. The distance to the moving target and the target's velocity with respect to the ultrasonic beam are determined by range-gating the return echoes. These received echoes are both phase and amplitude modulated by the moving target. This range-gated echo is then compared with a sample of the original transmitted signal in a phase detector to extract the Doppler components. A number of these systems have been built and used for measuring blood velocity³⁻⁸.

As will be discussed in the next chapter, one of the concerns with a conventional Doppler system is providing

sufficient energy in the pulse to enable targets of interest to be easily detected, simultaneously with providing sufficient range resolution (obtained by using shorter duration pulses). A conventional system increases transmitted energy by increasing the peak energy in each pulse, thus improving the system immunity to noise. However, there is presently some concern about the safe peak intensity levels for tissues^{25,26}.

Random Signal System

One potential solution to the peak power problem associated with conventional Doppler systems lies in the use of random noise as the transmitted signal. Using random noise, a duty cycle of 100% may be utilized without degrading the systems range resolving capability. Also, the signal may be pulsed modulated and transmitted at an arbitrarily high repetition rate without introducing range ambiguities. (Those concepts will be treated in detail in Chapter Four.)

The random signal system proposed by Newhouse and by Jethwa were attempts to utilize random noise in this fashion. Also, it was speculated by these researchers that the random signal system could theoretically provide arbitrarily good velocity and range resolution.

Conventional Reflection Type Visualization Systems

Conventional reflection type ultrasonic visualization systems provide cross sectional presentations of static targets (tissue, muscle, bone, etc.) These systems transmit a series of narrow pulses of ultrasound. A portion of the transmitted energy is reflected from any acoustical impedance discontinuity (tissue interface) and received by the receiving transducer. The received signal is amplified and envelope detected. An image is then formed on a CRT by scanning properly and intensity modulating according to the energy in the received signal.

Velocity Imaging Systems

A second form of a visualization system is the presentation of dynamic (moving) targets, or Doppler visualization. In the special case where red blood cells are the moving targets, the system will be referred to as a Blood Flow Imaging System.

A simplified block diagram of a Blood Flow Imaging System is shown in Figure 2.1. As shown in the block diagram, the signal to be transmitted is generated by the signal generator, amplified by the power amplifier, and converted to an acoustical signal by the transmitting transducer. The ultrasonic energy is then reflected by a continuous stream of moving red blood cells in the flowing blood as well as

surrounding tissue. The signal received by the receiving transducer is amplified and processed to provide a velocity estimate corresponding to each spatial location.

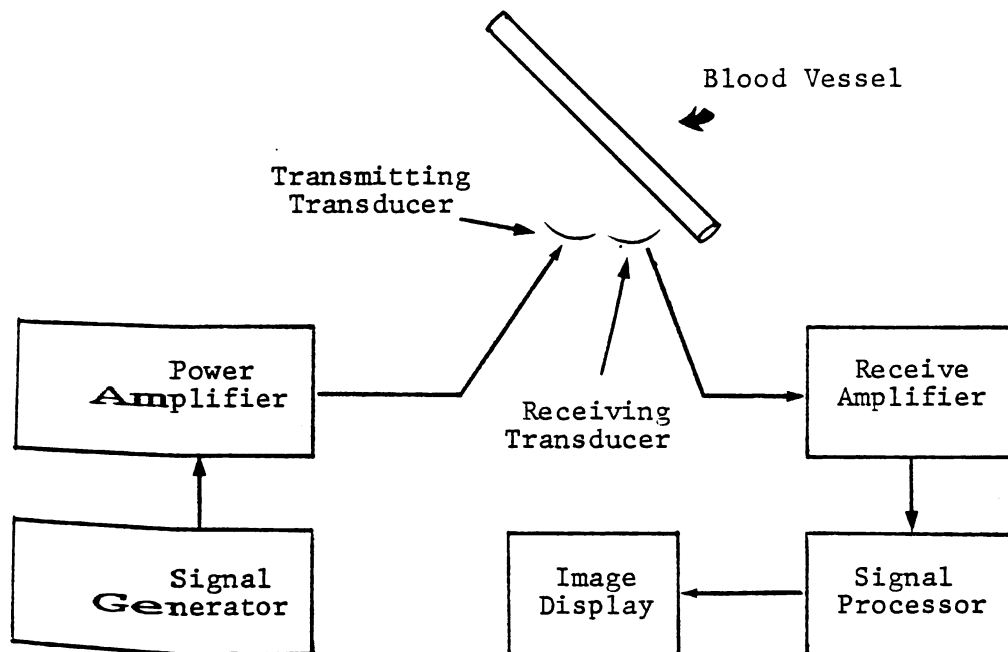


Figure 2.1 Simplified Blood Flow Imaging System

Some limited success has been reported in the area of Blood Flow Imaging²⁷. However, very little work has been done in investigating fundamental limitations, system constraints, appropriate transmitted signals, or optimum processing and the associated performance.

This investigation was an outgrowth of a desire to understand more clearly those fundamental processes involved

in Ultrasonic Blood Velocity Imaging.

Early Experimental Results

Initially, the purpose of this research was to exploit the suggested advantages of the random signal system in making blood velocity measurements. As a result, a flow measurement system was constructed which was capable of comparing the performance of the random signal flowmeter with the more conventional pulsed sinusoid system. Additionally, a blood flow simulation system was constructed so that in-vitro measurements could be made.

Figure 2.2 shows the physical construction of the blood flow simulation system. Seven millimeter dialysis tubing was used to simulate blood vessels of the size most likely to be encountered in practice. The length of the tube was chosen as approximately 100 times the diameter of the tube so that laminar time independent flow could be guaranteed in the exposed section. Also, as shown, this construction allowed for the introduction of obstructions into the tubing. G. E. Antifoam containing seven micron silicon particles was mixed with distilled water to simulate actual blood.

The block diagram of the experimental system which was constructed is shown in Figure 2.3. As shown, the transmitted signal consisted of either a sample function from a random noise source or a pulsed sinusoid. A portion of the transmitted signal is delayed by the variable acoustic delay

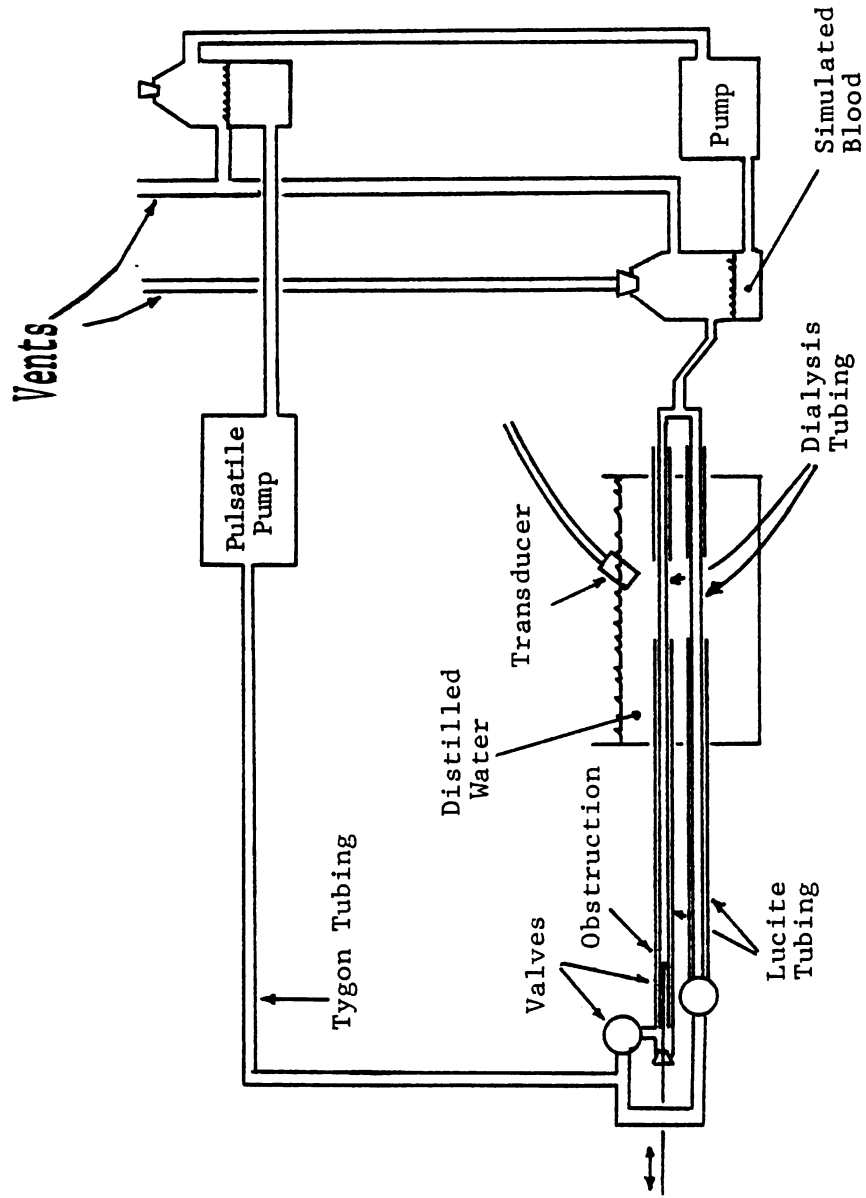


Figure 2.2 The Blood Flow Simulation System

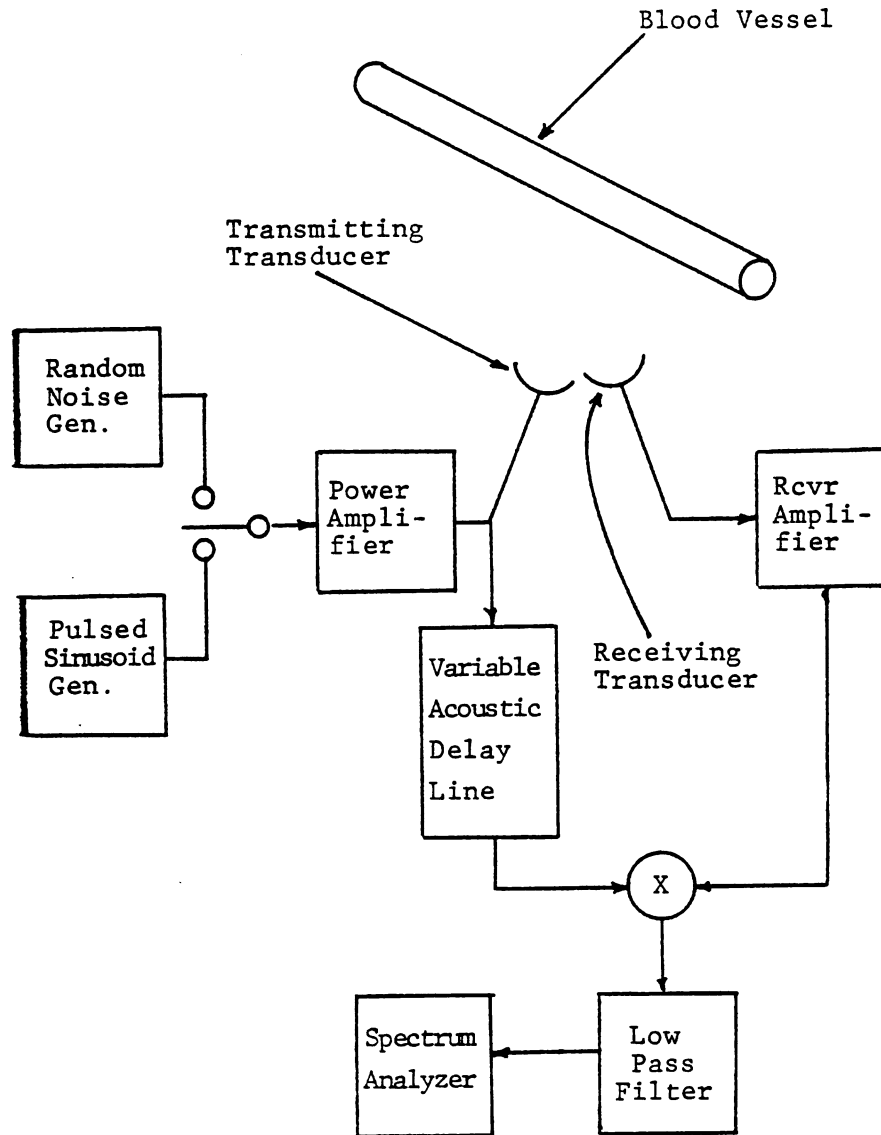


Figure 2.3 Experimental Velocity Measuring System

line and then mixed with the received signal. The output of the mixer is low pass filtered and its frequency content analyzed by a digital spectrum analyzer. The range under examination is determined by the delay introduced into the reference signal by the delay line.

Figure 2.4 shows a typical velocity profile reconstructed from Doppler spectra obtained using the experimental system^{38,39}. The actual spectrum analyzer output corresponding to a few selected positions across the vessel diameter is shown in Figure 2.5.

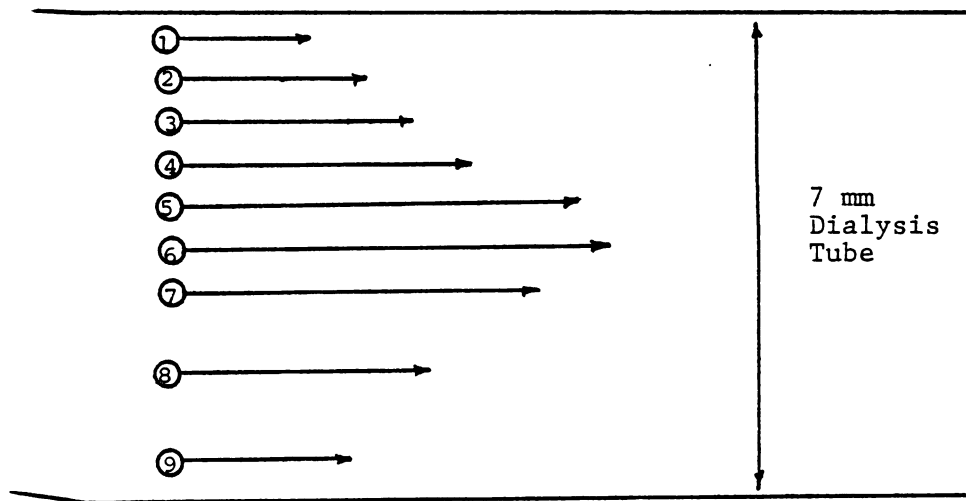


Figure 2.4 Flow Profile Across Unobstructed 7 mm Tube

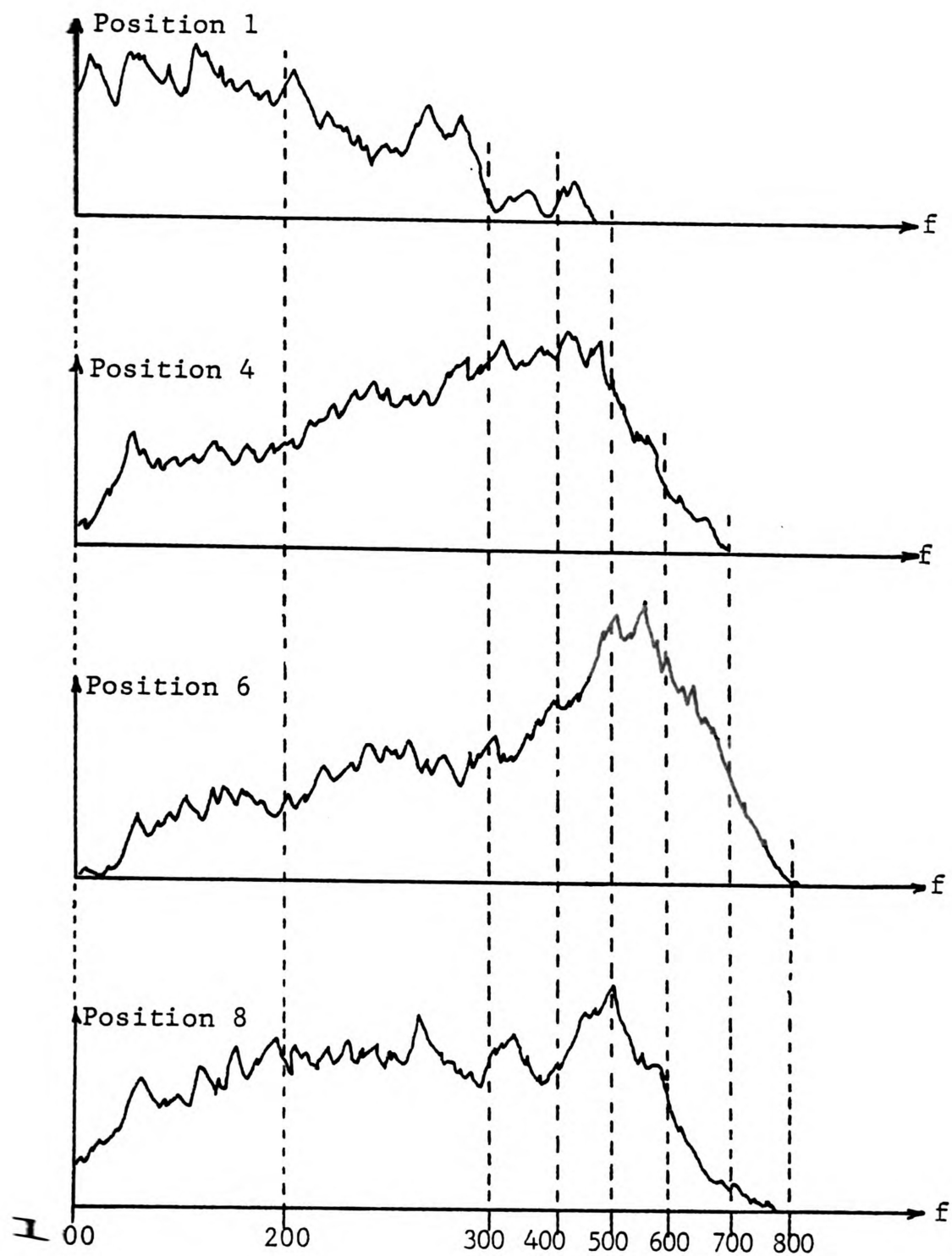


Figure 2.5 Actual Doppler Spectrum Analyzer Output
at Selected Positions Along the Diameter
of a 7 mm Tube

These spectra were obtained using random noise as the transmitted signal by averaging the output spectra over several seconds. When long time averaging was not used, the Doppler spectra were virtually uninterpretable. Even with averaging, the difficulty in reconstructing a profile from them is apparent. Clearly, long time averaging cannot be tolerated in-vivo where pulsatile flow exists. Nearly identical results were obtained when a pulsed sinusoid was used as the transmitted signal.

These results indicated that the range and velocity resolutions of the random signal system were comparable to those of the existing conventional ultrasonic Doppler systems, but not superior as had been anticipated. Additionally, although the in-vitro results indicated that similar system performance could be expected, in-vivo results were quite different. Using random noise, not a single meaningful measurement was ever accomplished. On the other hand, obtaining in-vivo measurements using the conventional system were a matter of routine.

It was this combination of failures on the part of the random signal system which was to become the seed of this research. It became apparent that a more fundamental understanding of the processes involved in making in-vivo blood flow measurements was required.

CHAPTER III

TARGET MODEL

In this chapter, a model for the flowing blood as a **target** is presented and discussed. In the sequel, the word **model** is intended to mean a mathematical characterization of a **physical target** which is consistent with the measurement **methods** and objectives. From this characterization (model), **various** performance measures and design parameters may be **analyzed** and optimized according to the measurement **objectives**. However, before such a characterization is completed a **clear** understanding and/or definition of the following is **required**:

1. Measurement objective
2. General measurement method to be employed
3. Actual physical structure of the system upon which measurements are being made and its effects on the measurement method.

Therefore, the development of an actual mathematical characterization must be preceded by a discussion of each of the **topics** listed above.

After defining the general measurement method and **objective** as well as describing the important attributes of **the** physical system, this chapter addresses the problem of

formulating a model for the flowing blood. Additionally, a simple model for the surrounding tissue is presented. Thus, the final two sections of this chapter are:

4. Target Definition and Characterization
5. Simple Tissue Model

Measurement Objective

The objective of the ultrasonic flow visualization system is to display, as a function of time and as accurately as possible, the velocity of scatterers at each spatial location in the field of observation. Unfortunately, as will become apparent, the simultaneous achievement of good spatial, velocity and time resolution are conflicting requirements.

Therefore, it is difficult, if not impossible, to specify a single criteria which provides a measure of overall system capability. However, a unique set of design curves will be presented in a later chapter which suggest a design methodology to meet the measurement objectives of any specific application.

General Measurement Method

The general measurement method employed in this research is shown pictorially in Figure 3.1. As indicated, electrical signals are converted to propagating acoustic waves by the transmitting transducer. These waves are then alerted (scattered, attenuated, distorted, etc.) by the internal structures

of the human body. A portion of the altered transmitted waves are received by the receiving transducer and converted to electrical signals. These signals are then processed in the true correlation receiver to provide information related to the measurement objective. The only further restriction imposed on the general method is to constrain the transmitting and receiving transducers to occupy the same spatial location and orientation.

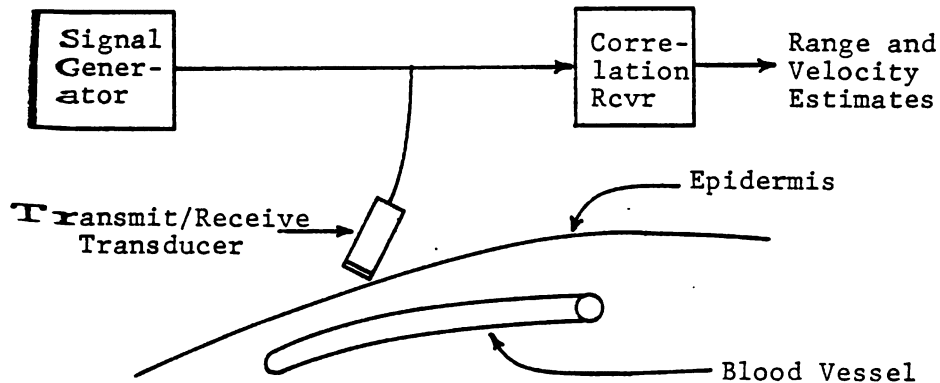


Figure 3.1 General Measurement Method

It should be pointed out that this choice of general measurement method is based on the author's, and other's, experiences as described previously in the introduction. And it is the purpose of this research to further exploit the advantages of this measurement scheme.

Physical Structure

The actual physical structure which the measurement system must interface with is the human body. Simply stated, the human body consists of an almost endless number of microscopic cells, each performing specific functions which are integrated for maintenance of the entire being. Primarily, there are four types of cells, which group together in a regular fashion to form the four general tissue types:

1. Epithelial
2. Muscle
3. Connective
4. Nerve
5. Blood

For example, Figure 3.2 shows how epithelial cells group together to form stratified tissue, while Figure 3.3 shows how smooth muscle cells group to form muscles.

Since tissue is composed of similar cells organized in an orderly fashion, it is reasonable to expect the acoustic properties of a given tissue to be nearly homogeneous. (See Appendix H for a brief discussion of acoustic waves.) Also, one might expect the acoustic properties of dissimilar tissues to be dissimilar. In fact, all reflection type ultrasonic tissue visualization systems are based on the fact that different tissue types provide different characteristic acoustic impedances and the fact that reflection occurs at the acoustic impedance discontinuities present at tissue interfaces. At

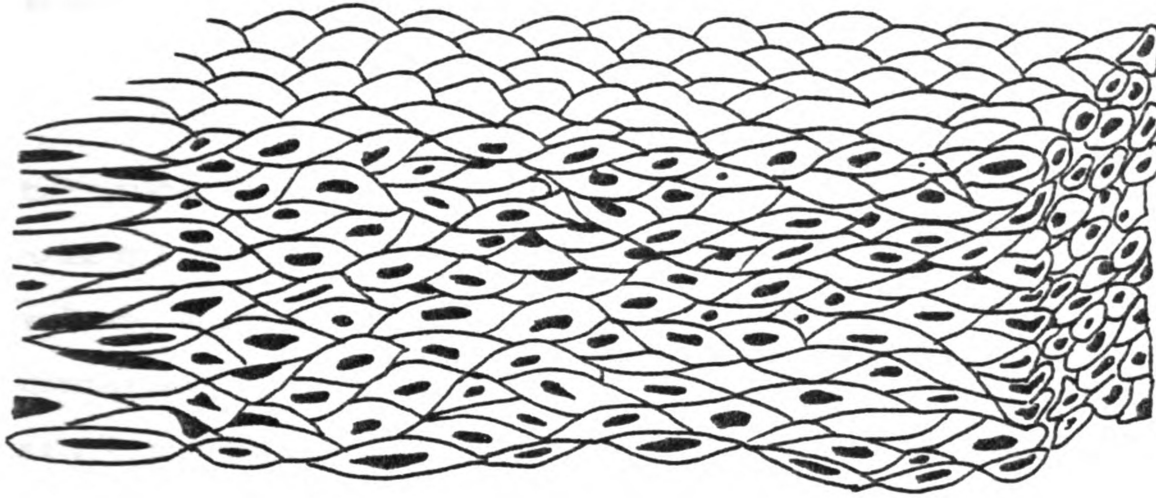


Figure 3.2 Stratified Squamous Epithelial Tissue

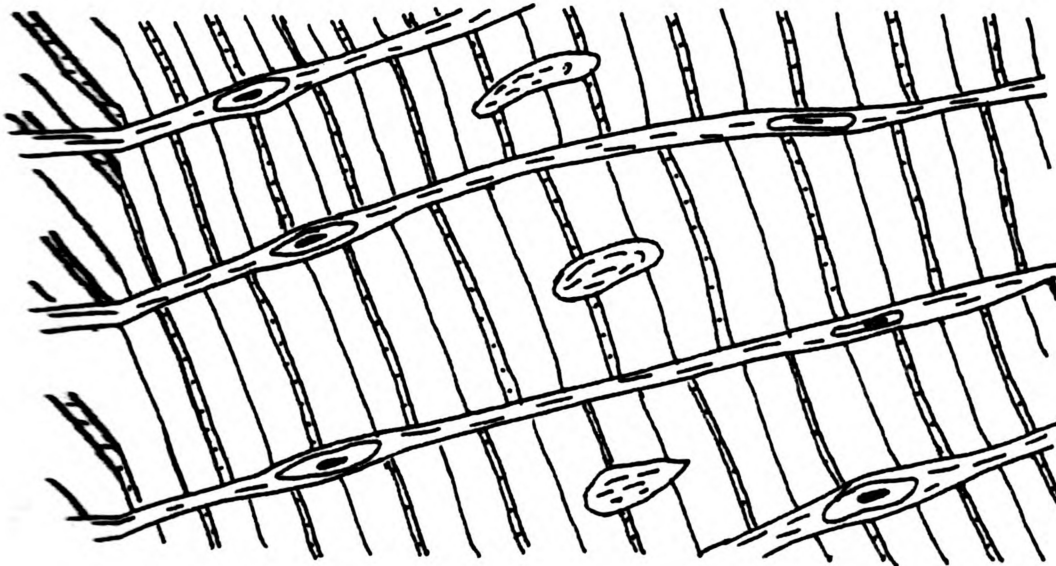


Figure 3.3 Muscle Tissue

bone/tissue or tissue/air interfaces, the characteristic impedance mismatch is so large that very little acoustic energy is transmitted (large reflection coefficient).

These tissue types form the layers of the various membranes of the body. The membranes cover the body, line various body cavities and enclose organs. In addition, muscle surfaces, organ surfaces, and interfaces between various organ parts, nerves, bones, tendons, etc., will all scatter ultrasonic energy. Signals returned to the receiving transducer from these interfaces are unwanted signals and only interfere with our ability to make accurate velocity measurements. These undesired returns are collectively known as clutter. Unlike noise, the effects of these returns cannot be reduced by increasing transmitter power. Only through appropriate signal design and/or sophisticated signal processing techniques can the effects of clutter be reduced.

Another important characteristic of tissue is its attenuation coefficient since it directly affects the design of an ultrasonic blood flow measuring instrument. With the exception of bone and lung tissue, other soft tissues exhibit attenuation coefficients ranging from .5 db per cm per MHz for adipose (fat) tissue, to over 2 db per cm per MHz for striated muscle tissue²⁸. Bone and lung tissue exhibit attenuation coefficients much greater than the attenuation coefficients listed above. For the remainder of this dissertation a nominal value of 2 db per cm per MHz will be

used for acoustic waves in the one to ten MHz category. Also, attenuation losses have been shown to vary directly with the carrier frequency²⁹ in biological tissue.

Of course, for a blood flow measurement system, the tissue whose characteristics are of most interest is the blood. Blood is composed of two major components. The first component is the fluid portion or blood plasma in which solutes are dissolved. The second component is the collection of living cells suspended in the plasma. These cells may be classified in one of three categories: erythrocytes, leukocytes, and thrombocytes.

Erythrocytes, or red blood cells, are approximately 7 microns in diameter, 1 - 2 microns thick, number 4.5 to 5.5 million, and occupy 40 to 50% of the total blood volume in a normal individual. The percentage of blood volume occupied by the red blood cells is known as the hematocrit.

The total volume occupied by the smaller and less numerous thrombocytes (platelets) and the leukocytes (white blood cells) is approximately 1% of the total blood volume. Thus, it is not surprising that the red blood cell has proven to be the major source of ultrasonic scattering from the blood³⁰.

Blood is only one component of a larger system called the cardiovascular system. The cardiovascular system includes the heart, arteries, capillaries, and veins. The

heart creates the pressure differential which pumps the blood through the system. The arteries carry blood away from the heart to the capillary beds in the tissue, and the veins return blood from the tissue to the heart.

The arteries and veins form a branching system of vessels which divide into more and more vessels of decreasing diameter as the capillary bed is approached. This branching occurs in such a way that the sum of the cross-sectional area of the two vessels following a branch is approximately 1.5 times the cross-sectional area of the vessel before the branch. Thus, the blood velocity decreases from an average value of 20 cm/sec in the aorta to less than .2 cm/sec in the capillary beds³¹. This research does not address flow measurement problems associated with microcirculation of the tissue. But rather, it is directed toward flow measurement in the major arteries having diameters greater than approximately .5 cm.

The major arteries and veins of the body resemble thin walled distensible circular cylindrical tubes. Their walls are made up of layers of endothelial cells, elastin fibers, smooth muscle, and collagenous fibers. Under control of the central nervous system, these vessels expand and contract to control blood flow and pressure. Also, blood flow in the arteries is quite pulsatile due to pulsatile pumping of the heart and these arteries expand and contract with the time

varying pressures in them. The situation is quite different in veins where flow is nearly time independent.

As derived in Appendix I, the flow profile for laminar flow in a circular cylindrical tube is parabolic.

$$V(r) = V_{\max} \left(1 - \frac{r^2}{a^2} \right) \quad 3.1$$

where a is the radius of the vessel.

The relationship between the average velocity across the cross section of the vessel and the maximum velocity in a parabolic profile is also derived in Appendix I and is found to be

$$V_{\max} = 2 \cdot V_{\text{avg}} \quad 3.2$$

At high velocities, the pattern of laminar flow breaks down and the fluid elements appear to flow in a random time varying fashion. The critical point at which this transition from laminar to turbulent flow occurs is defined by the so-called Reynolds number, where

$$\text{Reynolds number} = \frac{V_{\text{avg}} 2a\rho}{\eta} \quad 3.3$$

where ρ = blood density $\approx 1 \text{ gm/cm}^3$ and η is the blood viscosity which is approximately $.035 \text{ dyne sec/cm}^2$,³². Turbulence

usually occurs when the Reynolds number exceeds 2,300. Coulter and Papenheimer³³ found the critical Reynolds number for blood to be approximately 2,000. This indicates that, in the larger vessels, blood behaves much as a homogeneous fluid. With the exception of diseased vessels and flow at the root of the aorta, Reynolds numbers are usually well below 2,000 in the circulatory system. Thus, for purposes of this research, laminar flow will be assumed.

The design of any practical flow measuring instrument will be highly dependent upon the dynamic range of velocities to be measured. Figure 3.4 shows a typical plot of average volume flow rate vs. time for blood flow in the aorta. Using equation 3.2 and an average value of 1.0 cm for the diameter of the aorta, it is seen that blood velocities in the cardiovascular system should normally lie in the range of 0 - 100 cm/sec.

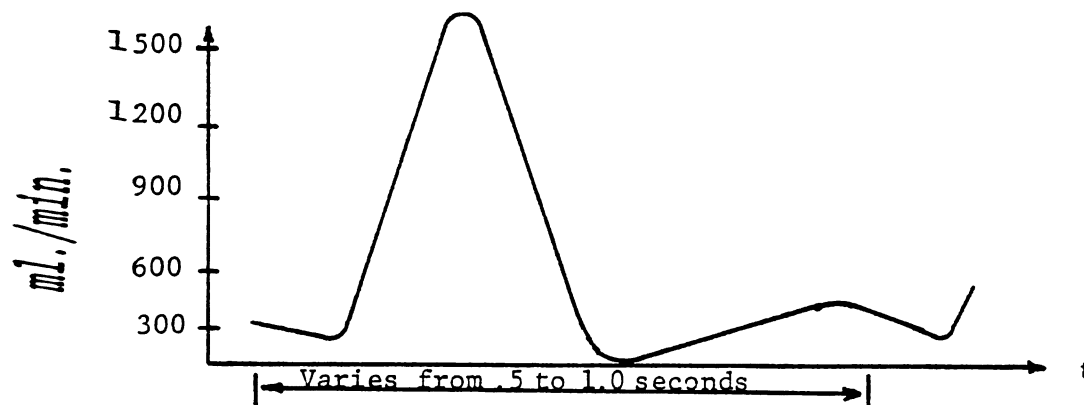


Figure 3.4 Typical Flow vs. Time in the Aorta

Another very important parameter characterizing the blood, as well as the surrounding tissue, is the effective scattering cross section. The scattering cross section of continuous biological media is defined as the fraction of incident acoustic power scattered in the direction of the receive transducer per unit solid angle per unit volume of media. A great deal of recent research has been directed toward measuring the scattering cross section of various tissues. Unfortunately, with only a few exceptions (whole blood for example), current measurements of absolute scattering cross sections provide little in the way of useful design data. However Baker, using the Duplex Scanner,²⁷ measured the relative scattering cross section of blood at 3Mhz to be 20 db below the scattering cross section of the vessel wall. In the analysis and design that follow, this number is used as the nominal relative scattering cross section of blood relative to all the surrounding tissue.

Also, experiments³⁴ have shown that the scattering cross section of blood increases as the fourth power of frequency and is nearly isotropic. This is consistent with Rayleigh scattering theory which states that given a Poisson distribution of independent scatterers, each with dimensions much less than a wavelength, and assuming first order scattering, then the scattered energy will be isotropic and exhibit a fourth power dependence on frequency. Thus, treating red blood cells as independent Poisson distributed scatterers is not only intuitively pleasing, but also consistent with the above

mentioned experimental results. The optimum choice of carrier frequency depends on a trade-off between the back scattered energy which is proportional to ω^4 and attenuation losses which are proportional to ω . Experience in building and working with C. W. Doppler flowmeters, Pulsed Doppler flowmeters, and Continuous Noise flowmeters has shown that 5 MHz is a reasonable choice for a blood flow imaging system.

Target Definition and Characterization

In Appendix F, a technique for using a correlation type receiver to estimate the range and range rate (or radial velocity) of a point target is introduced. It is shown that the maximum likelihood estimate of delay ($\hat{\tau}$) and Doppler frequency ($\hat{\omega}$) in the presence of white Gaussian noise is obtained by maximizing the square of the magnitude of the log likelihood function over all possible values of delay and Doppler frequency. That is:

$$\hat{\tau}, \hat{\omega} = \max_{\tau, \omega} |L(\tau, \omega)|^2 \quad \begin{matrix} \tau = \hat{\tau} \\ \omega = \hat{\omega} \end{matrix} \quad 3.4$$

where

$$L(\tau, \omega) = \int_{-\infty}^{\infty} \tilde{r}(t) \tilde{f}^* [(1 + \alpha)t - \tau] e^{j\omega t} dt \quad 3.5$$

In equation 3.4 $\tilde{r}(t)$ is the complex envelope of the received signal and $\tilde{f} [(1 + \alpha)t - \tau]$ is a delayed, time scaled version of the transmitted envelope.

There are two apparent difficulties with maximizing $|L(\tau, \omega)|^2$ as shown. One arises from the infinite limits of integration. The other because of the continuous nature of the candidate delay Doppler estimates. The first difficulty is easily removed since in any practical system the transmitted signal will be non-zero only for some finite time duration and therefore the limits of integration are finite. On the other hand, there is no apparent means of arguing away the existence of infinite possibilities for delay and Doppler estimates.

A practical method for dealing with this difficulty consists of the following two steps. First, limit the allowable ranges of both delay and Doppler to values which can physically occur. And secondly, divide the remaining ranges of τ and ω into a grid of discrete candidate delay/Doppler pairs. The pair which maximizes the magnitude of the log likelihood function is then chosen as the estimate of target delay and Doppler.

However, this introduces a new difficulty. Namely that of choosing the delay and Doppler separation of these pairs. A logical first step in solving this problem would be to somehow determine the delay and Doppler resolving capability of the transmitted signal. Fortunately, this information is available by properly interpreting the signal ambiguity function discussed in Appendix G. In the Appendix it is shown

that for all cases of interest in blood flow measurement, the range resolving capability is approximately the inverse of the effective bandwidth of the transmitted signal. Also, it is shown that the Doppler resolving capability of a conventional correlation receiver is roughly the inverse of the effective time duration of the signal, and it is suggested that in most cases of interest the same criteria holds for the true correlation receiver. However, demonstrating the reasonableness of this suggestion is reserved for Chapter Four where specific signals and their attributes are discussed. Thus a reasonable choice for delay separation of the discrete delay/Doppler pairs is also the inverse of the effective bandwidth and a reasonable choice for Doppler separation is, for most signals, the inverse of the effective signal duration.

As stated earlier, the objective of the blood flow imaging system is to estimate the velocity of the blood at a particular location within the vessel. That velocity estimate must be made by examining the sum of signals reflected from all red blood cells as they pass through the desired location. Therefore, since laminar flow has been assumed, the target will be defined as a "small" cylindrical subsection of the vessel parallel to the flow vector as shown in Figure 3.5. The range to the center of the target is assumed known. However, the approximate size and shape of the target cross section has not been specified. In general, the target shall consist of all red blood cells which by themselves would produce a significant

output from a correlation receiver perfectly matched in velocity and set at a known delay τ . Based on the previous discussion concerning the range resolving capability of the transmitted signal, the target shall specifically consist of those red blood cells which pass through the ultrasonic beam

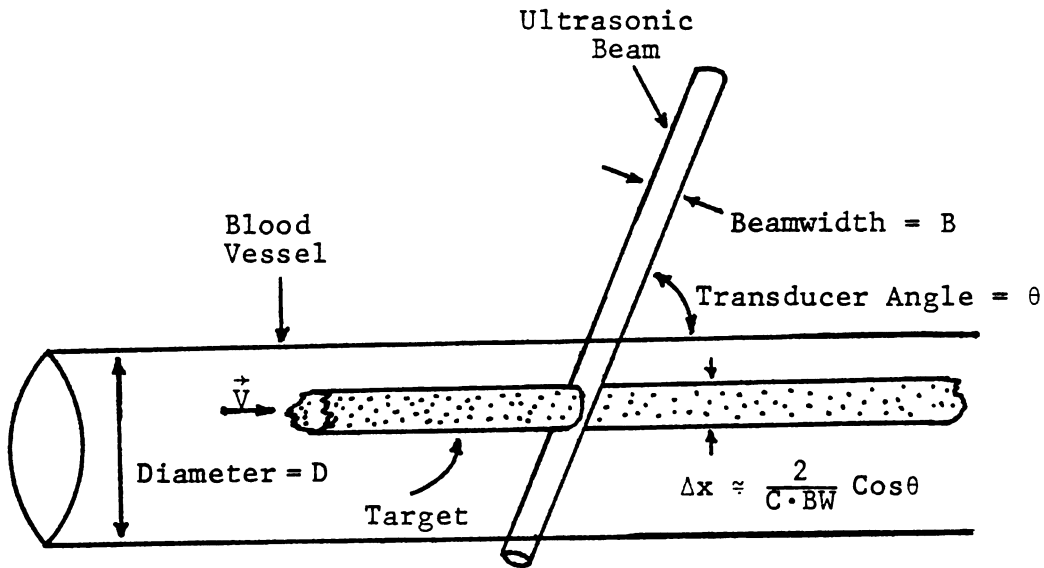


Figure 3.5 Target Definition

at ranges corresponding to delays between $\tau - \frac{1}{2 \cdot BW}$ and $\tau + \frac{1}{2 \cdot BW}$. The approximate dimensions and shape of a typical target are shown in the figure. Of course, the actual shape of the target depends on the specific signal and transducer beam pattern. Even when these are completely specified, the target shape is still somewhat arbitrary. Therefore, when specific target shapes and beam patterns are required, they will be chosen for mathematical convenience.

Having described and defined the physical target, a mathematical characterization (or model) shall be developed next. Figure 3.6 shows the geometric relationships between the target, the i^{th} RBC within the target, the ultrasonic beam, and the transducer. In addition to moving along the flow vector with velocity \bar{v}_i , the spatial orientation of the i^{th} RBC is continually changing. Thus, each red blood cell in the target appears as a fluctuating point target. However, the assumption will be made that each RBC appears as a non-fluctuating point target during the time required to pass through the ultrasonic beam. Additionally, it will be assumed that the beam is sufficiently narrow and the transducer sufficiently far removed such that θ_i is approximately equal to θ when the associated RBC is within the illumination volume. For

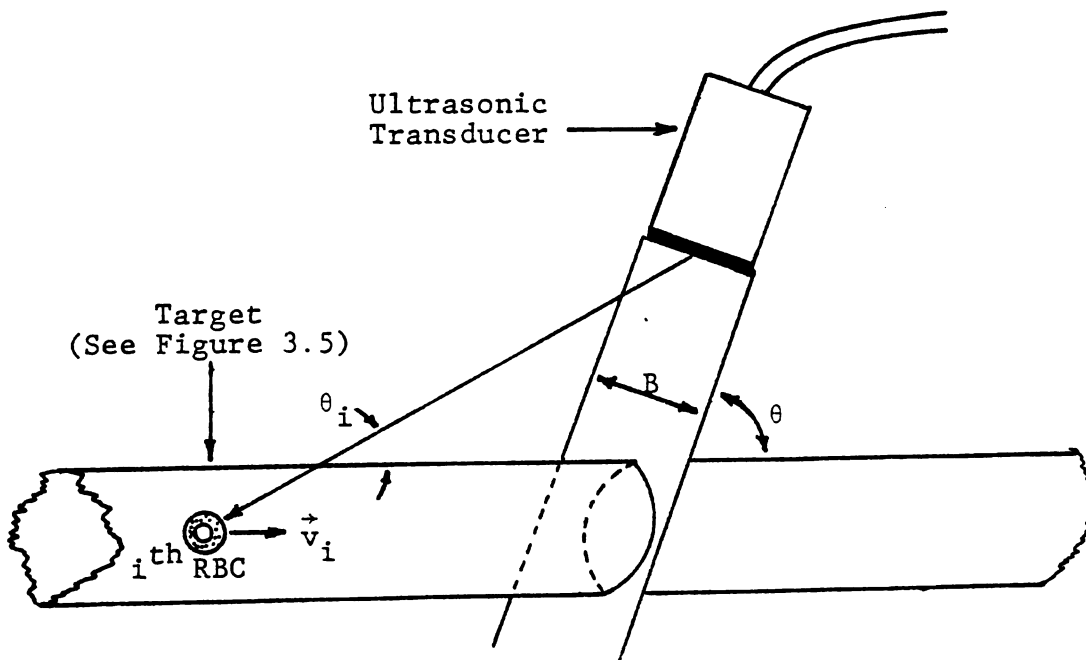


Figure 3.6 System Geometry

example, with a beam width of 1 mm and a target distance of approximately 2.5 cm, θ_i would vary on the order of two degrees. The importance of this assumption is to allow all RBC's along a particular streamline to be associated with a unique Doppler frequency given by:

$$\omega_d = \frac{2|\bar{v}_i|\omega_c}{c} \cos(\theta) \quad 3.6$$

Under these assumptions and temporarily neglecting the beam pattern, the signal received from the i^{th} red blood cell is the same as that derived for a point target in Appendix F (see equation F.14).

$$\tilde{r}_i(t) = \sqrt{E_t} \tilde{b}_i \tilde{f}[(1+\alpha(\bar{r}_i))t - \tau(\bar{r}_i)] e^{j\omega(\bar{r}_i) \cdot t} \quad 3.7$$

The effects of transducer losses, beam pattern, and two way propagation losses can be included by multiplying by an appropriate function of space $\tilde{T}(\bar{r}_i) = T(\bar{r}_i)e^{j\phi_i}$. If phase changes associated with $\tilde{T}(\bar{r}_i)$ are included in \tilde{b}_i , the actual received signal from the i^{th} red blood cell may be written as:

$$\tilde{r}_i(t) = \sqrt{E_t} \cdot T(\bar{r}_i + \bar{v}_i t) \tilde{b}_i \tilde{f}[(1+\alpha(\bar{r}_i))t - \tau(\bar{r}_i)] e^{j\omega(\bar{r}_i)t} \quad 3.8$$

The total signal received from all RBC's in the target is the sum of signals received from the individual red blood cells.

$$\tilde{r}(t) = \sum_i \tilde{r}_i(t)$$

Next, the summation will be divided into two summations. This division is achieved by breaking the target volume into small elements of equal volume V_j . Each V_j will in turn contain some random number, N_j , of red blood cells. The received signal may now be rewritten as:

$$\tilde{r}(t) = \sum_j \sum_{i=1}^{N_j} \sqrt{E_T} T(\bar{r}_{ij} + \bar{V}_{ij}t) \tilde{b}_{ij} \cdot \tilde{f}[(1 + \alpha(\bar{r}_{ij}))t - \tau(\bar{r}_{ij})] e^{j\omega(\bar{r}_{ij})t} \quad 3.9$$

If the volume elements are sufficiently small, then $\bar{r}_{ij} \approx \bar{r}_j$ and the expression for $\tilde{r}(t)$ can be rearranged as follows:

$$\tilde{r}(t) = \sum_j \sqrt{E_T} T(\bar{r}_j + \bar{V}_j t) \tilde{f}[(1 + \alpha(\bar{r}_j))t - \tau(\bar{r}_j)] \cdot e^{j\omega(\bar{r}_j)t} \cdot \sum_{i=1}^{N_j} \tilde{b}_{i,j} \quad 3.10$$

Because the reflection coefficients, \tilde{b}_{ij} , are assumed to be zero mean independent random variables, then for large N_j the central limit theorem allows the second summation in the above expression to be considered a single complex Gaussian random variable. Since $\tilde{r}(t)$ is a linear combination of complex Gaussian processes, it is itself a complex Gaussian process (see Appendix C). Additionally, the additive noise is considered Gaussian so that all the information required to evaluate the performance of the blood flow

imaging system or derive the optimum processing is contained in the covariance function of the received signal (see Appendix D). First the mean of $\tilde{r}(t)$ will be evaluated ($E\{\cdot\}$ is the expectation operator).

$$\begin{aligned}
 \tilde{m}(t) &= E\{\tilde{r}(t)\} \\
 &= E\left\{\sum_j \sqrt{E_t} T(\cdot) \tilde{f}(\cdot) e^{j\omega(\cdot)t} \sum_{i=1}^{N_j} \tilde{b}_{i,j}\right\} \\
 &= \sum_j \sqrt{E_t} T(\cdot) \tilde{f}(\cdot) e^{j\omega(\cdot)t} E\left\{\sum_{i=1}^{N_j} \tilde{b}_{i,j}\right\} \quad 3.11
 \end{aligned}$$

By assumption $E\{\tilde{b}_{ij}\} = 0$ so that

$$E\left\{\sum_{i=1}^{N_j} \tilde{b}_{i,j}\right\} = \sum_{i=1}^{N_j} E\{\tilde{b}_{i,j}\} = 0$$

Therefore,

$$\tilde{m}(t) = 0 \quad 3.12$$

This simplifies the expression for the complex covariance function $\tilde{K}(t_1, t_2)$.

$$\begin{aligned}
 \tilde{K}(t_1, t_2) &= E\{[\tilde{r}(t_1) - \tilde{m}(t_1)][\tilde{r}(t_2) - \tilde{m}(t_2)]^*\} \\
 &= E\{\tilde{r}(t_1)\tilde{r}^*(t_2)\} \quad 3.13
 \end{aligned}$$

Substituting for $\tilde{r}(t)$ from equation 3.10, the covariance function becomes

$$\tilde{K}(t_1, t_2) = E \left\{ \left[\sum_j \sqrt{E_t} \tilde{g}_j(t_1) \sum_{i=1}^{N_j} b_{i,j} \right] \left[\sum_k \sqrt{E_t} g_k^*(t_2) \sum_{\ell=1}^{N_k} \tilde{b}_{\ell,k}^* \right] \right\} \quad 3.14$$

where

$$\tilde{g}_j(t) = T(\bar{r}_j + \bar{V}_j t) \tilde{f}[(1 + \alpha(\bar{r}_j))t - \tau(\bar{r}_j)] e^{j\omega(\bar{r}_j)t} \quad 3.15$$

or

$$\tilde{K}(t_1, t_2) = E_t \sum_j \sum_k \tilde{g}_j(t_1) g_k^*(t_2) E \left\{ \sum_{i=1}^{N_j} \sum_{\ell=1}^{N_k} \tilde{b}_{i,j} \tilde{b}_{\ell,k}^* \right\} \quad 3.16$$

Because of the independence assumption for scattering from individual red blood cells, i.e.,

$$E\{\tilde{b}_m \tilde{b}_n^*\} = \begin{cases} 2\sigma_b^2 & m=n \\ 0 & m \neq n \end{cases}$$

the only terms which contribute to $\tilde{K}(t_1, t_2)$ are those which contain products of the form $\tilde{b}_{ij} \tilde{b}_{ij}^* = |\tilde{b}_{ij}|^2$. Thus $\tilde{K}(t_1, t_2)$ may be simplified as:

$$\tilde{K}(t_1, t_2) = E_t \sum_j \tilde{g}_j(t_1) \tilde{g}_j^*(t_2) E \left\{ \sum_{i=1}^{N_j} |\tilde{b}_{i,j}|^2 \right\} \quad 3.17$$

Now since N_j and \tilde{b}_{ij} are both independent random variables the expectation in equation 3.17 is by the definition of expectation (letting $x_{ij} = |\tilde{b}_{ij}|^2$):

$$\begin{aligned} E \left\{ \sum_{i=1}^{N_j} x_{i,j} \right\} &= \sum_{N_j=1}^{\infty} \int_0^{\infty} \sum_{i=1}^{N_j} x_{i,j} p(N_j, x) dx \\ &= \sum_{N_j=1}^{\infty} \int_0^{\infty} \sum_{i=1}^{N_j} x_{i,j} p(x) P(N_j) dx \\ &= \sum_{N_j=1}^{\infty} \sum_{i=1}^{N_j} \int_0^{\infty} x_{i,j} p(x) dx P(N_j) \\ &= \sum_{N_j=1}^{\infty} N_j 2\sigma_b^2 P(N_j) \\ &= 2\sigma_b^2 E\{N_j\} \end{aligned} \quad 3.18$$

Since the red blood cells are by assumption Poisson distributed in space, the average number within any volume element ΔV_j with volume ΔV is given as

$$E\{N_j\} = \rho \Delta V \quad 3.19$$

where ρ is the density of red blood cells.

Substituting these results into the expression for the covariance of $\tilde{r}(t)$ provides further simplification.

$$\tilde{K}(t_1, t_2) = 2\sigma_b^2 E_t \rho \sum_j \tilde{g}_j(t_1) \tilde{g}_j^*(t_2) \Delta V \quad 3.20$$

In order to replace the summation with an integral it is necessary that ΔV be much smaller than λ^3 and still contain a statistically significant number of RBC's. At 5 MHz, λ^3 is approximately $2.7 \times 10^{-6} \text{ cm}^3$. This volume contains over 20,000 red blood cells. Even at $\Delta V = \lambda^3/1000$ there are still an average of 20 RBC's per ΔV , more than adequate for the Gaussian approximation to be valid.³⁵ Thus the final form of $\tilde{K}(t_1, t_2)$ is

$$\tilde{K}(t_1, t_2) = 2\sigma_b^2 E_t \rho \int_{\text{target volume}} \tilde{g}(t_1) \tilde{g}^*(t_2) dV \quad 3.21$$

$$\tilde{g}(t) = T(\bar{r} + \bar{V}(\bar{r})t) \tilde{f}[(1 + \alpha(\bar{r}))t - \tau(\bar{r})] e^{j\omega(\bar{r})t}$$

This is the desired characterization and is a major result in the analysis of a blood flow imaging system. This result will be used extensively in Chapter Five.

Next a very crude but useful characterization of tissue surrounding the target is developed.

Simple Tissue Model

When performing transcutaneous blood flow measurements using ultrasound, there are many sources of scattering other than the target red blood cells. These sources include various tissue interfaces as well as red blood cells elsewhere within the vessel. Returns from such undesired clutter will degrade the performance of certain ultrasonic flowmeters and the system designer should be cognizant of their effect. Using the measurement technique chosen for this research, there are two potential methods of combating clutter, signal processing and appropriate signal design.

In order for signal processing to be effective the designer must have adequate knowledge of the clutter environment. This knowledge may take one of two forms: (1) a deterministic description of the scattering characteristics of all internal structures, or (2) a good statistical model for tissue scattering. Deterministic knowledge of all internal tissue interfaces is clearly impractical if not impossible to obtain and use. Also, at this time an adequate statistical description of tissue scattering is not available. In fact, since such a statistical model must be valid for all possible transducer positions and orientations, it too may be impractical or impossible to develop.

Fortunately, using only a very rudimentary model for the target environment, system performance may be quite effec-

tively optimized through appropriate signal selection. Unfortunately, very little information is available which aids in formulating even a crude characterization. However, in this section a model is described which makes use of the available information and provides a realistic worst case clutter characterization.

The model used for the target environment will be called the relative range scattering function. The purpose of this range scattering function is to describe the distribution of returned energy as a function of the range at which it was reflected. In developing this model it will be assumed that the gross attenuation and scattering properties of tissue is homogeneous. If second order scattering effects are ignored, then the intensity of ultrasound incident on a differential range element of tissue at range R is:

$$I_{\text{incident}} = I_t e^{-2aR}$$

where a is the attenuation coefficient of tissue. The intensity of the wave reflected in the direction of the transducer is found by multiplying the incident intensity by the square of the reflection coefficient and the size of the differential range element (see equation H17).

$$I_{\text{reflected}} = |\Gamma_T|^2 \cdot dR \cdot I_{\text{incident}} \quad 3.23$$

Here Γ_T has been used to represent the reflection coefficient of tissue. The reflected energy is attenuated as it propagates back to the receive transducer so that the received intensity of the wave is:

$$I_{\text{received}} = e^{-2aR} \cdot I_{\text{reflected}} \quad 3.24$$

$$I_{\text{received}} = |\Gamma_T|^2 I_t e^{-4aR} dR \quad 3.25$$

It will be assumed that the center of the vessel of interest is located at a range given by R_c and has a radius of R_r . If blood is considered to be lossless, the intensity of ultrasound at the receive transducer due to reflection from within the blood vessel is given by:

$$I_{\text{received}} = |\Gamma_B|^2 I_t e^{-4a(R_c - R_r)} dR \quad 3.26$$

If a uniform beam of cross sectional area A is assumed, then, by comparison with $\tilde{K}(t, t)$ from equation 3.21, it is seen that the reflection coefficient of blood may be written as:

$$|\Gamma_B|^2 = 2\sigma_B^2 \rho A \quad 3.27$$

Notice that in equation 3.21 the attenuation factor e^{-4aR} has been absorbed in the beam profile $T(\bar{r}, \bar{v}, t)$. Because of the one-to-one correspondence between range and delay, the range scattering function is easily made a function of τ rather than R . Making the change of variables

$$R = \frac{\tau \cdot c}{2} \quad 3.28$$

The general range scattering function may be written as:

$$S(\tau) = |\Gamma_T|^2 I_t e^{-2ac\tau} d\tau \cdot \frac{c}{2} \quad 0 < \tau < \tau_c - \tau_r$$

$$S(\tau) = |\Gamma_B|^2 I_t e^{-2ac(\tau_c - \tau_r)} d\tau \cdot \frac{c}{2} \quad \tau_c - \tau_r < \tau < \tau_c + \tau_r$$

$$S(\tau) = |\Gamma_T|^2 I_t e^{-2ac(\tau - 2\tau_r)} d\tau \cdot \frac{c}{2} \quad \tau > \tau_c + \tau_r$$

Since only relative scattering intensities will be of interest in the following chapters, the range scattering function may be normalized to $|\Gamma_T|^2 I_t \cdot \frac{c}{2} d\tau$. The result of this normalization is the desired relative range scattering function.

$$S_R(\tau) = e^{-2ac\tau} \quad 0 < \tau < \tau_c - \tau_r \quad 3.29$$

$$S_R(\tau) = \frac{|\Gamma_B|^2}{|\Gamma_T|^2} e^{-2ac(\tau_c - \tau_r)} \quad \tau_c - \tau_r < \tau < \tau_c + \tau_r \quad 3.30$$

$$S_R(\tau) = e^{-2ac(\tau - 2\tau_r)} \quad \tau > \tau_c + \tau_r \quad 3.31$$

Using the assumed value of 10 db/cm for the attenuation of ultrasound in tissue at 5 Mhz, the value of a is found as $a = 1.15$ (refer to Appendix H for the conversion factor). As mentioned earlier, the relative reflection

coefficient of tissue was measured by Baker and found to be 20 db above that for whole blood. Thus the ratio $|r_B|^2/|r_T|^2$ equals .01. Substituting these values into equations 3.29 through 3.31, the final form of the relative range scattering function may be written.

$$S_R(\tau) = e^{-\eta\tau} \quad 0 < \tau < \tau_c - \tau_r \quad 3.32$$

$$S_R(\tau) = .01e^{-\eta(\tau_c - \tau_r)} \quad \tau_c - \tau_r < \tau < \tau_c + \tau_r \quad 3.33$$

$$S_R(\tau) = e^{-\eta(\tau - 2\tau_r)} \quad \tau > \tau_c + \tau_r \quad 3.34$$

where $\eta = 3.45 \times 10^5$.

In the next chapter various signals will be evaluated in terms of their clutter rejection capabilities. To do this a typical vessel range of 2.25 cm will be assumed and the vessel will be assumed to have a diameter of .5 cm. In this case, equations 3.32 through 3.34 may be further simplified.

$$S_R(\tau) = e^{-\eta\tau} \quad 0 < \tau < 3 \times 10^{-5} \quad 3.35$$

$$S_R(\tau) = 3 \times 10^{-7} \quad 3 \times 10^{-5} < \tau < 3.67 \times 10^{-5} \quad 3.36$$

$$S_R(\tau) = e^{-\eta(\tau - 6.67 \times 10^{-6})} \quad \tau > 3.67 \times 10^{-5} \quad 3.37$$

Figure 3.7 shows a sketch of $10 \cdot \log[S_R(\tau)]$ described by equations 3.35, 3.36, and 3.37.

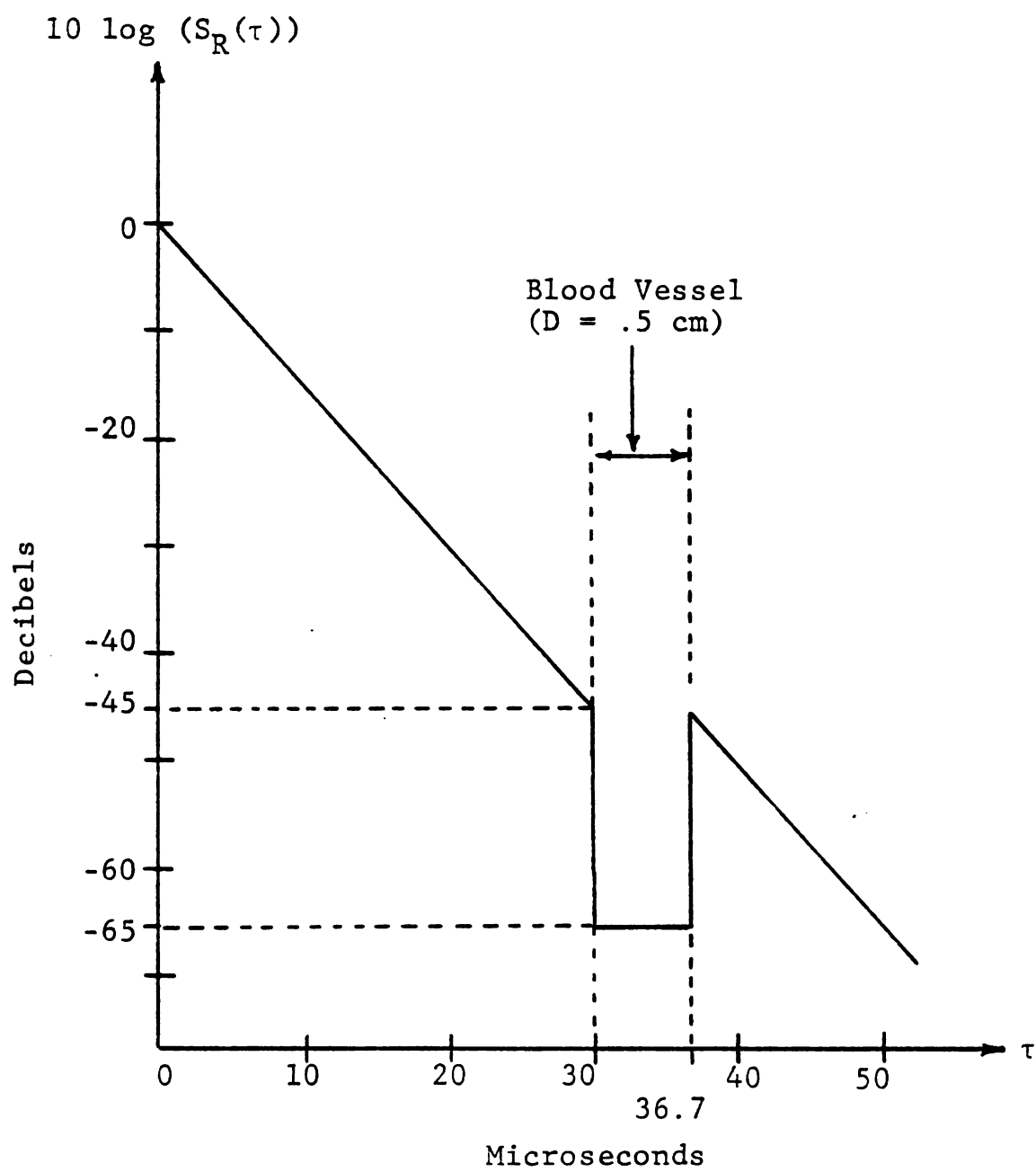


Figure 3.7 Typical Relative Range Scattering Function

Another dimension may be added to the Relative Range Scattering function which describes the distribution of energy at each range as a function of the Doppler shift which occurs upon reflection. The resulting function will be called the Relative Range Doppler Scattering function, $S_{RD}(\tau, f)$. For purposes of the analysis conducted in this dissertation it is adequate to assume that tissue is stationary. Also, if laminar flow is assumed, the Doppler within the vessel may be described as a function of range, $f_D(R)$. Note: In circular cylindrical vessels $f_D(R)$ will be parabolic. This information is easily incorporated into the clutter model in the following manner.

$$S_{RD}(\tau, f) = S_R(\tau) \delta(f) \quad 3.38$$

$$S_{RD}(\tau, f) = S_R(\tau) \delta(f - f_D(\tau)) \quad 3.39$$

$$S_{RD}(\tau, f) = S_R(\tau) \delta(f) \quad 3.40$$

To compute the total relative energy output of a correlation receiver perfectly matched to the target Doppler due to reflections from scatterers located in a specific region of delay space, the relative range Doppler scattering function is combined with the ambiguity function as follows.

$$E_c = \int_{\tau} \int_{-\infty}^{\infty} S_{RD}(\tau, f) \theta(\tau - \tau_t, f - f_t) df d\tau \quad 3.41$$

where τ_t and f_t are the target delay and Doppler, respectively.

This relationship will be used extensively in the next chapter to evaluate the clutter rejection capability of various signals.

CHAPTER IV

SIGNAL CONSIDERATIONS

In this chapter a particular waveform is selected as the transmitted signal. The first step in the selection process will consist of describing and discussing desirable signal characteristics in the context of blood flow imaging. Next, various signals are discussed and evaluated based on these desirable characteristics. And finally, any practical technological limitations will be considered in the selection of a modulation waveform.

Desirable Signal Characteristics

This section contains a listing of waveform characteristics which are considered desirable for blood flow imaging.

1. Large Bandwidth. As previously discussed, the range resolving capability of a flow imaging system is inversely proportional to the bandwidth of the transmitted signal. However, there are practical and theoretical reasons for limiting bandwidth which will be discussed later. At this point, it is sufficient to indicate that bandwidths in the range of one to three megahertz are reasonable.

2. Long Time Duration. For a conventional correlation receiver the Doppler (velocity) resolving capability is inversely proportional to the effective signal duration and therefore a long time duration signal is desirable. As with bandwidth, limitations will be placed on the maximum reasonable signal duration. Typical values will lie in the range from one to ten milliseconds.
3. High Energy Signal. Higher energy signals mean higher signal-to-noise ratios which is clearly a desirable characteristic.
4. Low Peak Power. Although adequate information is not available to make a definitive statement about the in-vivo effects of ultrasound, some concern has been expressed about the potential damage caused by high peak power.^{25,26} However, peak power input to LZT type transducers on the order of 10-30 watts has been used routinely and safely.²⁷
5. High Immunity to Clutter. A signal which minimizes the contribution of clutter returns to the correlator output will improve overall system performance.

Signal Selection

The primary tool which will be used in evaluating the acceptability of a given signal will be the conventional

ambiguity function. Additionally, the process of selecting a specific signal must take into account practical technological limitations as well as the desirable signal characteristics. After a specific signal is chosen it is shown that the Doppler resolution of the true correlation receiver is well approximated as that indicated by the ambiguity function.

One of the simplest modulation waveforms one might consider is the single pulse. The ambiguity function for the single pulse is easily derived as follows:

$$\begin{aligned}
 \tilde{f}(t) &= \frac{1}{\sqrt{T}} \quad \text{for} \quad -\frac{T}{2} < t < \frac{T}{2} \\
 &= \frac{1}{\sqrt{T}} \pi\left(\frac{t}{T}\right) \\
 \phi(\tau, f) &= \int_{-\infty}^{\infty} \frac{1}{T} \pi\left(\frac{t}{T}\right) \pi\left(\frac{t-\tau}{T}\right) e^{j2\pi f t} dt \\
 &= F \left\{ \frac{1}{T} \pi\left(\frac{t-\tau/2}{T-|\tau|}\right) \right\} \\
 &= \frac{T-|\tau|}{T} e^{-j\pi f \tau} \text{sinc}((T-|\tau|)f) \\
 \theta(\tau, f) &= |\phi(\tau, f)|^2 = \left(\frac{T-|\tau|}{T}\right)^2 \text{sinc}^2((T-|\tau|)f) \quad 4.1
 \end{aligned}$$

where

$$\pi(x) = \begin{cases} 1 & |x| < \frac{1}{2} \\ 0 & \text{elsewhere} \end{cases}$$

In Figure 4.1, illustrating the ambiguity function for a single pulse, it is observed that the function has a single peak whose width along the delay axis is directly proportional to the pulse width and whose width along the frequency axis is inversely proportional to the pulse width. To achieve the velocity resolutions necessary for blood flow imaging (i.e., 100 hz - 1 Khz with a 5 Mhz carrier) signal durations on the order of one to ten milliseconds must be used. Since this provides a range resolving capability in the 75 to 750 cm range, the single pulse is clearly unacceptable.

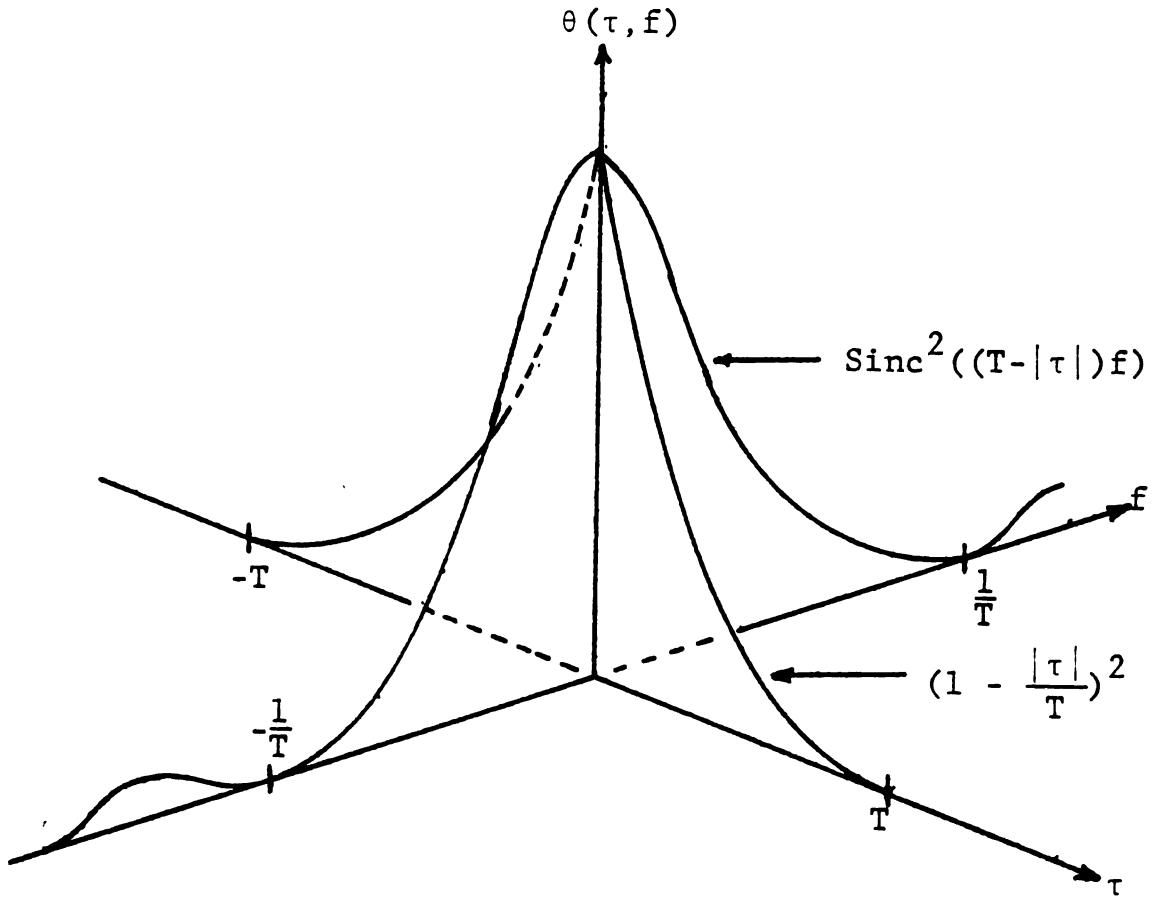


Figure 4.1 Ambiguity Function for a Single Pulse

One method of improving the range resolving capability without disturbing the velocity resolution is to introduce complexities into the transmitted pulse. For example, if the basic pulse is multiplied by wideband noise, a large bandwidth long time duration signal is generated. The average or expected ambiguity function for such a signal is derived by computing

$$\bar{\Theta}(\tau, f) = E\{\phi(\tau, f) \phi^*(\tau, f)\} \quad 4.2$$

where the expectation is an ensemble average taken over all possible waveforms of the noise process. The ambiguity function for random noise has been derived by Cooper³⁶ and is shown in Figure 4.2.

As expected, the width along the delay axis is determined by the signal bandwidth while the width along the frequency axis is determined by the signal duration. Of particular importance is the fact that there are no significant ambiguous responses.

There are difficulties in implementing a random signal system. One of the limiting devices in the hardware implementation of this system is the delay line required to produce a delayed version of the transmitted signal. This delay line must be capable of delaying a 1-3 Mhz bandwidth

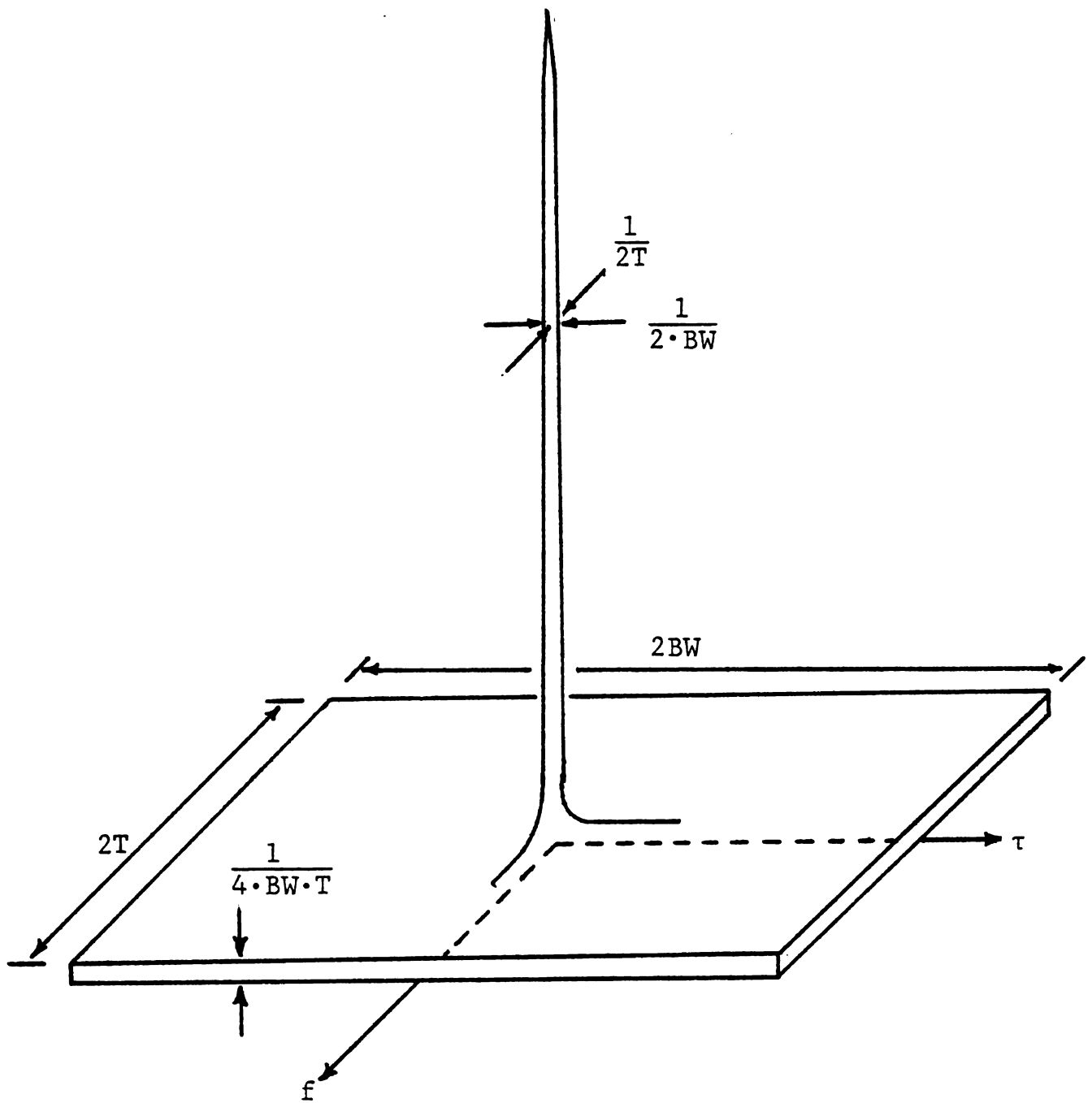


Figure 4.2 Ambiguity Function for Random Noise

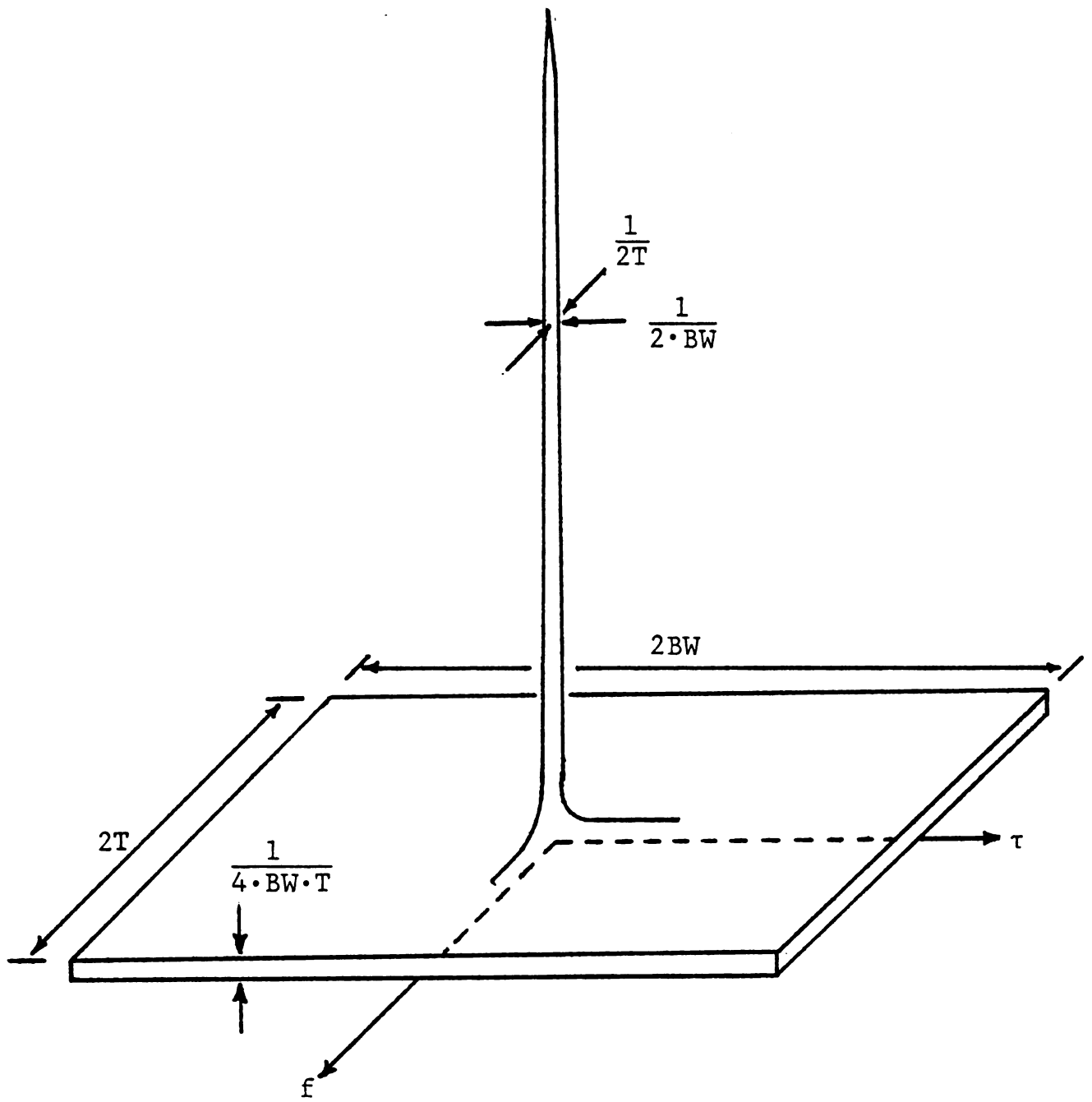


Figure 4.2 Ambiguity Function for Random Noise

analog signal centered at 5 Mhz for up to 50 μ s. The requirement for such a delay line is unique to systems using non-deterministic signals. In the past, analog acoustic delay lines were used in the experimental random signal system described in Chapter Two. However, these mechanically varied lines are much too slow for use in velocity imaging.

Pseudo random codes (Barker codes, Gold codes, and other Pseudo Noise (PN) sequences) have been developed to approximate a random pulse sequence. Actually, these codes are deterministic and therefore the use of a delay line to preserve the transmitted waveform is not required. There is a class of PN sequences which are particularly appealing. They are called maximal length linear shift register sequences. Briefly, these sequences are called shift register sequences because they can be generated by a feedback shift register. A typical feedback arrangement is shown in Figure 4.3.

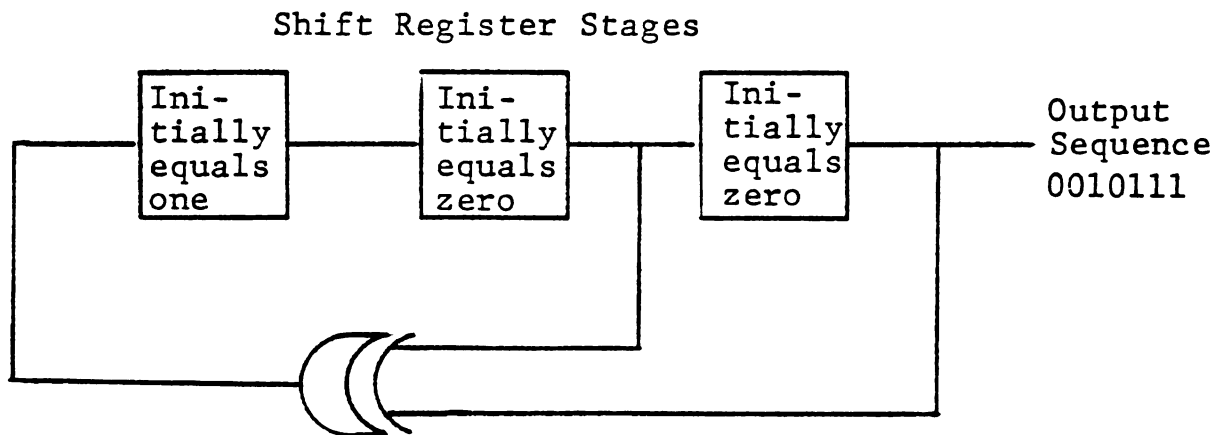


Figure 4.3 A Typical Feedback Shift Register

They are called maximal length because they are periodic on $2^L - 1$ clock pulses, where L is the number of shift register stages employed. For example, see the output sequence associated with the feedback shift register of Figure 4.3. Additionally, PN sequences exhibit some very nice properties which make them nearly ideal substitutes for truly random sequences. Specifically, the number of ones exceeds the number of zeros by one, a run of length K occurs with probability 2^{-K} and the cyclic autocorrelation function has constant sidelobes equal to $-1/N$. Unfortunately, the noncyclic autocorrelation function, $\phi(\tau, 0)$, for PN sequences does not have uniformly flat sidelobes. However, it has been shown³⁷ that the average sidelobe level for the ambiguity function (for PN sequences) along the delay axis, $\phi(\tau, 0)$, is $-1/N$. Also, the average ambiguity function for PN sequences has been shown to be approximately that pictured for random noise in Figure 4.2. The only modifications necessary are to replace bandwidth (BW) with $1/T_B$ (where T_B is the bit period) so that $T \cdot BW$ is N , the length of the code in bits. Figure 4.4 illustrates the average sidelobe level of an ambiguity function for a PN sequence.

Typically, these sequences are used to Binary phase modulate a carrier. With this modulation scheme, the transmitted signal exhibits most of the desirable signal characteristics mentioned earlier. Specifically, it can be a large

bandwidth long time duration signal with the highest possible energy for the lowest peak power.

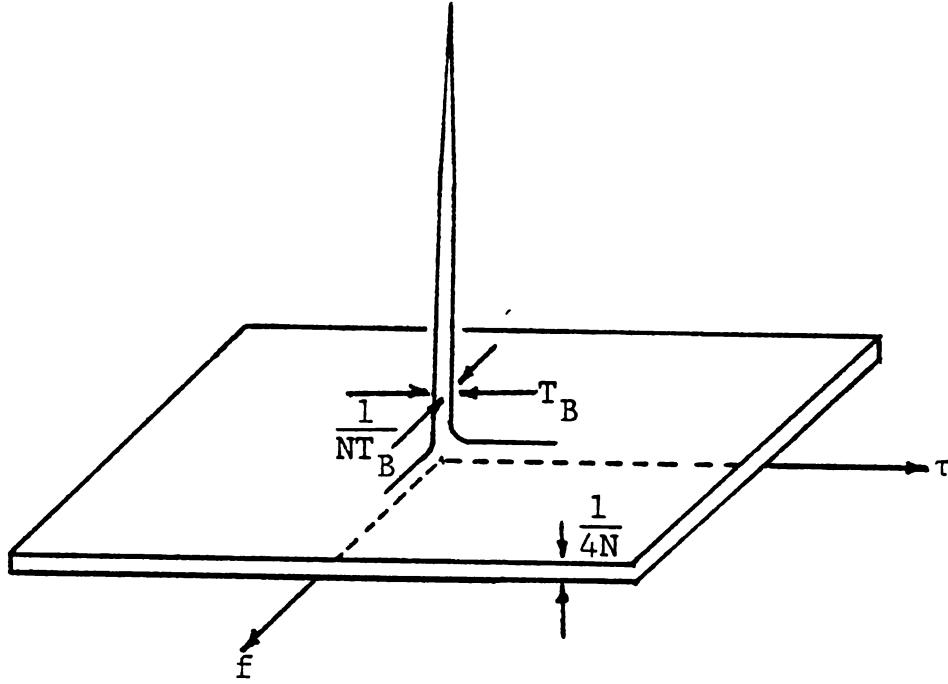


Figure 4.4 Average Ambiguity Function for a PN Sequence

To evaluate the potential performance of a correlation receiver using this signal in the presence of clutter, the clutter model of equations 3.38, 3.39, 3.40 will be combined with the ambiguity function of Figure 4.4 through the relationship given by equation 3.41. Using these models, the average output of the correlation receiver due to target returns in the absence of noise can be reduced to:

$$E_t = \int_{\text{target}} S_R(\tau) \theta(\tau - \tau_t, f_D(\tau) - f_t) d\tau \quad 4.3$$

For a target perfectly matched in Doppler to the correlator and having a range extent of $\Delta\tau$, the average energy returned from the target is: (using equation 3.36)

$$E_t = \Delta\tau \cdot 3 \times 10^{-7} \quad 4.4$$

In deriving this expression, a uniform velocity profile within the target has been assumed. The effects of Doppler spreading due to non-uniform profiles will be considered in Chapter Six.

Similarly, the average energy output due to clutter returns is found by substituting equations 3.38, 3.39, 3.40 into equation 3.41 and using equations 3.35, 3.36, and 3.37.

$$\begin{aligned} E_c &= \int_{\text{clutter}} S_R(\tau) \theta(\tau - \tau_t, f_D(\tau) - f_t) d\tau \\ &= \int_0^\infty e^{-\eta\tau} \frac{1}{4N} d\tau + \int_{3 \times 10^{-5}}^{3.7 \times 10^{-5}} 3 \times 10^{-7} \frac{1}{4N} d\tau \\ &\quad - \Delta\tau \cdot 3 \times 10^{-7} \frac{1}{4N} \\ &\approx \frac{7.2 \times 10^{-7}}{N} \quad 4.5 \end{aligned}$$

For a typical delay resolution on the order of 1×10^{-6} the signal-to-clutter ratio is computed as follows:

$$\text{SCR} \approx \frac{\Delta\tau \cdot 3 \times 10^{-7}}{\frac{7.2 \times 10^{-7}}{N}}$$

$$\text{SCR} = 4.2N \times 10^{-7}$$

4.6

This is an example of the signal-to-clutter ratio expected for a typical .5 cm diameter vessel located 2.25 cm from the transducer using a long time duration PN sequence. The correct interpretation of equation 4.6 is that increasing the number of bits in the sequence improves the signal-to-clutter ratio. In the case of blood flow imaging where 1-10 msec signals are required, N will range from 10^3 to 10^4 which results in an SCR in the range from .0004 to .004. This is not an acceptable value and other signals must be investigated.

The simplest large time bandwidth product signal which combats clutter as well as or better than any other signal is the periodic pulse train shown in Figure 4.5.

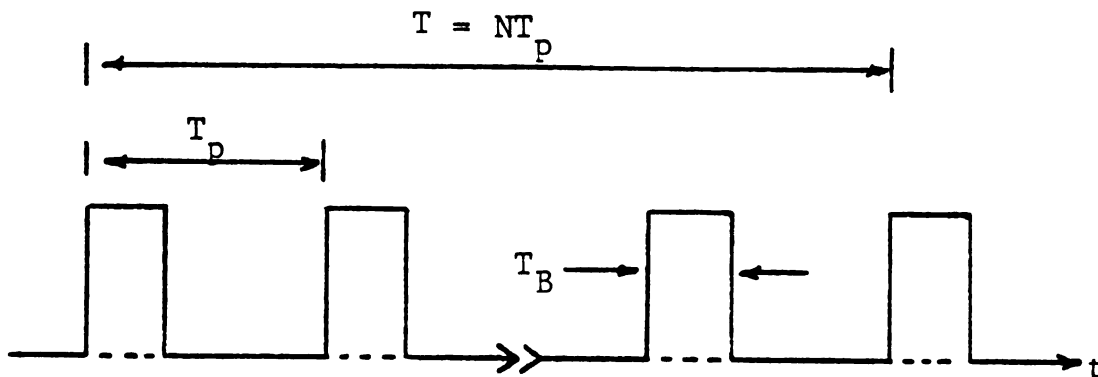


Figure 4.5 Periodic Pulse Train

Insight into some of the properties of ambiguity functions can be gained by intuitively developing an approximate representation for the ambiguity function associated with a periodic pulse train. (A rigorous derivation is available in any standard radar text.) From Figure G2, it is observed that the area of the pedestal of a generalized ambiguity function is $2T \cdot 2BW$. For the periodic pulse train this area is approximately $2NT_p \frac{2}{T_B}$. However, the ambiguity function is non-zero only in narrow strips parallel to the Doppler axis. The width of these strips is approximately T_B so that the total area where the function takes on non-zero values is approximately $2NT_p \frac{2}{T_B} \frac{T_B}{T_p}$. Since the volume of the ambiguity function must be unity, the average pedestal height is $\frac{1}{4N}$. Using this and properties one and two in Appendix G, an approximate ambiguity function has been sketched in Figure 4.6. This approximation for the average pedestal height between peaks has neglected the volume under each peak. If this volume had been included, the derived value for the pedestal height would have been reduced slightly.

The important features of this particular ambiguity function are 1) the narrow central peak, 2) the presence of "clear" areas that are not affected by clutter, and 3) the presence of subsidiary peaks. Clutter present at these peaks can cause the receiver to make an incorrect decision.

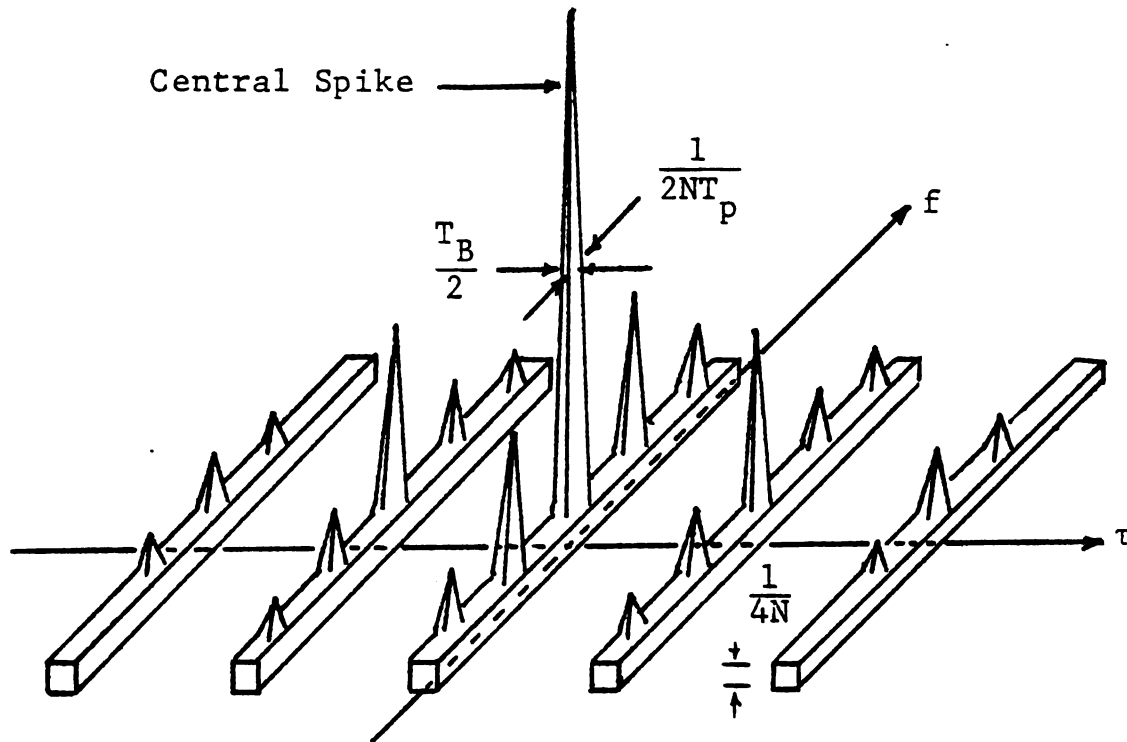


Figure 4.6 Approximate Ambiguity Function for a Periodic Pulse Train

Based on the clutter model of Chapter Three, it is reasonable to assume that clutter more than about 2.5 cm beyond the vessel is negligible. Therefore, to allow for the observation of vessels up to 3.5 cm deep the ambiguity peaks in delay must be greater than $47 \mu s$ (the two-way propagation time to a target 3.5 cm deep). This corresponds to a Pulse Repetition Frequency (PRF) of 21 KHz or less. To allow a margin of safety, a PRF of 10 KHz is selected. This choice of PRF generates ambiguous peaks in

Doppler separated by 10 KHz. Since the maximum expected Doppler is on the order of 5 KHz, this is completely acceptable.

This signal choice provides the best immunity to clutter, and at the same time provides the worst ratio of total energy to peak power.

However, it has been suggested that another class of signals exist which reach a reasonable compromise between the PN sequence and the pulsed sinusoid. These signals are formed by replacing each pulse of the periodic pulse train with a slightly longer time duration burst of a large bandwidth signal.

One possible compromise would be to replace each pulse with a short, large bandwidth PN sequence, and observe the effect on the signal-to-clutter ratio. A typical signal sequence is illustrated in Figure 4.7.

The sequence period is selected to be 10^{-4} seconds as it was for the periodic pulse train. The total signal duration is T , (1-10 msec), and T_B is the bit period, which is on the order of 1 μ s.

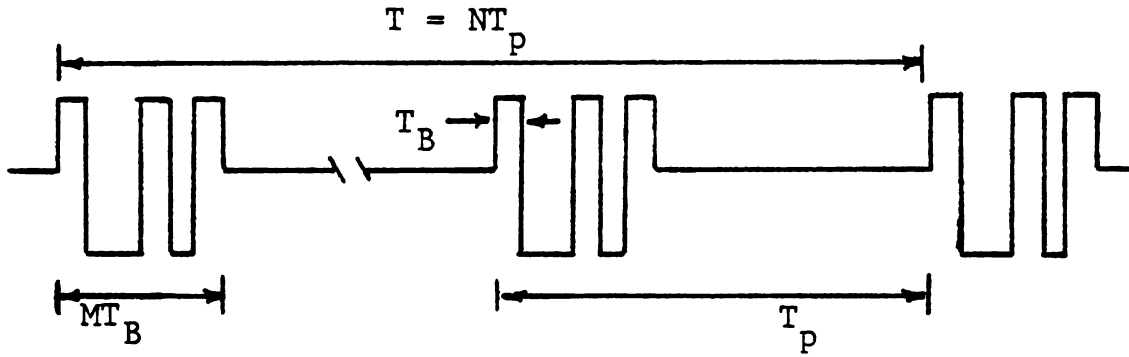


Figure 4.7 Periodic Train of PN Sequences

This signal may be represented analytically as

$$\tilde{f}(t) = \sqrt{\frac{T_p}{MT_B T}} \left\{ \begin{array}{l} \frac{T}{T_p} - 1 \\ \sum_{k=0}^{\quad} P(t - kT_p) \end{array} \right\} \quad 4.7$$

where $P(t)$ is an M bit PN sequence. The first step in computing the ambiguity function is to compute the time frequency autocorrelation function $\tilde{\phi}(\tau, f)$.

$$\tilde{\phi}(\tau, f) = \int_{-\infty}^{\infty} f(t) f^*(t + \tau) e^{j2\pi f t} dt \quad 4.8$$

If T_p is greater than $2MT_B$, then $\tilde{\phi}(\cdot)$ contains strips of clear area for certain values of τ . These strips of clear area lie midway between the subsidiary peaks of $\tilde{\phi}(\cdot)$ along the delay axis. The centers of the clear areas nearest the origin correspond to the location of clutter 3.75 cm from the target. Since the greatest expected target depth is 3.5 cm, the only portion of the ambiguity function which is

of any interest lies between these first two clear areas.

For $|\tau| < MT_B$ using 4.7 in 4.8,

$$\tilde{\phi}(\tau, f) = \frac{T_P}{MT_B T} \sum_{k=0}^{\frac{T}{T_P} - 1} \left[\int_{kT_P}^{kT_P + MT_B - |\tau|} P(t - kT_P) P^*(t - kT_P + \tau) e^{j2\pi f t} dt \right]$$

4.9

Letting $u = t - kT_P$

$$\tilde{\phi}(\tau, f) = \frac{T_P}{T} \sum_{k=0}^{\frac{T}{T_P} - 1} \left[\frac{1}{MT_B} \int_0^{MT_B - |\tau|} P(u) \cdot P^*(u + \tau) e^{j2\pi f u} du \right] e^{j2\pi f k T_P}$$

$$\tilde{\phi}(\tau, f) = \frac{T_P}{T} \sum_{k=0}^{\frac{T}{T_P} - 1} e^{j2\pi f k T_P} \tilde{\phi}_P(\tau, f)$$

4.10

The summation in equation 4.10 is a finite geometric series so that

$$\tilde{\phi}(\tau, f) = \frac{T_P}{T} \frac{e^{j2\pi f T} - 1}{e^{j2\pi f T_P} - 1} \tilde{\phi}_P(\tau, f)$$

4.11

Equation 4.11 is the time frequency autocorrelation function. The ambiguity function is easily derived from it by computing $\tilde{\phi}(\tau, f) \tilde{\phi}^*(\tau, f)$. The result is:

$$\theta(\tau, f) = \left(\frac{T_P}{T}\right)^2 \frac{1 - \cos(2\pi fT)}{1 - \cos(2\pi fT_P)} \theta_P(\tau, f) \quad 4.12$$

Taking the limit as f approaches zero one finds that along the delay axis $\theta(\tau, 0)$ equals $\theta_P(\tau, 0)$.

Again using properties three through six and Figure G2 in Appendix G, it is quickly verified that the area of $\theta(\tau, f)$ in the τ, f plane is $2T \cdot 2BW = \frac{4NT_P}{T_B}$. The strips of clear area reduce the strips of non-clear area such that the non-clear area is approximately $\frac{4NT_P}{T_B} \times \frac{(2M-1)T_B}{T_P}$. Thus, in order for the volume of the ambiguity function to equal one, the average pedestal height must be approximately $\frac{1}{4N(2M-1)}$.

Now returning to the example illustrated in equations 4.4-4.6, the target energy is as computed in equation 4.4 with $\Delta\tau = \frac{1}{BW} = T_B$.

$$E_t = T_B \cdot 3 \times 10^{-7} \quad 4.13$$

To evaluate the received clutter energy, a worst case situation will be assumed; i.e., the target is located in the range cell adjacent to the nearest vessel wall. Figure 4.8 shows the spatial relationships between the target, the clutter, and the approximate ambiguity function associated with the transmitted signal.

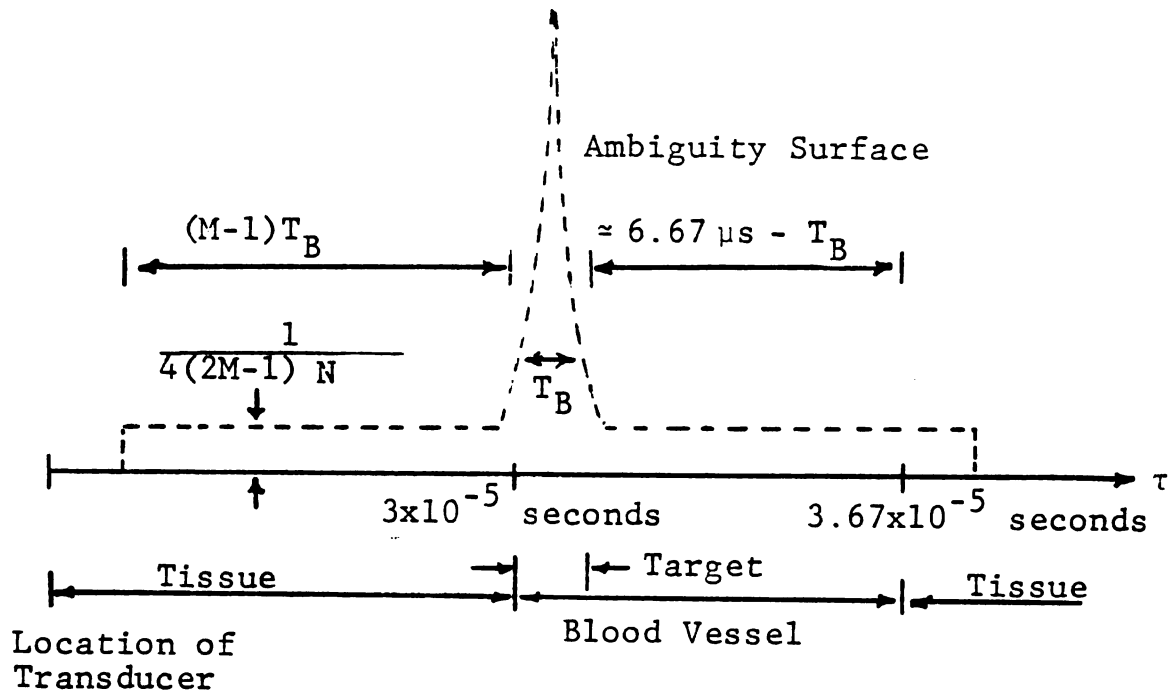


Figure 4.8 Geometry for Clutter Computations

The clutter computations are as follows and parallel those associated with equation 4.5.

$$E_C = I_1 + I_2 + I_3 \quad 4.14$$

$$I_1 = \int_{3 \times 10^{-5}}^{3 \times 10^{-5}} \exp[-3.45 \times 10^5 \cdot \tau] \frac{1}{4N(2M-1)} d\tau$$

$$= \frac{2.3 \times 10^{-11}}{N(2M-1)} (\exp[3.45 \times 10^5 \cdot (M-1)T_B] - 1)$$

$$I_2 = \begin{cases} \frac{6.7 \times 10^{-6} - T_B}{4N(2M-1)} \cdot 3 \times 10^{-7} & (M-1)T_B > 6.7 \times 10^{-6} \\ \frac{(M-1)T_B}{4N(2M-1)} \cdot 3 \times 10^{-7} & (M-1)T_B \leq 6.7 \times 10^{-6} \end{cases}$$

$$I_3 = \begin{cases} \int_{3 \times 10^{-5} + T_B}^{3 \times 10^{-5} + MT_B} \exp[-3.45 \times 10^5 \cdot \tau] \frac{1}{4N(2M-1)} d\tau \\ \frac{2.3 \times 10^{-11}}{N(2M-1)} (1 - \exp[-3.45 \times 10^5 \cdot (M-1)T_B]) & (M-1)T_B > 6.7 \times 10^{-6} \\ 0 & (M-1)T_B \leq 6.7 \times 10^{-6} \end{cases}$$

It is easily verified that E_C is a monotonically increasing function of M which is approximately flat for $M \lesssim 4$. For $M \lesssim 4$ the exponential in I_1 is reasonably well approximated by the first two terms of a Taylor series (assuming T_B to be on the order of 1×10^{-6}). Thus, I_1 , I_2 and I_3 are given approximately as:

$$\begin{aligned} I_1 &\approx \frac{2.3 \times 10^{-11}}{N(2M-1)} \cdot 3.45 \times 10^5 (M-1)T_B \\ &= 8 \times 10^{-6} T_B \frac{M-1}{N(2M-1)} \end{aligned} \quad 4.15$$

$$I_2 \approx 7.5 \times 10^{-8} \cdot T_B \frac{M-1}{N(2M-1)} \quad 4.16$$

$$I_3 \approx 0 \quad 4.17$$

And the total energy is approximately I_1 .

$$E_C \approx 8 \times 10^{-6} T_B \frac{M-1}{N(2M-1)} \quad M \leq 4 \quad 4.18$$

Therefore, for $M \leq 4$, the signal-to-clutter ratio is:

$$\begin{aligned} \text{SCR} = \frac{E_t}{E_C} &= \frac{T_B \times 3 \times 10^{-7}}{\frac{M-1}{N(2M-1)} T_B \cdot 8 \times 10^{-6}} \\ &= 3.75 \times 10^{-2} \frac{(2M-1) N}{M-1} \end{aligned} \quad 4.19$$

In major blood vessels such as the aorta where high velocities are encountered, the signal durations employed can be on the order of .001 seconds or less. (The reasons will become apparent in a later chapter.) Thus N can take on values less than or equal to approximately ten. Without resorting to a periodic pulse train by setting M equal to one, the maximum signal-to-clutter ratio is obtained for M equals two. Even for this signal, the signal-to-clutter ratio is approximately zero db and therefore not adequate for reliable blood flow imaging. The overwhelming effect of the vessel wall is obvious. In order for a signal to be usable, the vessel wall must lie in a clear area of its ambiguity function. Thus, for the instrument to make reliable velocity measurements over as much of the vessel as possible, the periodic pulse train appears to be the only reasonable signal choice.

11

12

13

14

15

16

17

18

19

All that remains to be accomplished in this chapter is to show that the Doppler resolution of the periodic pulse train using a true correlation receiver is approximately that indicated by the conventional ambiguity function.

The transmitted signal shown in Figure 4.5 may be written analytically as

$$\tilde{f}(t) = \sqrt{\frac{T_P}{T_B T}} \sum_{k=0}^{\frac{T}{T_P} - 1} \pi\left(\frac{t - kT_P}{T_B}\right) \quad 4.20$$

where

$$\pi(x) = \begin{cases} 0 & |x| > \frac{1}{2} \\ 1 & |x| < \frac{1}{2} \end{cases}$$

Along the Doppler axis (i.e., $\tau=0$) the generalized time frequency autocorrelation function is

$$\begin{aligned} \tilde{\phi}'(0, f_1, f_2) = \int \left\{ \tilde{f}\left[\left(1 + \frac{f_1}{f_c}\right)t\right] e^{j2\pi f_1 t} \right. \\ \left. \cdot \tilde{f}^*\left[\left(1 + \frac{f_2}{f_c}\right)t\right] e^{j2\pi f_2 t} \right\} dt \end{aligned} \quad 4.21$$

If f_2 is assumed greater than f_1 , and f_1 and f_2 are both assumed small compared to f_c , then by substituting equation 4.20 into 4.21 an expression for $\tilde{\phi}'(0, f_1, f_2)$ can be derived.

For convenience, $\alpha_1 = \frac{f_1}{f_c}$ and $\alpha_2 = \frac{f_2}{f_c}$.

$$\begin{aligned} \tilde{\phi}'(0, f_1, f_2) \approx \frac{T_P}{T} \sum_k \frac{1}{T_B} \int_{\frac{kT_P - \frac{T_B}{2}}{1 + \alpha_1}}^{\frac{kT_P + \frac{T_B}{2}}{1 + \alpha_2}} \pi \left(\frac{t - \frac{kT_P}{1 + \alpha_1}}{T_B} \right) \\ \cdot \pi \left(\frac{t - \frac{kT_P}{1 + \alpha_2}}{T_B} \right) e^{j2\pi(f_1 - f_2)t} dt \end{aligned} \quad 4.22$$

Using the fact that $\exp \frac{j2\pi(f_1 - f_2)kT_P}{1 + \alpha}$ is approximately $\exp(j2\pi(f_1 - f_2)kT_P)$ for all Dopplers of interest, $\tilde{\phi}'(0, f_1, f_2)$ can be simplified as: (letting $f = f_1 - f_2$)

$$\tilde{\phi}'(0, f) = \frac{T_P}{T} \sum_{k=0}^{\frac{T}{T_P} - 1} C \left(1 - \frac{kT_P}{T_B f_c} f \right) e^{j2\pi kT_P f} \quad 4.23$$

where the function $C(x)$ is defined as $C(x) = 0$ for $x \leq 0$ and $C(x) = x$ for $x > 0$.

Now when $T_P f \ll 1$, the summation in equation 4.23 can be approximated as an integral in the following manner. Note that since pulse repetition rates are generally greater than 10 KHz, $T_P f$ will be less than one for Doppler mismatch less than 10 KHz. An absolute maximum upper limit on Doppler mismatch will be 1 KHz with 500 Hz being more typical.

$$\text{Let } x_k = \frac{kT_P}{T} ; \quad \frac{T_P}{T} = \Delta x$$

$$\begin{aligned}
\tilde{\phi}'(o, f) &= \sum_{k=0}^{\frac{1}{\Delta x} - 1} C\left(1 - \frac{fT}{T_B f_c} k \cdot \Delta x\right) e^{j2\pi fT k \Delta x} \Delta x \\
&\approx \int_{x=0}^1 C\left(1 - \frac{fT}{T_B f_c} x\right) e^{j2\pi fTx} dx
\end{aligned} \tag{4.24}$$

For the case when $fT \leq T_B f_c$, which includes Doppler mismatch up to $f < \frac{T_B f_c}{T} \approx \frac{5}{T}$, then $C(g(x))$ equals $g(x)$ such that: (This approximation is justified since our interest is only in the behavior of $\tilde{\phi}'(\cdot)$ near $fT=1$.)

$$\tilde{\phi}'(o, f) \approx \int_0^1 \left(1 - \frac{fT}{T_B f_c} x\right) e^{j2\pi fTx} dx \tag{4.25}$$

A great deal can be inferred about the behavior of $\tilde{\phi}'(o, f)$ by properly interpreting this integral. With the product of bit period and carrier frequency being typically about 5, the function in parenthesis is nearly constant for $fT < 1$. In that case, $\tilde{\phi}'(o, f)$ can be interpreted as the Fourier transform of a pulse of width fT . This in turn is the well known sinc function with zeros at integer multiples of fT . Therefore, the larger the value of $T_B f_c$, the more closely the conventional ambiguity function approximates the generalized ambiguity function in the vicinity of the central spike.

The generalized ambiguity function along the Doppler axis is computed as the square of the magnitude of $\tilde{\phi}'(o, f)$

the
the
the
the

the
the
the
the

$$\theta'(\omega, f) = |\tilde{\phi}'(\omega, f)|^2 \quad 4.26$$

Table 4.1 shows the results of a numerical evaluation of equation 4.26 using equation 4.21. Additionally, corresponding values for the conventional ambiguity function of the periodic pulse train are given for comparison.

It is clear that for bit period carrier frequency products typically employed, the Doppler resolution using a true correlation receiver is well approximated by the inverse of the signal duration.

Table 4.1 $\theta'(o, fT)$ for a Periodic Pulse Train

$\theta'(o, fT)$					
fT	$T_B f_c$				$\theta(o, fT)$
	2.5	5.0	7.5	10.0	
0.0	1.0	1.0	1.0	1.0	1.0
0.1	.929	.948	.955	.959	.968
0.2	.806	.840	.851	.858	.875
0.3	.651	.693	.708	.715	.737
0.4	.486	.528	.543	.550	.573
0.5	.330	.366	.379	.385	.405
0.6	.200	.255	.235	.240	.254
0.7	.104	.117	.123	.126	.135
0.8	.043	.047	.050	.051	.055
0.9	0.13	0.11	0.11	0.11	0.12
1.0	.004	.001	.000	.000	.000
1.1	.008	.007	.007	.007	.008
1.2	0.16	.019	.020	.022	.024
1.3	0.22	.030	.033	.034	.034
1.4	.024	.035	.038	.040	.047
1.5	.022	.033	.036	.039	.045
1.6	.017	.026	.029	.030	.036
1.7	.012	.016	.018	.019	.023
1.8	.008	.008	.009	.009	.011
1.9	.005	.003	.003	.002	.003
2.0	.004	.001	.000	.000	.000

CHAPTER V

PROCESSING CONSIDERATIONS

In this chapter the reasonableness of using a correlation type receiver is investigated. In part, this is accomplished by deriving a theoretically optimum receiver and comparing its structure with that of the correlation receiver. In so doing certain constraints will be imposed on the design and operation of the correlation receiver if it is to perform in a near optimum fashion.

Transit Time Effects

The major effect causing correlation type receivers to be non-optimum for blood flow imaging is a transit time effect. Briefly, the transit time effect is due to the finite time that moving red blood cells are within the ultrasonic beam. To the receiver, this appears as though the target scattering properties are changing with time, and indeed they are.

As stated in Chapter Three, the covariance function of the received signal is all that is required to derive the optimum receiver. Also, an expression for the covariance function was derived and is repeated here for convenience.

$$\tilde{K}(t_1, t_2) = 2\sigma_b^2 E_t \rho \int_{\substack{\text{target} \\ \text{volume}}} \tilde{g}(t_1) g^*(t_2) dV \quad 5.1$$

$$\tilde{g}(t) = T(\bar{r} + \bar{V}(\bar{r})t) \tilde{f}[(1 + \alpha(\bar{r}))t - \tau(\bar{r})] e^{j\omega(\bar{r})t}$$

Recall that the effective scattering cross section associated with each red blood cell is σ_b^2 . The density of red blood cells is ρ . E_t is the energy in the transmitted signal whose normalized complex envelope is $\tilde{f}(t)$. The Doppler frequency is represented by $\omega(\bar{r})$ and is a function of spatial location \bar{r} . Also, α is directly related to $\omega(\bar{r})$ by $\alpha = \frac{\omega(\bar{r})}{\omega_c}$ where ω_c is the carrier frequency of the transmitted signal. And $\tau(\bar{r})$ is the two-way propagation time to the initial location of each differential volume element. The function which gives rise to the transit time effects is the beam pattern $T(\cdot)$. Notice that as each differential volume element of blood moves through space, the effective scattering is modulated by $T(\cdot)$.

Since the intention is to determine the general effect that transit time has on true correlation receiver performance and not to determine the performance of a specific system, the choice of beam and target shape is somewhat arbitrary. For mathematical convenience a somewhat unusual beam pattern is chosen. As shown in Figure 5.1, a spatially hard limited beam with square cross section and beamwidth B has been chosen.

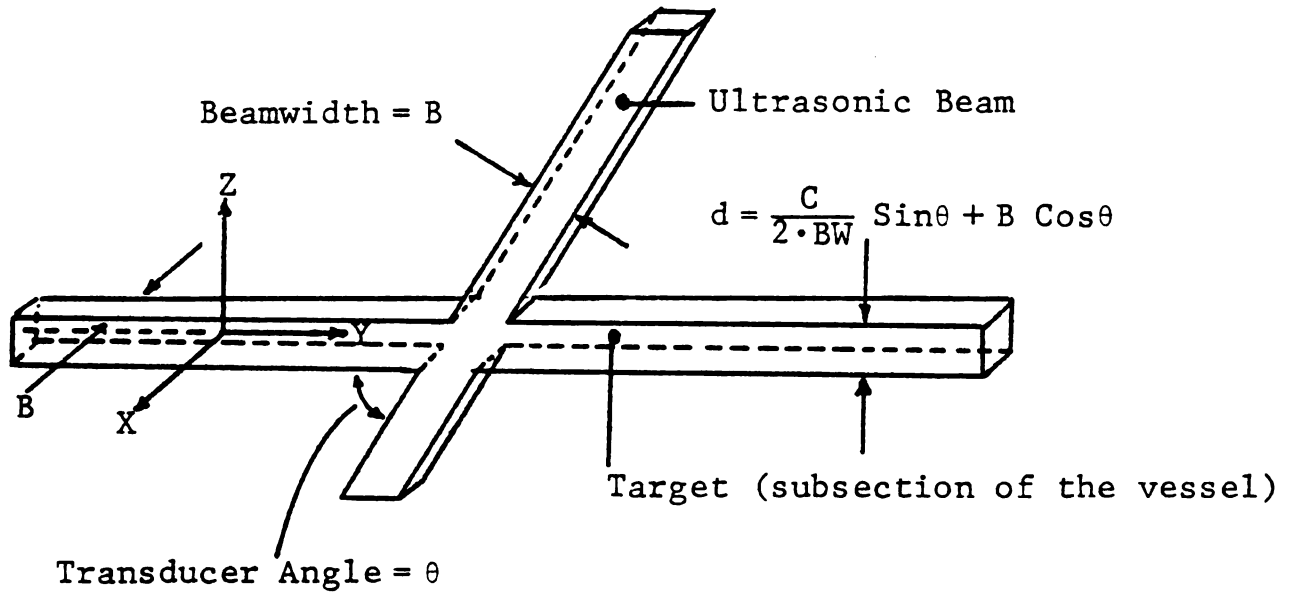


Figure 5.1 Target and Beam Geometry

Temporarily neglecting the relative motion of the target, this choice of beam pattern may be described by $T(\cdot)$ as follows. (The effects of propagation losses are being included in $T(\cdot)$).

$$T(x, y, z) = e^{-\eta\tau/2} \pi\left(\frac{x}{B}\right) \pi\left(\frac{y - \frac{z}{\tan\theta}}{\frac{B}{\sin\theta}}\right) \quad 5.2$$

To be consistent with equation 3.21, the relative motion of the target is included by substituting $x = x + V_x t$, $y = y + V_y t$, $z = z + V_z t$,

$$T(x, y, z) = e^{-\eta\tau/2} \pi \left(\frac{x + V_x t}{B} \right) \pi \left(\frac{y + V_y t - \frac{z + V_z t}{\tan\theta}}{\frac{B}{\sin\theta}} \right) \quad 5.3$$

Additionally, a rectangular target is defined to match the beam pattern and range resolution of the signal.

In order to facilitate the analysis, two assumptions shall be made.

1. The velocity of red blood cells within the target is not a function of spatial location. That is, $\bar{V}(\bar{r}) = V_y \hat{y}$. This also implies that $\omega(\bar{r}) = \omega$ and $\alpha(\bar{r}) = \alpha$.
2. The Doppler shifted received signal was reflected from a stationary fluctuating point target such that $\tau(\bar{r}) = \tau$. (As will be discussed later, this assumption is valid only when true correlation is employed.)

The first assumption is reasonable since, in the center of the vessel where transit time effects are the greatest, the velocity profile is nearly uniform. In Chapter Six further design constraints will be imposed on ultrasonic blood flow measurement systems to account for non-uniform velocity profiles within the target.

Effects which can result from the non-zero range extent of scatterers have been minimized by the target definition. Thus, assuming true correlation processing, assumption two is also reasonable.

Making these assumptions and substituting 5.3 into 5.1:

$$\tilde{K}(t_1, t_2) = 2\sigma_b^2 E_t \rho e^{-\eta\tau} \int_{\text{target}} \tilde{g}_1(t_1) \tilde{g}_1^*(t_2) dV$$

$$\tilde{g}_1(t) = \pi \left(\frac{x}{B} \right) \pi \left(\frac{y + V_y t - \frac{z}{\tan\theta}}{\frac{B}{\sin\theta}} \right) \tilde{f}[(1+\alpha)t - \tau] e^{j\omega t} \quad 5.4$$

Bringing variables which are not functions of space outside the integral, 5.4 may be rewritten as:

$$\tilde{K}(t_1, t_2) = 2\sigma_b^2 E_t \rho e^{-\eta\tau} \tilde{f}[(1+\alpha)t_1 - \tau] e^{j\omega t_1} \quad 5.5$$

$$\cdot I \cdot \tilde{f}^*[(1+\alpha)t_2 - \tau] e^{j\omega t_2}$$

where

$$I = \iiint_{\text{target}} \pi \left(\frac{x}{B} \right) \pi \left(\frac{y + V_y t_1 - \frac{z}{\tan\theta}}{\frac{B}{\sin\theta}} \right) \cdot \pi \left(\frac{y + V_y t_2 - \frac{z}{\tan\theta}}{\frac{B}{\sin\theta}} \right) dx dy dz \quad 5.6$$

Carrying out the integration over x and simplifying the remaining product leaves

$$I = B \iint_{\pi} \left(\frac{y + V_y \left(\frac{t_1 + t_2}{2} \right) - \frac{z}{\tan \theta}}{\frac{B}{\sin \theta} - V_y |t_1 - t_2|} \right) u \left(\frac{B}{\sin \theta} - V_y |t_1 - t_2| \right) dy dz \quad 5.7$$

where $u(\cdot)$ is the unit step function.

Next, the infinite integration on y is carried out leaving

$$I = B \int_{-\frac{d}{2}}^{\frac{d}{2}} \left[\frac{B}{\sin \theta} - V_y |t_1 - t_2| \right] u \left(\frac{B}{\sin \theta} - V_y |t_1 - t_2| \right) dx \quad 5.8$$

where

$$d = \frac{C}{2 \cdot BW} \sin \theta + B \cos(\theta) \quad 5.9$$

Since I equals zero when $\frac{B}{\sin \theta}$ is less than $V_y |t_1 - t_2|$, the integral I can be written in final form as shown in equation 5.10.

$$I = \frac{B^2 d}{\sin \theta} \Lambda(av\lambda) \quad 5.10$$

where

$$\Lambda(x) = \begin{cases} 0 & |x| < 1 \\ |x| & |x| < 1 \end{cases}$$

$$a = \frac{\sin \theta}{B}$$

$$\lambda = t_1 - t_2$$

$$v = V_y$$

$$av = \frac{1}{\text{transmit time of red blood cells across the beam}}$$

And finally, the covariance function may be written in its final form.

$$\tilde{K}(t_1, t_2) = K \tilde{f}[(1+\alpha)t_1 - \tau] \Lambda(av\lambda) \tilde{f}^*[(1+\alpha)t_2 - \tau] e^{j\omega\lambda} \quad 5.11$$

where

$$K = \frac{B_d^2}{\sin\theta} 2\sigma_b^2 E_t \rho e^{-\eta\tau}$$

= average signal energy received from the defined target.

Derivation of the Optimum Detector in the Presence of Transit Time Effects

Because the process is Gaussian, equation 5.11 contains all the information required to derive the optimum detector. One well known form of the optimum receiver for minimum probability of error is shown in Appendix D, Figure D.4, and reproduced here slightly modified.

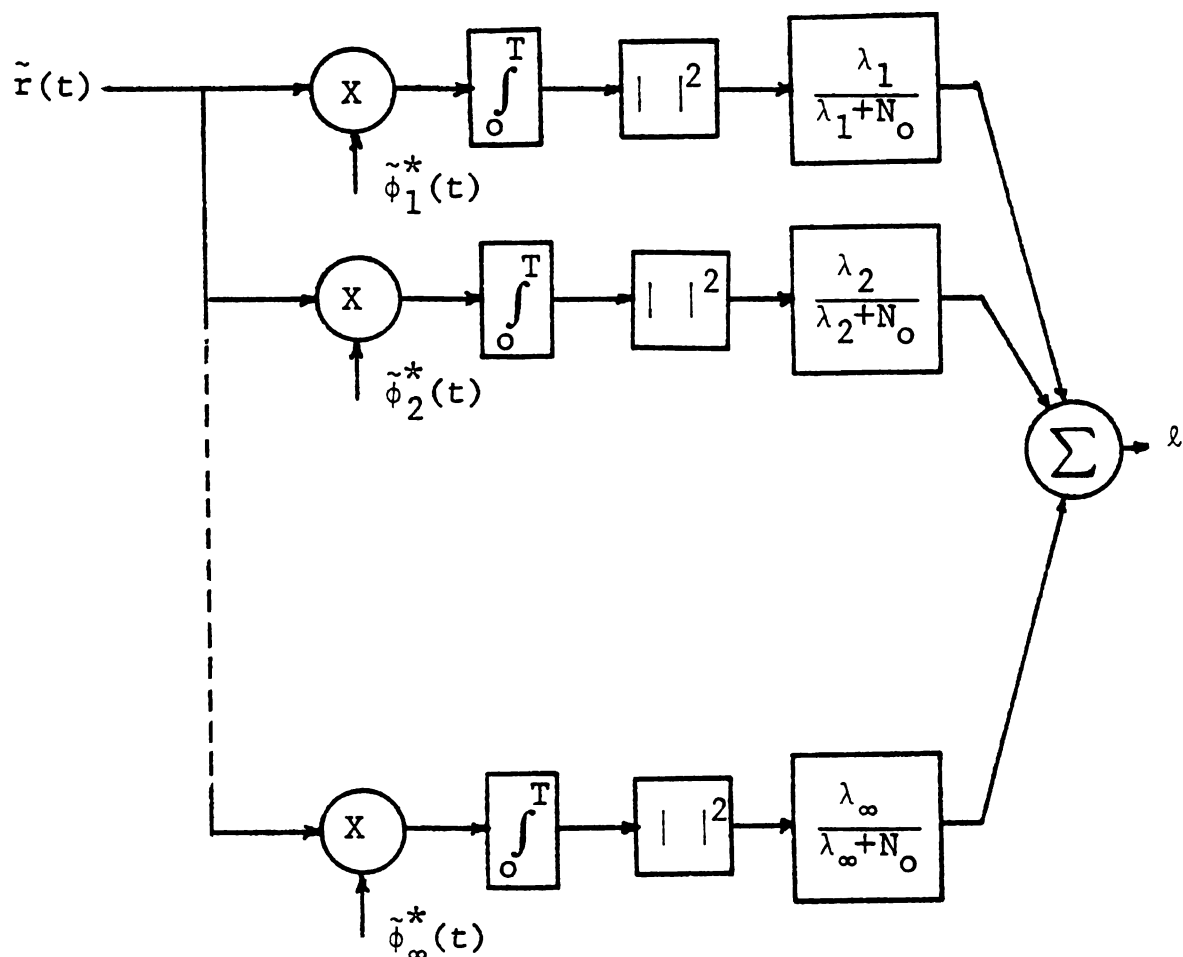


Figure 5.2 Optimum Detector

In this detector a target is determined to be present at the specified range with the estimated velocity if, and only if, the output ℓ is greater than some threshold γ . In this figure N_0 is the average received noise energy in the direction of each Eigenfunction $\tilde{\phi}_i(t)$, where the set $\{\tilde{\phi}_i(t)\}$ are Eigenfunctions of the signal process and solve the integral equation 5.12.

$$\begin{aligned}
 \lambda \tilde{\phi}(t) &= \int_{-\frac{T}{2}}^{\frac{T}{2}} \tilde{K}(t, u) \tilde{\phi}(u) du \\
 &= \int_{-\frac{T}{2}}^{\frac{T}{2}} K \cdot \tilde{f}(t) \Lambda(av(t-u)) \tilde{f}^*(u) e^{j\omega(t-u)} \tilde{\phi}(u) du
 \end{aligned}
 \tag{5.12}$$

Without loss of generality, the target delay has been assumed to be zero, $\tau = 0$, and the envelope compression factor α has been left out since it does not affect the solution. Also, T is the signal duration and a symmetric signal has been assumed.

Clearly, for any u in the interval $(-\frac{T}{2}, \frac{T}{2})$, any representation of $\Lambda(av(t-u))$ which equals $\Lambda(av(t-u))$ for all t in the interval $(-\frac{T}{2}, \frac{T}{2})$, may be used. Specifically, a periodic approximation, $\Lambda_p(av(t-u))$, with a fundamental period of at least $2T$ which equals $\Lambda(av(t-u))$ on the interval $(-\frac{T}{2}, \frac{T}{2})$ is an accurate representation.

By approximating $\Lambda_p(av(t-u))$ as a modified $k+1$ term Fourier series with a fundamental period of $2N$ times the signal duration, the integral equation of 5.12 can be made separable. The modified Fourier series representation of $\Lambda(av\lambda)$ is:

$$\Lambda(av\lambda) = \sum_{n=0}^k a_n \cos\left(\frac{2\pi n}{2NT} \lambda\right)$$

5.13

$$a_n = \frac{C_n}{\sum_{i=0}^k C_i}$$

Where C_n is the standard Fourier coefficient which is computed using well known formulas.

$$C_0 = \frac{1}{2NT} \int_{-NT}^{NT} \Lambda(av\lambda) d\lambda$$

$$= \frac{1}{NT} \int_0^{NT} (1 - av\lambda) \pi\left(\frac{av\lambda}{2}\right) d\lambda$$

$$= \begin{cases} 1 - \frac{NavT}{2} & avT < \frac{1}{N} \\ \frac{1}{2NavT} & avT \geq \frac{1}{N} \end{cases}$$

$$C_n = \frac{2}{2NT} \int_{-NT}^{NT} \Lambda(av\lambda) \cos\left(\frac{2\pi n}{2NT} \lambda\right) d\lambda$$

$$= \frac{2}{NT} \int_0^{NT} (1 - av\lambda) \pi\left(\frac{av\lambda}{2}\right) \cos\left(\frac{2\pi n}{2NT} \lambda\right) d\lambda$$

$$\underline{\text{For } avT < \frac{1}{N}}$$

$$C_n = \begin{cases} 0 & n = \text{even} \\ \frac{4NavT}{(\pi n)^2} & n = \text{odd} \end{cases}$$

$$\underline{\text{For } avT \geq \frac{1}{N}}$$

$$C_n = \frac{2NavT}{(\pi n)^2} (1 - \cos(\frac{\pi n}{NavT}))$$

In the expansion of equation 5.13 the normalization of the standard Fourier coefficients was necessary to insure that $\Lambda(0) = 1$.

By letting β equal avT , where T is the signal duration, then β represents the ratio of signal duration to transmit time. The coefficients C_n may now be rewritten to emphasize their dependence on β .

$$\underline{\text{For } \beta < \frac{1}{N}}$$

$$C_0 = 1 - \frac{N}{2} \beta$$

$$C_n = \begin{cases} 0 & n = \text{even} \\ \frac{4n\beta}{(\pi n)^2} & n = \text{odd} \end{cases}$$

5.14

$$\text{For } \beta \geq \frac{1}{N}$$

$$C_o = \frac{1}{2N\beta}$$

5.15

$$C_n = \frac{2N\beta}{(\pi n)^2} (1 - \cos(\frac{\pi n}{N\beta}))$$

Also, to show explicitly the dependence on β , $\Lambda_p(\text{av}\lambda)$ may be written as $\Lambda_p(\beta \frac{\lambda}{T})$. A plot of $\Lambda_p(\beta \frac{\lambda}{T})$ using $N=2.5$ and a six term expansion for various values of β is shown in Figure 5.3. Notice that a six term expansion implies that k equals 5 in equation 5.13.

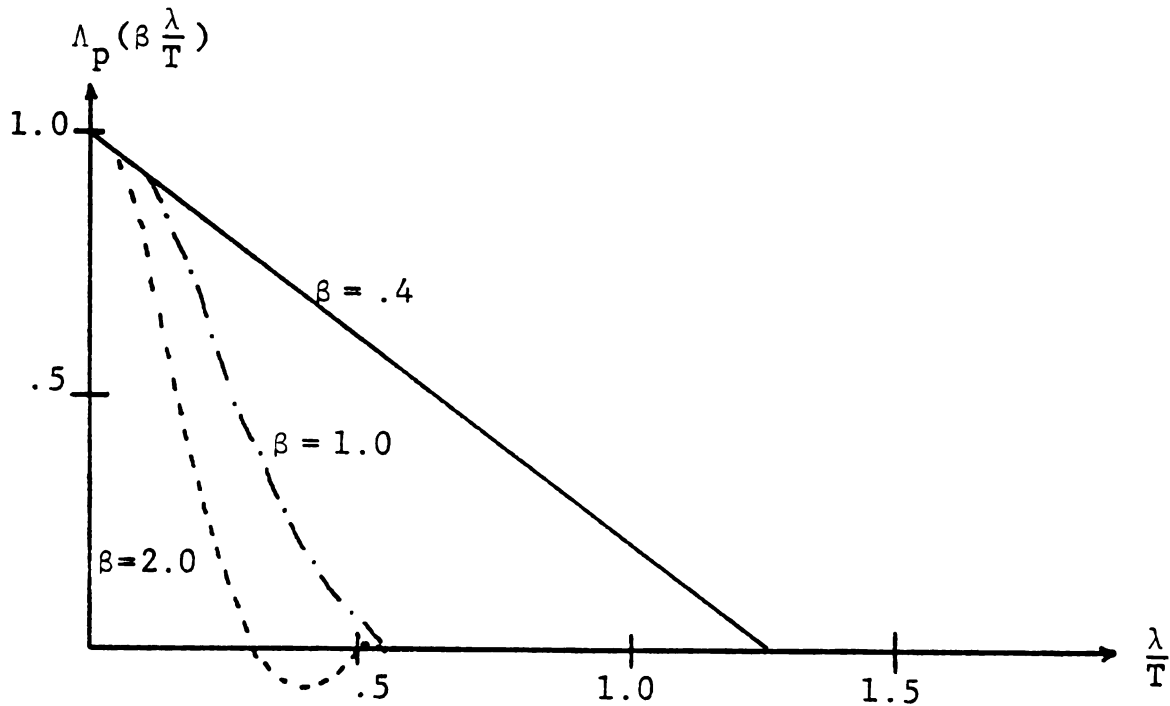


Figure 5.3 Approximate $\Lambda_p(\beta \frac{\lambda}{T})$

$\Lambda(av\lambda)$, given by equation 5.13, is transformed to a separable form using the common trigonometric identity:

$$\cos(x-y) = \cos(x)\cos(y) + \sin(x)\sin(y)$$

Then, letting $\omega_n = \frac{\pi n}{NT}$ and $\lambda = t-u$;

$$\begin{aligned} \Lambda(av(t-u)) &= a_0 + \sum_{n=1}^k a_n \cos(\omega_n t) \cos(\omega_n u) \\ &\quad + \sum_{n=1}^k a_n \sin(\omega_n t) \sin(\omega_n u) \end{aligned} \tag{5.16}$$

And finally, the integral equation of 5.12 may be written in a separable form.

$$\lambda \tilde{\phi}(t) = \int_{-\frac{T}{2}}^{\frac{T}{2}} \sum_{j=1}^{2k+1} \tilde{M}_j(t) \tilde{N}_j(u) \tilde{\phi}(u) du \tag{5.17}$$

where

$$M_1(t) = \sqrt{a_0 K} \tilde{f}(t) e^{j\omega t}$$

$$M_{2n}(t) = \sqrt{a_n K} \cos\left(\frac{\pi n}{NT} t\right) \tilde{f}(t) e^{j\omega t}$$

$$M_{2n+1}(t) = \sqrt{a_n K} \sin\left(\frac{n\pi}{NT} t\right) \tilde{f}(t) e^{j\omega t}$$

$$\tilde{N}_i(t) = \tilde{M}_i^*(t)$$

From this equation the Eigenvalues and Eigenfunctions of $\tilde{K}(t,u)$ may be determined. First, the order of integration and summation are interchanged so that

$$\lambda \tilde{\phi}(t) = \sum_{j=1}^{2k+1} \tilde{M}_j(t) \int_{-\frac{T}{2}}^{\frac{T}{2}} \tilde{N}_j(u) \tilde{\phi}(u) du \quad 5.18$$

Letting the integral equal \tilde{C}_j

$$\lambda \tilde{\phi}(t) = \sum_{j=1}^{2k+1} \tilde{M}_j(t) \cdot \tilde{C}_j \quad 5.19$$

Multiplying both sides by $\tilde{N}_i(t)$ and integrating:

$$\int_{-\frac{T}{2}}^{\frac{T}{2}} \tilde{\phi}(t) \tilde{N}_i(t) dt = \sum_{j=1}^{2k+1} \int_{-\frac{T}{2}}^{\frac{T}{2}} \tilde{M}_j(t) \tilde{N}_i(t) dt \cdot \tilde{C}_j \quad 5.20$$

Letting $\alpha_{i,j} = \int_{-T/2}^{T/2} \tilde{M}_j(t) \cdot \tilde{N}_i(t) dt$

$$\lambda \tilde{C}_i = \sum_{j=1}^{2k+1} \alpha_{i,j} \tilde{C}_j \quad 5.21$$

Or, in matrix notation:

$$\lambda \bar{C} = A \bar{C} \quad 5.22$$

Therefore, the Eigenvalues of the signal process are the Eigenvalues of the $2k+1$ by $2k+1$ matrix A . Also, if the

optimum receiver were to be implemented, then the Eigenfunctions could be generated as follows (from equation 5.19):

$$\tilde{\phi}_i(t) = \frac{1}{\lambda_i} \sum_{j=1}^{2k+1} \tilde{C}_{i,j} \tilde{M}_j(t) \quad 5.23$$

Where C_{ij} is the j^{th} component of the normalized Eigenvector associated with λ_i .

The computation of the elements of A, α_{ij} , is somewhat laborious and is carried out in Appendix J. In the derivation it is assumed that $T_p \ll \frac{2NT}{n}$ which is reasonable for all cases of interest. The elements of A are summarized below.

$$\alpha_{11} = a_o K \quad 5.24$$

$$\alpha_{1,2n} = \frac{2K\sqrt{a_o a_n}}{f_n} \sin(f_n/2) \quad 5.25$$

$$\alpha_{2n,2n} = \frac{Ka_n}{2f_n} (f_n + \sin(f_n)) \quad 5.26$$

$$\alpha_{2n+1,2n+1} = \frac{Ka_n}{2f_n} (f_n - \sin(f_n)) \quad 5.27$$

$$\alpha_{2n,2m}^{n \neq m} = K\sqrt{a_n a_m} \left[\frac{\sin(\frac{f_{n+m}}{2})}{f_{n+m}} + \frac{\sin(\frac{f_{n-m}}{2})}{f_{n-m}} \right] \quad 5.28$$

$$\alpha_{2n+1, 2m+1} = K \sqrt{a_n a_m} \left[\frac{\sin\left(\frac{f_{n+m}}{2}\right)}{f_{n+m}} - \frac{\sin\left(\frac{f_{n-m}}{2}\right)}{f_{n-m}} \right] \quad 5.29$$

$$\alpha_{2n, 1} = \alpha_{1, 2n} \quad 5.30$$

where

$$\beta = avT = \frac{T}{[av]^{-1}} = \frac{\text{Signal Duration}}{\text{Transit Time}} \quad 5.31$$

$$f_n = \frac{n\pi}{N} \quad 5.32$$

The remaining entries are zero.

Having determined the entries of the A matrix, the Eigenvalues and Eigenfunctions can be computed and the optimum detector could be implemented. It is interesting to note, as can be seen by studying the Fourier coefficients, that only one parameter has any effect on the receiver structure. That parameter is β , the ratio of signal duration to transit time. Later in this chapter an interesting interpretation of β will be given which will be the basis for comparing Doppler resolution of the true correlation and conventional correlation receivers.

Performance of the Optimum Detector in the Presence of Transit Time Effects

Begin by observing equation D.15 and its implementation in Figure 5.2. If equal apriori probabilities are assumed, then for minimum probability of error γ' equals one and the receiver decision threshold becomes

$$\gamma = \sum_{i=1}^{2k+1} N_o \ln \left(\frac{\lambda_i}{N_o} + 1 \right) \quad 5.33$$

This threshold is then used in the computation of the probability of detection (P_D) and the probability of false alarm (P_F).

$$P_D = \int_{\gamma}^{\infty} p(\ell | \text{target is present}) \quad 5.34$$

$$P_F = \int_{\gamma}^{\infty} p(\ell | \text{target is absent}) \quad 5.35$$

$$\ell = \sum_{i=1}^{2k+1} y_i \quad (\text{see Figure 5.2}) \quad 5.36$$

Before the integrals of equations 5.34 and 5.35 can be completed, the density functions which describe ℓ on both hypotheses must be determined. Since ℓ is the sum of independent random variables, the characteristic function for $p(\ell | \text{target present})$ may be determined by multiplying the characteristic functions of the individual random variables.

Before this can be completed, however, the probability density of y_i , given that a target is present, must be determined.

First, note that because $\tilde{r}(t)$ is assumed to be a Gaussian process, then each \tilde{r}_i is an independent Gaussian random variable with mean and variance given as follows:

$$\begin{aligned}
 E\{\tilde{r}_i\} &= E\{\int (\tilde{r}(t) + \tilde{w}(t)) \tilde{\phi}_i(t) dt\} \\
 &= \int E\{\tilde{r}(t) + \tilde{w}(t)\} \tilde{\phi}_i(t) dt \\
 &= 0
 \end{aligned} \tag{5.37}$$

$$\begin{aligned}
 E\{\tilde{r}_i \tilde{r}_i^*\} &= E\{\int (\tilde{r}(t) + \tilde{w}(t)) \tilde{\phi}_i(t) dt \\
 &\quad \cdot \int (\tilde{r}(u) + \tilde{w}(u))^* \tilde{\phi}_i^*(u) du\} \\
 &= \int \int \tilde{\phi}_i(t) [\tilde{K}(t, u) + N_o \delta(t - u)] \tilde{\phi}_i^*(u) du dt
 \end{aligned} \tag{5.38}$$

Using Mercers theorem (Property 1, Appendix D) to replace $\tilde{K}(t, u)$:

$$\begin{aligned}
 E\{|\tilde{r}_i|^2\} &= \int \int \tilde{\phi}_i(t) \left[\sum_j \lambda_j \tilde{\phi}_j(t) \tilde{\phi}_i^*(u) \right] \tilde{\phi}_i^*(u) dt du \\
 &\quad + \int N_o \tilde{\phi}_i(t) \tilde{\phi}_i^*(t) dt
 \end{aligned} \tag{5.39}$$

And finally, using the orthonormality of the Eigenfunctions $\{\tilde{\phi}_i(t)\}$:

$$E\{|\tilde{r}_i|^2\} = \lambda_i + N_o \quad 5.40$$

Using equations C22 and C24 from Appendix C, the probability density function for the magnitude of \tilde{r}_i is written immediately as:

$$p_{|\tilde{r}_i|}(|r_i|) = \frac{2|\tilde{r}_i|}{\lambda_i + N_o} \exp\left(-\frac{|\tilde{r}_i|^2}{\lambda_i + N_o}\right) \quad 5.41$$

Letting y_i equal the random variable input to the summer, its probability density may be determined by appropriately transforming the probability density governing $|\tilde{r}_i|$.

$$\begin{aligned} y_i &= \frac{\lambda_i}{\lambda_i + N_o} |\tilde{r}_i|^2 \\ dy_i &= \frac{2\lambda_i}{\lambda_i + N_o} |\tilde{r}_i| d|\tilde{r}_i| \\ f^{-1}(y_i) &= \sqrt{\frac{\lambda_i + N_o}{\lambda_i}} y_i \\ p_{y_i}(y_i) &= p_{|\tilde{r}_i|}(f^{-1}(y_i)) \left| \frac{d|\tilde{r}_i|}{dy} \right| \end{aligned}$$

Making the appropriate substitutions:

$$p(y_i | \text{target is present}) = \frac{1}{\lambda_i} e^{-\frac{y_i}{\lambda_i}} \quad 5.42$$

Similarly, $p(y_i | \text{target absent})$ may be obtained from $p(|\tilde{r}_i| | \text{target absent})$.

$$p(|\tilde{r}_i| | \text{target is absent}) = \frac{2|\tilde{r}_i|}{N_o} e^{-\frac{|\tilde{r}_i|^2}{N_o}}$$

Carrying out identical steps as for $p(y_i | \text{target present})$, the probability density of y_i , given that the target is absent, can be derived. The result is:

$$p(y_i | \text{target is absent}) = \frac{\lambda_i + N_o}{N_o \lambda_i} e^{-\frac{(\lambda_i + N_o)y_i}{N_o \lambda_i}} \quad 5.43$$

Both of these are exponential densities of the general form:

$$p(y_i) = \frac{1}{\beta_i} e^{-\frac{y_i}{\beta_i}} \quad 5.44$$

The characteristic function associated with $p(y_i)$ is easily found by computing the expectation of e^{jvy_i} .

$$\begin{aligned} \phi_{p_i} &= E\{e^{jvy_i}\} = \int_0^\infty e^{jvy_i} \frac{1}{\beta_i} e^{-\frac{y_i}{\beta_i}} dy_i \\ &= \frac{1}{\beta_i} \int_0^\infty e^{(jv - \frac{1}{\beta_i})y_i} dy_i \end{aligned} \quad 5.45$$

or

$$\phi_{p_i} = -\frac{1}{jv\beta_i - 1} \quad 5.46$$

Now since the y_i 's are independent, the characteristic function of their sum, ℓ , is the product of their characteristic functions.

$$\phi_{P_\ell} = \prod_{i=1}^{2k+1} \left(- \frac{1}{jv\beta_i - 1} \right)$$

This in turn may be expanded as a partial fraction expansion of the form

$$\phi_{P_\ell} = \sum_{i=1}^{2k+1} - \frac{P_i}{jv\beta_i - 1} \quad 5.47$$

where

$$P_i = \prod_{\substack{j=1 \\ j \neq i}}^{2k+1} \frac{\beta_i}{\beta_i - \beta_j} \quad 5.48$$

Each term of the expansion is of the same form as ϕ_{P_i} and therefore the probability density associated with ϕ_{P_ℓ} is determined by inspection.

$$P(\ell | H_j) = \sum_{i=1}^{2k+1} \frac{P_i}{\beta_i} e^{-\frac{\ell}{\beta_i}} \quad 5.49$$

where

On H_1 : (target is present)

$$\beta_i = \lambda_i \quad 5.50$$

On H_0 : (target is absent)

$$\beta_i = \frac{\lambda_i N_0}{\lambda_i + N_0} \quad 5.51$$

Substituting 5.49 and 5.50 (5.51) into 5.34 (5.36) and carrying out the integration, the probability of detection (probability of false alarm) is easily determined.

$$P_{D(F)} = \sum_{i=1}^{2k+1} P_i e^{-\frac{Y}{\beta_i}} \quad 5.52$$

The total probability of error (assuming equally likely events) is simply the average total error:

$$P_E = \frac{1}{2} (1 - P_D + P_F) \quad 5.53$$

Notice that if the transit time of red blood cells were infinity, then $\Lambda(\beta \frac{\lambda}{T})$ would simply be a constant value of one for all λ . In the Fourier series expansion of $\Lambda(\beta \frac{\lambda}{T})$, a_0 would equal one and all other coefficients would be zero. As a result, all entries of A would be zero except a_{11} which would equal K , the total expected received signal energy. Therefore, the first component of the associated Eigenvector would equal one, and all other components would be zero. Thus, in this degenerate case the correlation receiver is identically the optimum receiver.

Performance of the Correlation Detector in the Presence of Transit Time Effects

Figure 5.4 shows the operations involved in a correlation type detector. As shown, the received signal consists of the reflected signal plus additive noise. Both $\tilde{r}(t)$ and $\tilde{w}(t)$ are assumed to be sample functions from independent zero mean complex Gaussian processes. Additionally, $\tilde{w}(t)$ is assumed white.

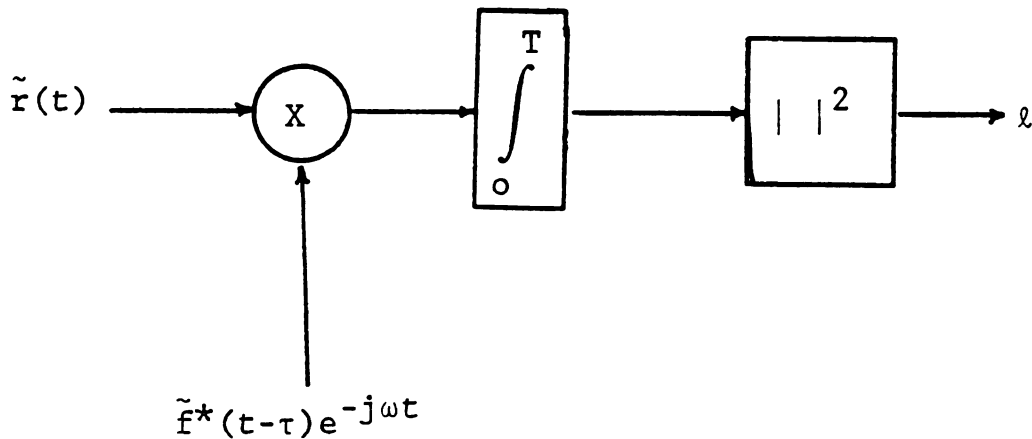


Figure 5.4 Correlation Detector

In order to determine the performance capability of the correlation detector, two pieces of information are required: (1) the threshold, and (2) the probability density function governing ℓ .

Having already derived a probability of error expression for the optimum receiver simplifies the task of deriving a similar expression for a correlation receiver perfectly matched to the target Doppler. Since many of the detailed computations are identical, they need not be repeated.

Because $\tilde{r}(t)$ and $\tilde{w}(t)$ are zero mean processes, \tilde{r} is a zero mean random variable with a mean value equal to zero.

$$\begin{aligned}
 E\{\tilde{r}\} &= E\{\int (\tilde{r}(t) + \tilde{w}(t)) \tilde{f}^*(t) e^{-j\omega t} dt\} \\
 &= \int E\{\tilde{r}(t) + \tilde{w}(t)\} \tilde{f}^*(t) e^{-j\omega t} dt \\
 &= 0
 \end{aligned} \tag{5.54}$$

Finding the variance of \tilde{r} is somewhat more involved.

$$\begin{aligned}
 E\{\tilde{r}\tilde{r}^*\} &= E\{\int (\tilde{r}(t) + \tilde{w}(t)) \tilde{f}^*(t) e^{-j\omega t} dt \\
 &\quad \cdot \int (\tilde{r}(u) + \tilde{w}(u))^* \tilde{f}(u) e^{j\omega u} du\}
 \end{aligned} \tag{5.55}$$

$$\begin{aligned}
 E\{\tilde{r}\tilde{r}^*\} &= \int \int \tilde{f}^*(t) E\{(\tilde{r}(t) + \tilde{w}(t)) (\tilde{r}^*(u) + \tilde{w}^*(u))\} \\
 &\quad \cdot \tilde{f}(u) e^{j\omega(u-t)} dt du
 \end{aligned} \tag{5.56}$$

Because $E\{\tilde{r}(t)\tilde{w}(t)\} = 0$, the expectation may be simplified as follows:

$$\begin{aligned}
& E\{(\tilde{r}(t) + \tilde{w}(t))(\tilde{r}^*(u) + \tilde{w}^*(u))\} \\
& = E\{\tilde{r}(t)\tilde{r}^*(u)\} + E\{\tilde{w}(t)\tilde{w}^*(u)\}
\end{aligned} \tag{5.57}$$

The first expectation is just the covariance function which was originally defined in equation 3.13. Eventually, this covariance was determined to be as given by equation 5.11. Assuming the noise to be white, the second expectation is simply $N_0 \delta(t-u)$. Making these substitutions into equation 5.56, the expression for the variance of \tilde{r} becomes:

$$\begin{aligned}
E\{\tilde{r}\tilde{r}^*\} &= K \iint \tilde{f}^*(t) \tilde{f}(t) \Lambda(av\lambda) \tilde{f}^*(u) \tilde{f}(u) dt du \\
&+ \iint \tilde{f}^*(t) N_0 \delta(t-u) \tilde{f}(u) dt du
\end{aligned} \tag{5.58}$$

Using the normality of $\tilde{f}(t)$ and the Fourier approximation for $\Lambda(av(t-u))$ given by equation 5.13, equation 5.58 expands to:

$$\begin{aligned}
E\{\tilde{r}\tilde{r}^*\} &= K \iint |\tilde{f}(t)|^2 a_0 |\tilde{f}(u)|^2 dt du \\
&+ K \iint |\tilde{f}(t)|^2 \left[\sum_{n=1}^k a_n \cos(\omega_n t) \cos(\omega_n u) \right] |\tilde{f}(u)|^2 dt du \\
&+ K \iint |\tilde{f}(t)|^2 \left[\sum_{n=1}^k a_n \sin(\omega_n t) \sin(\omega_n u) \right] |\tilde{f}(u)|^2 dt du \\
&+ N_0
\end{aligned} \tag{5.59}$$

Each of these terms are directly related to the elements of the A matrix so that:

$$E\{\tilde{r}\tilde{r}^*\} = \alpha_{1,1} + \sum_{n=1}^k \frac{\alpha_{1,2n}^2}{\alpha_{1,1}} + \sum_{n=1}^k \frac{\alpha_{1,2n+1}^2}{\alpha_{1,1}} + N_o \quad 5.60$$

But, as shown in Appendix J, $\alpha_{1,2n+1} = 0$. Also, defining $E\{\tilde{r}\tilde{r}^*\}$ in the absence of noise as \bar{E}_c , a measure of the correlated energy, the variance of r may be written as:

$$E\{\tilde{r}\tilde{r}^*\} = \bar{E}_c + N_o \quad 5.61$$

where \bar{E}_c is given by:

$$\begin{aligned} \bar{E}_c &= K \left[\alpha_{1,1} + \sum_{n=1}^k \frac{\alpha_{1,2n}^2}{\alpha_{1,1}} \right] \\ &= K \left[a_o + \sum_{n=1}^k a_n \text{sinc}^2 \left(\frac{n\tau}{NT} \right) \right] \end{aligned} \quad 5.62$$

Figure 5.5 shows the dependence of \bar{E}_c on β , where β is the ratio of signal duration to transit time and provides the first indication as to the effect β has on correlation detector performance. As shown, the signal energy at the output of the correlation receiver decreases as β increases.

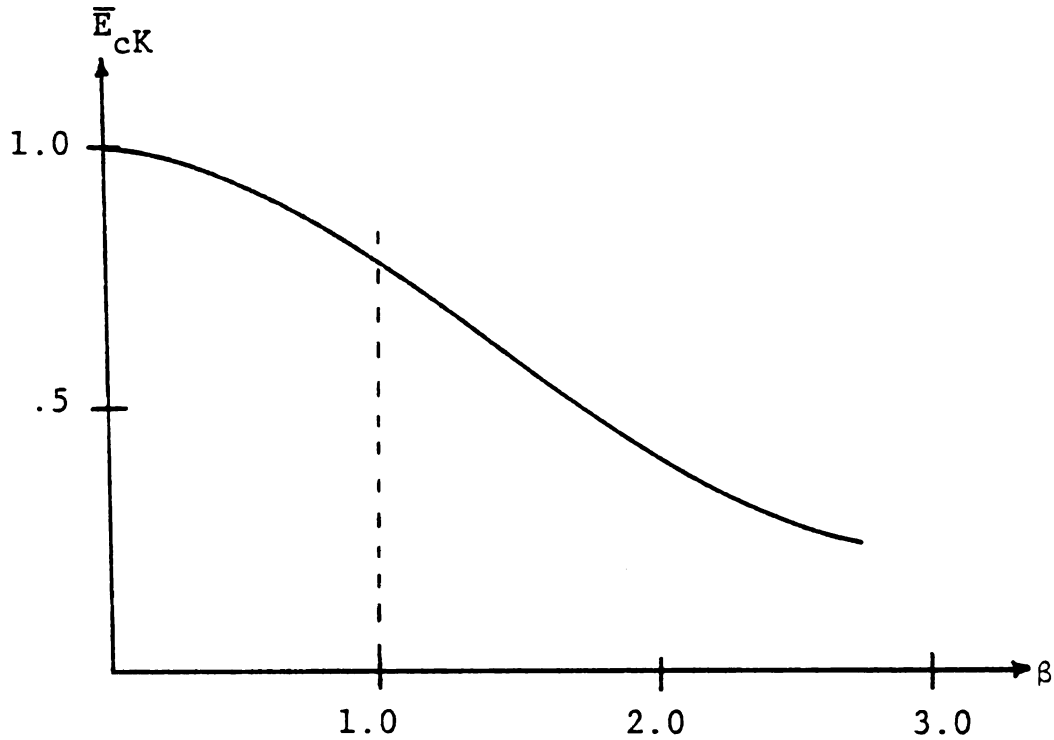


Figure 5.5 Correlated Energy Function

Before the implications of this relationship are discussed in the next section, the probability of error for the correlation detector is derived.

The magnitude of $|\tilde{r}|$ has a Rayleigh density of the form

$$p(|\tilde{r}| | \text{target is present}) = \frac{2|\tilde{r}|}{\bar{E}_c + N_o} e^{-\frac{|\tilde{r}|^2}{\bar{E}_c + N_o}} \quad 5.63$$

The derivation of the density of $p(|\tilde{r}|^2)$ follows the same procedure as that used to derive equation 5.42. Therefore, the details of the derivation have been omitted. The result is:

$$p(\ell | \text{target is present}) = \frac{1}{\bar{E}_c + N_o} e^{-\frac{\ell}{\bar{E}_c + N_o}} \quad 5.64$$

$$p(\ell | \text{target is absent}) = \frac{1}{N_o} e^{-\frac{\ell}{N_o}} \quad 5.65$$

The likelihood ratio and the associated test for minimum probability of error is given by the following equation. To ensure results consistent with those for the optimum detector, equal apriori probabilities have been assumed.

$$\text{LRT} = \frac{\frac{1}{\bar{E}_c + N_o} e^{-\frac{\ell}{\bar{E}_c + N_o}}}{\frac{1}{N_o} e^{-\frac{\ell}{N_o}}} \geq 1$$

$$\frac{N_o}{\bar{E}_c + N_o} e^{\ell \left(\frac{\bar{E}_c}{N_o (\bar{E}_c + N_o)} \right)} \geq 1 \quad 5.66$$

By taking the logarithm of both sides, an equivalent test is:

$$\ell \geq \gamma$$

$$\gamma = \frac{N_o (\bar{E}_c + N_o)}{\bar{E}_c} \ln \left(\frac{\bar{E}_c + N_o}{N_o} \right) \quad 5.67$$

The probabilities of correlation detection and false alarm may now be computed.

$$\begin{aligned}
 P_{CD} &= \int_{\gamma}^{\infty} p(\ell | \text{target present}) d\ell \\
 &= \int_{\gamma}^{\infty} \frac{1}{\bar{E}_c + N_o} \exp\left(-\frac{\ell}{\bar{E}_c + N_o}\right) d\ell \\
 &= \exp\left(-\frac{N_o}{\bar{E}_c} \ln\left(\frac{\bar{E}_c + N_o}{N_o}\right)\right)
 \end{aligned} \tag{5.68}$$

$$\begin{aligned}
 P_{CF} &= \int_{\gamma}^{\infty} p(\ell | \text{target absent}) d\ell \\
 &= \int_{\gamma}^{\infty} \frac{1}{N_o} \exp\left(-\frac{\ell}{N_o}\right) d\ell \\
 &= \exp\left(-\frac{\bar{E}_c + N_o}{\bar{E}_c} \ln\left(\frac{\bar{E}_c + N_o}{N_o}\right)\right)
 \end{aligned} \tag{5.69}$$

And the total probability of correlator error is again computed as the average total error.

$$P_{CE} = \frac{1}{2}[1 - P_{CD} + P_{CF}] \tag{5.70}$$

Constraints on the Correlation Detector for Near Optimality

Returning to the expressions for the performance of the optimum detector, it is relatively easy to determine under what conditions the correlation detector behaves near optimum.

Since the sum of the Eigenvalues must equal the signal energy in the received signal (Property 2, Appendix D), if any one Eigenvalue approaches that value, then the remaining Eigenvalues are necessarily small. Thus, as a single Eigenvalue tends to dominate, the threshold given in equation 5.33 approaches the threshold associated with that Eigenvalue alone. Recalling that K is the average signal energy in the received signal,

$$\lim_{\lambda \rightarrow K} \gamma = N_o \ln\left(\frac{K}{N_o} + 1\right) \quad 5.71$$

Also as one Eigenvalue tends to dominate, a single B_i tends to dominate on each hypothesis (equations 5.50 and 5.51) and as a result one of the P_i coefficients (equation 5.48) tends to a value of one while all others tend to zero. Therefore, as all Eigenvalues except one tend to zero, the probabilities of detection and false alarm for the optimum detector reduce to:

$$P_D = \exp\left(-\frac{N_o}{K} \ln\left(\frac{K+N_o}{N_o}\right)\right) \quad 5.72$$

$$P_F = \exp\left(-\frac{K+N_o}{K} \ln\left(\frac{K+N_o}{N_o}\right)\right) \quad 5.73$$

These are seen to be nearly identical to those equations 5.68 and 5.69 which describe the performance of a correlation detector. (For β equal to zero, they are identical.)

Additionally, and possibly most importantly, as β becomes small, λ_1 tends to dominate, and the optimum receiver structure tends to that of the correlation detector.

Figure 5.6, which is a plot of the largest normalized Eigenvalue of A, reveals that for $\beta \lesssim 1$ the correlation detector is nearly identically the optimum structure.

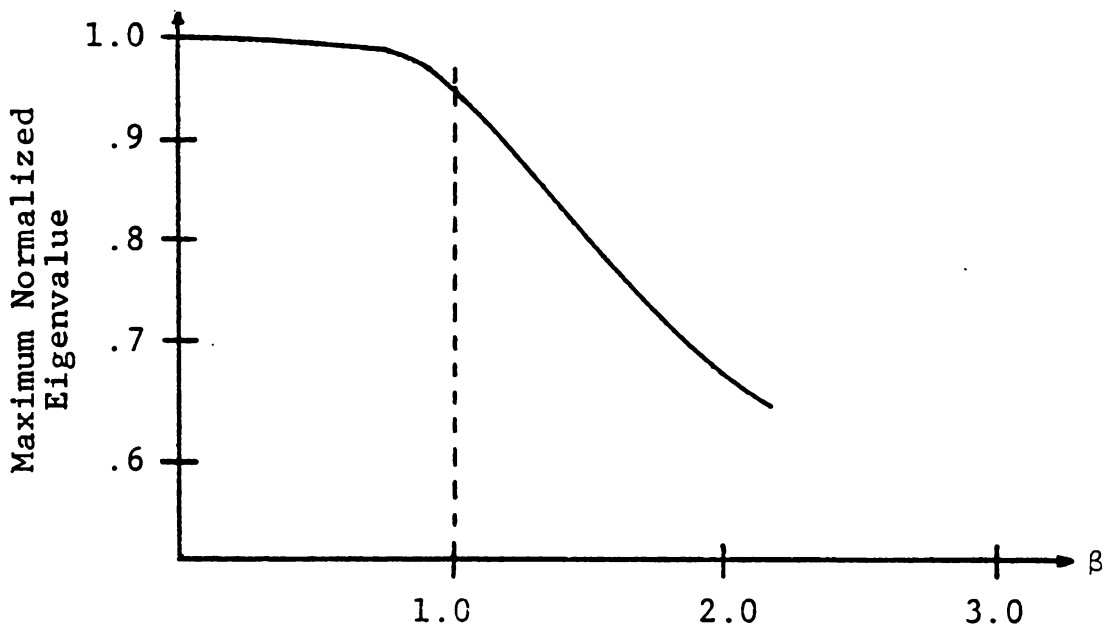


Figure 5.6 Maximum Normalized Eigenvalue of A

Thus, for the correlation receiver performance to approximate that of the optimum receiver, it is sufficient but not necessary that the signal duration be less than or equal to the correlation time of the scattering process.

For true correlation this is the transit time. A nice interpretation of this result will be given in the next section.

The determination of the necessary condition is somewhat subjective and is partially based on the effect that transit time has on the resolving capability of the instrument. As previously discussed, a correlation detector is capable of resolving non-fluctuating targets separated in Doppler by approximately the inverse of the signal duration. As a result, the Doppler resolution could be improved without bound by increasing the effective signal duration. This is not the case when fluctuating targets are involved, as in the case of blood flow measurement, and has been a major misconception on the part of several researchers working the ultrasonic blood flow measurement problem.

In the absence of noise, the signal received from the target portion of the vessel may be written to emphasize the modulation effect of finite transit time.

$$\tilde{r}(t) = \tilde{a}(t)\tilde{f}(t) \quad 5.74$$

The output of the integrator section of a correlation detector mismatched in Doppler by $2\pi f$ radians is simply the Fourier transform of the product of $\tilde{a}(t)$ and the squared envelope of the transmitted signal.

$$\begin{aligned}\tilde{r} &= \int \tilde{a}(t) |\tilde{f}(t)|^2 e^{j2\pi ft} dt \\ &= F\{\tilde{a}(t) \cdot |\tilde{f}(t)|^2\}\end{aligned}\tag{5.75}$$

Which in turn is the convolution of the Fourier transforms of $\tilde{a}(t)$ and $|\tilde{f}(t)|^2$.

$$\tilde{r} = F\{\tilde{a}(t)\} * F\{|\tilde{f}(t)|^2\}\tag{5.76}$$

The squared magnitude of the Fourier transform of $|\tilde{f}(t)|^2$ is just the correlation receiver response to a Doppler mismatched non-fluctuating point target and has an effective width of the inverse of the signal duration. Thus the effect of the time modulation $\tilde{a}(t)$ is to spread the correlation detector response and thereby spoil the resolution of the instrument. Some feeling for the average spreading can be obtained by recalling that the power spectrum of $\tilde{a}(t)$ is the Fourier transform of its autocorrelation function, which in this case is $\Lambda(\beta \frac{\lambda}{T})$.

$$\begin{aligned}S_{\tilde{a}}(f) &= |F\{\Lambda(\beta \frac{\lambda}{T})\}|^2 \\ &= \left[\frac{T}{\beta} \cdot \text{sinc}^2\left(\frac{Tf}{\beta}\right) \right]^2\end{aligned}\tag{5.77}$$

As indicated by this equation, the power spectrum of $\tilde{a}(t)$ has its first zero at f equal the inverse of the red blood cell transit time. Thus for transit times less than the signal duration the resolution is limited primarily by the transit time and not by the signal duration. Similarly, when the transit time is greater than the signal duration, the Doppler resolution is determined by the signal duration.

Thus the fundamental effect of finite transit time is to modulate the reflected signal which, in the frequency domain, has the effect of spreading the Doppler frequency spectrum. By limiting the signal duration to the transit time of the red blood cells, the Doppler spectrum has been confined to the central spike of the ambiguity function for a correlation receiver. In fact, any effect which spreads the Doppler spectrum more than the resolution of the instrument will cause the correlation detector to be non-optimum. In addition to transit time, another effect which could cause this undesirable spreading is the non-uniformity of blood velocity across the target. One of the system constraints imposed in the next chapter will specifically address this issue.

There are at least two good justifications for transmitting shortest possible signal without degrading the instrument's resolution. The first can be extrapolated from Figure 5.5 and equations 5.68, 5.69, and 5.70. That is, for a

constant energy transmitted signal, the performance of the correlation detector decreases as the ratio of signal duration to transit time increases. The second reason is that the shorter the time duration of the transmitted signal, the better the instrument will follow the time varying Doppler associated with arterial flow. Additionally, since the Doppler resolution of the correlation detector is limited to the inverse of the correlation time of the scattering process, there are no apparent justifications for transmitting a fixed energy signal whose duration exceeds the transit time.

Based on these reasons and the sufficiency already established, a reasonable requirement for optimality of the correlation receiver in the presence of transit time effects is that the signal duration be less than or equal to the effective correlation time of the target.

Resolving Capability of Both True and Conventional Correlation Receivers

In this final section of the chapter, the effect of finite transit time on the resolution of true and conventional correlation receivers is investigated. This treatment provides a nice physical interpretation of many of the principles discussed thus far and is relatively intuitive in nature.

The discussion begins by postulating a conventional correlation receiver perfectly matched to the velocity of particles in the target. Figure 5.7 shows a schematic representation of the ultrasonic beam intersecting a target in the blood vessel. It will be assumed that the velocity is constant across the target so that the target appears as a random distribution of particles moving with velocity \bar{v} . Note: This assumption is particularly valid at the center of the vessel where the gradient of the velocity profile is the smallest. As before, each particle is considered a nonfluctuating point scatterer whose scattering properties are statistically independent of all other particles.

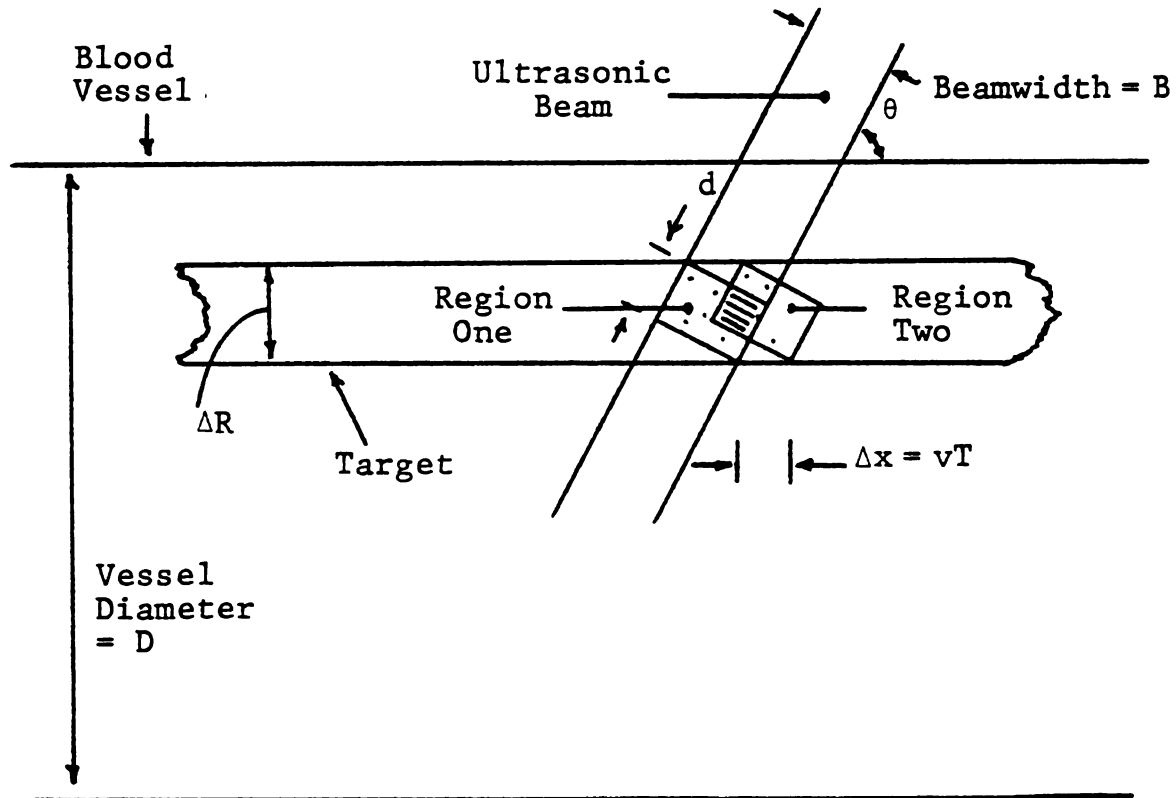


Figure 5.7 Conventional Correlation Receiver Operation

As shown in the figure, targets within region one contribute to the correlator output at time t_1 . All other particles do not contribute because they are either outside the beam or their range does not correspond to delays which lie under the central spike of the ambiguity function.

Each particle in this region Doppler shifts the carrier of the transmitted signal and returns a portion of its energy to the receiving transducer. As long as a particle can remain in this region returning energy on a carrier which is shifted by the appropriate Doppler frequency, it will continue to increase the energy at the output of the correlator. Clearly this cannot continue indefinitely since, in order to appropriately Doppler shift the carrier, the particle must be traveling with a constant radial velocity toward or away from the receive transducer. Thus it will necessarily move out of the spatial region of receiver sensitivity. The maximum time a particle could spend in the region would be less than or equal to d (the range extent of the region of receiver sensitivity) divided by the radial velocity of the particle. Assuming the delay resolution to be the inverse of the signal bandwidth and converting to spatial resolution, an expression for this time, T_{\max} , can be derived.

$$T_{\max} \leq \frac{d}{v_r} = \frac{\Delta\tau \cdot c}{2v_r} = \frac{c}{2v_r \cdot BW} \quad 5.78$$

or

$$T_{\max} \cdot BW \leq \frac{c}{2v_r}$$

This is just the Doppler criteria derived in equation G.4. Thus another way to interpret the Doppler criteria is as follows: point targets can contribute to the output of a perfectly matched conventional correlation receiver for the entire duration of the signal if, and only if, the Doppler criteria is satisfied.

At time $t_2 = t_1 + \tau$ the particles initially in region one would have traveled to region two. However, only those particles in the shaded region remain within the region of receiver sensitivity. Since the particles are independent scatterers, the value of the correlation function of the scattering process is just the ratio of the volume of the shaded region to the volume of region one. This is easily shown by the following simple derivation. The average number of particles in region one is ρv_1 while the average number of particles in the shaded region is ρv_s . Also, the average number of "new" particles in region one at time t_2 is $\rho(v_1 - v_s)$. Then the covariance function of the received signal may be computed as follows:

$$\tilde{K}(t_1, t_2) = E \left\{ \left(\sum_{i=1}^{\rho v_1} \tilde{b}_i \tilde{f}(t_1) \right) \cdot \left(\sum_{j=1}^{\rho v_s} \tilde{b}_j^* \tilde{f}^*(t_2) + \sum_{k=1}^{\rho(v_1 - v_s)} \tilde{b}_k^* \tilde{f}^*(t_2) \right) \right\}$$

Now S

The

simpl

cess

to b

test

Now since

$$E\{\tilde{b}_i \tilde{b}_j^*\} = \begin{cases} 0 & i \neq j \\ 2\sigma_b^2 & i = j \end{cases}$$

Then

$$\begin{aligned} \tilde{K}(t_1, t_2) &= E_t \sum_{i=1}^{\rho v_s} \tilde{f}(t_1) 2\sigma_b^2 \tilde{f}^*(t_2) \\ &= E_t \rho v_s \tilde{f}(t_1) 2\sigma_b^2 \tilde{f}^*(t_2) \\ &= 2\sigma_b^2 \rho v_1 E_t \tilde{f}(t_1) \frac{v_s}{v_1} \tilde{f}^*(t_2) \\ &= 2\sigma_b^2 \rho v_1 E_t \tilde{f}(t_1) \tilde{K}_c(\tau) \tilde{f}^*(t_2) \end{aligned}$$

If a square beam shape is again assumed for mathematical simplicity, the correlation function of the scattering process reduces to a ratio of the areas shown. This is computed to be:

$$\tilde{K}_c(\tau) = \frac{(B-v\tau \sin\theta)(d-v\tau \cos\theta)}{B \cdot d} \quad 5.79$$

This expression can be simplified by expanding and defining two parameters:

$$\tilde{K}_c(\tau) = \begin{cases} 1 - a v \tau - \tau \left[b v - \tau a b v^2 \right] & |\tau| \leq \min \left[\frac{1}{a v}, \frac{1}{b v} \right] \\ 0 & \text{Otherwise} \end{cases} \quad 5.80$$

where

$$a = \frac{\sin \theta}{B}$$

$$b = \frac{\cos \theta}{d}$$

The usage of the parameter a is consistent with previous usage and b is a newly introduced parameter.

Next, the same line of reasoning will lead to a similar expression for the scattering covariance function when a "true" correlation receiver is employed. Remember that true correlation in this development is taken to mean that the received waveform is correlated with a Doppler shifted, time scaled, delayed version of the transmitted signal. In effect, the true correlation receiver tries to follow the target in space by introducing a delay rate in the reference signal. Thus if a true correlation receiver is perfectly matched to a point target, not only is the reference carrier perfectly matched to the target Doppler, but the spatial region of receiver sensitivity travels through space at exactly the same rate as the radial velocity of the target. Clearly, this has the potential of allowing a longer correlated

observation time and therefore, ultimately better velocity resolution.

Referring to Figure 5.8, red blood cells within region one contribute to the correlation output at time t_1 . At time $t_2 = t_1 + \tau$, only those red blood cells in the shaded region remain in the region of sensitivity.

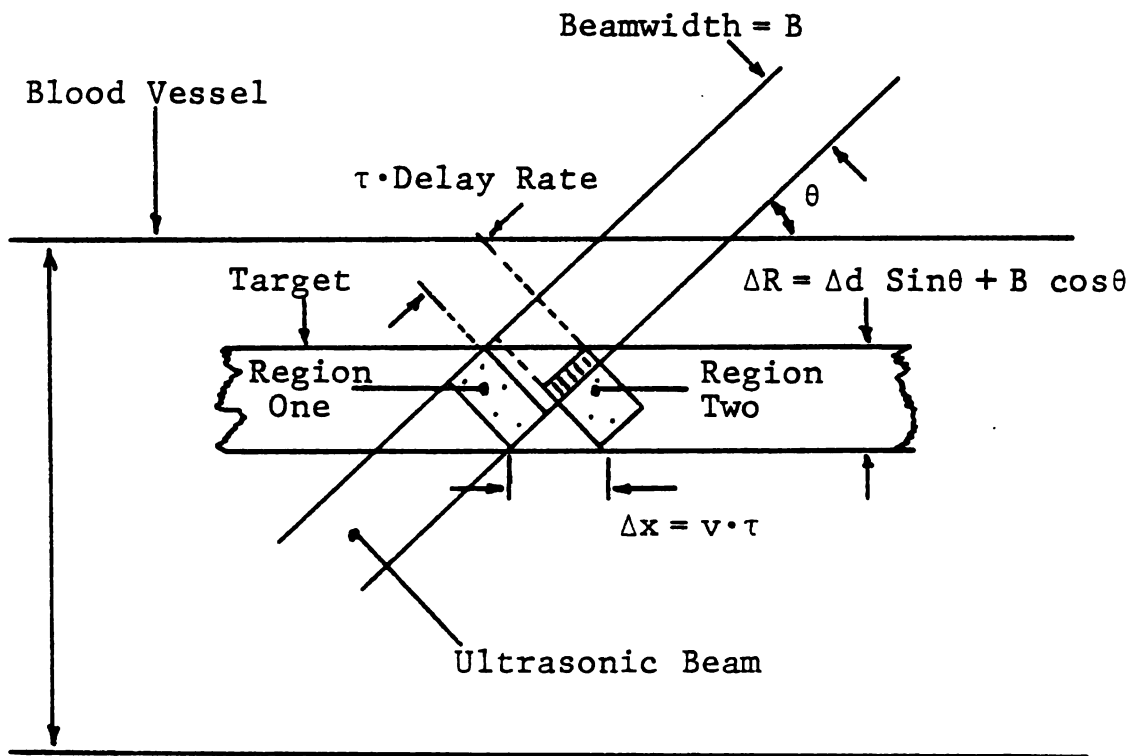


Figure 5.8 True Correlation Receiver Operation

The primary difference between the operation shown in this figure and that shown for the conventional receiver is that the region of sensitivity has maintained the best possible delay match with the original particles.

The covariance function of the scattering process may now be computed in the same manner as it was for the conventional receiver. By taking the ratio of shaded area to the area of region one;

$$\tilde{K}(t_1, t_2) = 2\sigma_b^2 V_l E_t \tilde{f}(t_1) \tilde{K}_T(\tau) \tilde{f}(t_2)$$

$$\begin{aligned} \tilde{K}_T(\tau) &= \frac{d(B - V\tau \sin\theta)}{B \cdot d} \\ &= \begin{cases} 1 - \frac{V \sin\theta}{B} \tau & |\tau| < \frac{B}{\sin\theta} \\ 0 & \text{Otherwise} \end{cases} \end{aligned}$$

$$K_T(\tau) = \Lambda(av\tau) \quad 5.81$$

$$a = \frac{\sin\theta}{B}$$

This is precisely the correlation function derived earlier from the covariance function when range spreading was ignored. In that derivation it was assumed that each scatterer remained at the center of the region of receiver sensitivity and Doppler shifted the carrier. Clearly that assumption is reasonable only if true correlation is employed.

To compare these two forms of processing the effective correlation time for each will be derived. The Doppler resolving capability of each will then be determined as the inverse of the effective correlation time. And finally, the

resolution of the two for a typical selection of design parameters will be plotted as a function of transducer angle θ .

For correlation functions such as those under discussion, a reasonable measure of effective correlation time is:

$$\tau_{\text{eff}} = \int_{-\infty}^{\infty} \tilde{K}(\tau) d\tau$$

For true correlation the computation is nearly trivial:

$$\tau_T = \frac{1}{av} \int_0^{\infty} (1 - av\tau) d\tau$$

$$\tau_T = \frac{1}{av} = \frac{T}{\beta} \quad 5.82$$

This is just the transit time of red blood cells across the beam.

For the conventional receiver the computations are slightly more involved. From equation 5.80

$$\tau_c = \frac{\min[\frac{1}{av}, \frac{1}{bv}]}{2 \int_0^{\min[\frac{1}{av}, \frac{1}{bv}]} 1 - (av+bv)\tau + abV^2\tau^2 d\tau}$$

$$\tau_c = \begin{cases} \frac{1}{av}(1 - \frac{b}{6a}) & a \geq b \\ \frac{1}{bv}(1 - \frac{a}{6b}) & b \geq a \end{cases}$$

This is nearly equal to the transit time of red blood cells through the correlation receiver's region of sensitivity.

Using typical parameters of 2 MHz bandwidth ($d \approx .375$ mm), a beamwidth of 1.0 mm, and a velocity of 50 cm/sec, the plot of Doppler resolution in Figure 5.9 was generated. The potential resolution improvement using true correlation processing over a fairly large range of transducer angles is obvious.

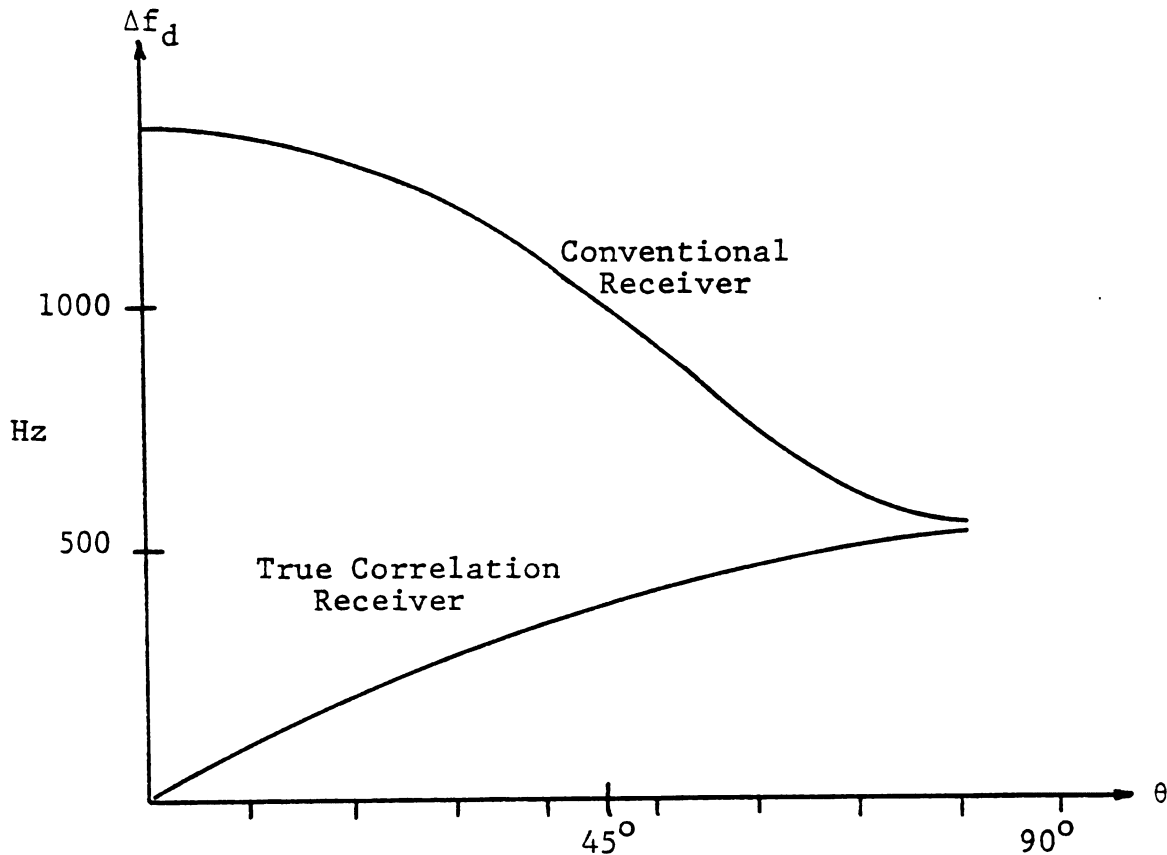


Figure 5.9 Typical Doppler Resolution Plot

It is interesting to note that the theoretical Doppler resolving capability of the true correlation receiver becomes perfect as θ approaches zero. Realistically, of course, this cannot be accomplished. The primary factors working against it are: (1) an infinite integration time is required which is clearly not possible; (2) the red blood cells were assumed to be non-fluctuating when in fact they are actually tumbling; and most importantly, (3) in certain areas of the vessel cross section there can be a significant spread of velocities across the target. However, in the center of the vessel where the effect of transit time is the greatest, the actual spread of velocities is minimum. It is here that true correlation demonstrates the greatest advantage.

In this chapter it was shown that for signal durations less than or equal to the effective correlation time of the scattering process, the performance of a correlation detector is not severely degraded. In fact, under these conditions the correlation receiver is near optimum. If increasing the signal duration beyond the transit time increased the Doppler resolving capability of the instrument, one might consider allowing a slight departure from optimum error performance for the gain in resolution. However, using a true correlation receiver, which provides the best Doppler resolution, the resolving capability of the instrument is limited by the transit time of the red blood cells across the beam. Thus,

there is no advantage in transmitting a constant energy signal whose duration is greater than the transit time.

CHAPTER VI

RESOLUTION CONSTRAINTS AND RECEIVER PERFORMANCE

The work of previous chapters has been concerned with developing a model for the flowing blood and surrounding tissue, and with optimum techniques for detecting blood flow signals. Additionally, certain fundamental limitations were discussed which affect the overall system design of a blood flow imaging instrument. In this chapter these fundamental limitations will be the basis for developing and discussing equations which describe the complex interrelationships between constraints on signal bandwidth, beamwidth, vessel diameter, transducer angle, and spatial and velocity resolution. Also, the error performance of the blood flow imaging system will be evaluated.

Resolution Constraints

Shown in Figure 6.1 is a block diagram of the signal processing section of the blood flow imaging system. As indicated, the signal processor consists of a bank of N correlators, each matched to the same range. However, the Doppler (and the associated time scaling of the envelope) of each correlator in the bank is offset from one another by the inverse of the signal duration. At the end of the correlation

time the output of each correlator is examined by the greatest-of detector which outputs a signal whose magnitude represents the correlator chosen. For example, if the correlator of

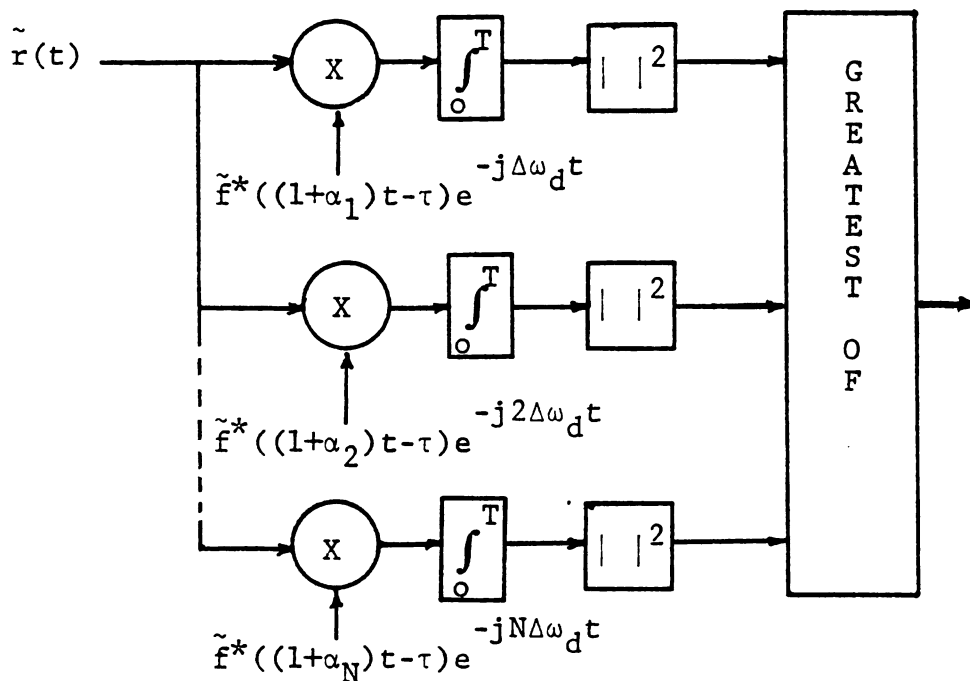


Figure 6.1 System Signal Processor

maximum output were matched to Doppler of $3/T$, then the output of the greatest-of detector might be the binary representation of the digit three. The output of the greatest-of detector is then used to control a visual display. For discussion purposes in this chapter, one might imagine that the controlled variable is the intensity of a CRT spot. (Displays will be discussed in more detail in a later chapter.)

As previously discussed, for laminar time independent flow the signal duration is constrained to be less than or equal to the transit time of the highest velocity red blood cells in the vessel. Since the primary objective of the blood flow imaging system is to estimate blood velocity as accurately as possible, the signal duration should be set at the maximum allowed by this constraint.

$$T = \frac{B}{V_{\max} \sin \theta} \quad 6.1$$

Recalling the direct correspondence between V_{\max} and the maximum Doppler $f_{D_{\max}}$:

$$V_{\max} = \frac{cf_{D_{\max}}}{2f_c \cos \theta} \quad 6.2$$

The Doppler resolution (which is $1/T$) is constrained such that:

$$\Delta f_D \approx \frac{1}{T} = \frac{f_{D_{\max}}}{\frac{2Bf_c}{c \tan \theta}} \quad 6.3$$

As already mentioned, the signal processor consists of N correlators, therefore N levels of brightness. The number of brightness levels is found by dividing the maximum Doppler by the Doppler resolution of the instrument; i.e.,

$$N = \frac{f_{D_{\max}}}{\Delta f_D} \quad 6.4$$

Comparing equation 6.4 with 6.3 it is seen that the number of achievable gray levels for a particular choice of beamwidth, carrier frequency and transducer angle is

$$N = \frac{2Bf_c}{c \tan \theta} \quad 6.5$$

The importance of this result is that the achievable number of gray levels is independent of the velocity of the targets. In fact, N is dependent only on the beamwidth of the transducer (which is usually fixed), the carrier frequency (which is almost always fixed), and the transducer angle with respect to the vessel. This implies that once the conditions under which the instrument will operate are defined, the number of correlators is fixed, simplifying the system design.

If the instrument is expected to operate over some range of transducer angles, then the poorest Doppler resolution (in terms of the number of gray levels) will occur at the maximum angle θ_{\max} .

$$N(\theta_{\max}) = \frac{2 \cdot B \cdot f_c}{c \cdot \tan(\theta_{\max})} \quad 6.6$$

This constraint on the velocity resolution has been imposed by the nature of correlation processing. There is also a constraint imposed by the nature of the target being observed.

For laminar time independent flow, the velocity profile across the diameter of a circular cylindrical vessel was derived in Appendix H.

$$f_D(x) = f_{D_{\max}} \left(1 - \frac{4x^2}{D^2}\right) \quad 6.7$$

Figure 6.2 illustrates how this profile would appear in a longitudinal cut through the vessel center. Also shown in the figure is a typical target located near the vessel wall.

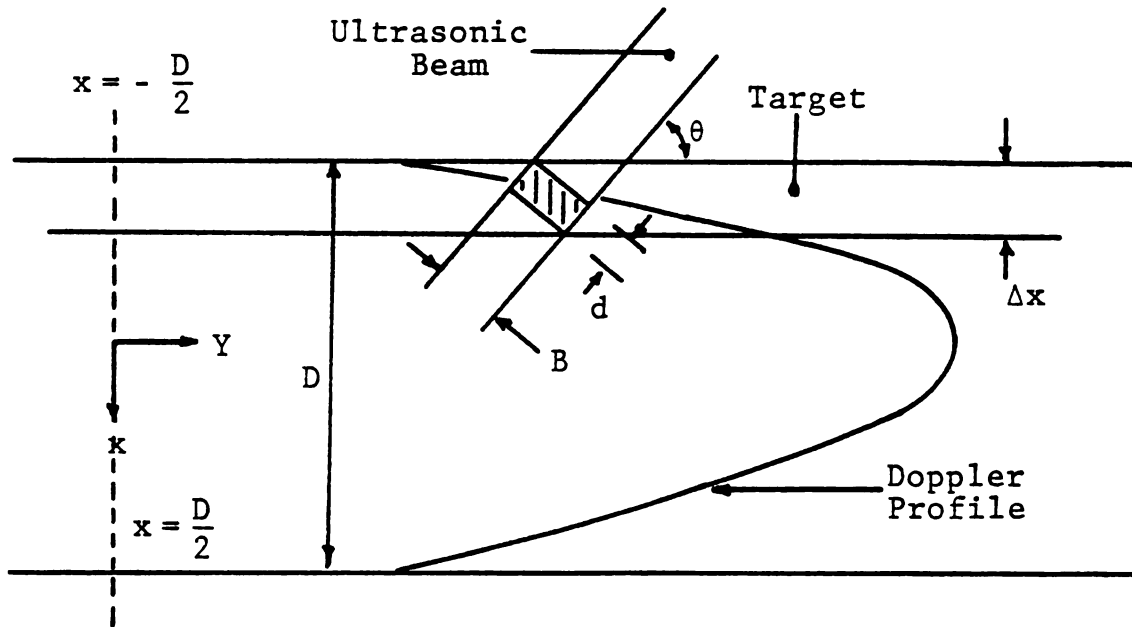


Figure 6.2 Bloodflow Doppler Profile Target Interaction

The width of that target is given by

$$\Delta x = d \sin \theta + B \cos \theta \quad 6.8$$

For reasons discussed in the previous chapter, in order for the individual correlators to operate in an optimum fashion, the actual Doppler spread within the target should be contained within the Doppler resolution of the instrument. As indicated in the figure, the maximum spread of Doppler occurs in the targets located nearest the vessel wall. The Doppler spread across that target may be approximated as:

$$\begin{aligned}\overline{\Delta f_D} &= \left. \frac{\partial f_D}{\partial x} \right|_{(-\frac{D}{2})} \cdot \Delta x \\ &= \frac{4\Delta x f_{D_{\max}}}{D}\end{aligned}\tag{6.9}$$

As was stated previously, the constraint on Δf_D is

$$\overline{\Delta f_D} \leq \Delta f_D \approx \frac{1}{T}\tag{6.10}$$

For this constraint to be satisfied Δx must be small enough that;

$$\Delta x \leq \frac{D}{4T f_{D_{\max}}}\tag{6.11}$$

Defining the ratio of D to Δx as M , and using equation 6.4, the constraint on Δx may be simplified.

$$\Delta x \leq \frac{D}{4N}$$

or;

$$M \geq 4N \quad 6.12$$

This important result states that for optimum design and operation, the number of spatial subdivisions which can be achieved across the vessel, M , must be greater than or equal to four times the number of allowed or desired gray levels.

Using these two apparently simple constraints, the complex interrelationships between all system parameters are determined. Combining the results of equations 6.6 and 6.12, for a system designed to operate as optimally as possible up to some θ_{\max} , the spatial resolution must be sufficient such that for all angles up to θ_{\max} , M is greater than or equal to $4N(\theta_{\max})$.

$$M \Big|_{\theta < \theta_{\max}} \geq 4N(\theta_{\max}) \quad 6.13$$

Recalling the definition of M and using the fact that $d = c/(2 \cdot BW)$, then from equation 6.8

$$M = \frac{D}{\Delta x} = \frac{D}{\frac{c}{2 \cdot BW} \sin \theta + B \cos \theta} \quad 6.14$$

M is clearly a function of θ , which takes on a minimum value for some θ ; call this angle (θ_{worst}). If the inequality of equation 6.13 is satisfied for M evaluated at θ_{worst} , then it is certainly satisfied for all θ less than θ_{\max} .

The value of θ_{worst} is found by taking the derivative of M with respect to θ in equation 6.14, setting equal to zero and solving for θ_{worst} . The result is:

$$\theta_{\text{worst}} = \text{Tan}^{-1} \left(\frac{c}{2 \cdot B \cdot BW} \right) \quad 6.15$$

M evaluated at θ_{worst} is:

$$M \Big|_{\theta=\theta_{\text{worst}}} = \frac{2 \cdot D \cdot BW}{\sqrt{c^2 + (2 \cdot B \cdot BW)^2}} \quad 6.16$$

Substituting this expression for $M(\theta_{\text{worst}})$ and the expression for $N(\theta_{\text{max}})$ in equation 6.13, a convenient inequality constraint on the bandwidth is obtained. After straightforward algebraic manipulations, the desired constraint is obtained.

$$BW \geq \frac{4 \cdot B \cdot f_c \cdot C}{\sqrt{D^2 \text{Tan}^2(\theta_{\text{max}}) - 64 \cdot B^4 f_c^2}} \quad 6.17$$

Equation 6.17 is a constraint on bandwidth as a function of θ_{max} with beamwidth as a parameter. By using the constraint of equation 6.6, a similar constraint on bandwidth as a function of θ_{max} with N as a parameter is obtained. This is accomplished simply by solving equation 6.6 for B and substituting into equation 6.17. The result of this substitution is:

$$BW \geq \frac{2N \cdot C \cdot f_c}{\sqrt{D^2 f_c^2 - 4N^4 C^2 \tan^2(\theta_{\max})}} \quad 6.18$$

Plots of the functions 6.17 and 6.18 are given in Figure 6.3, 6.4, 6.5, and 6.6. These curves are for carrier frequencies of 3 and 5 MHz and vessel diameters of .5 and 1.0 cm.

These plots contain a great deal of information if interpreted properly. Basically, they indicate what choice of parameters results in the optimum use of the instrument's frequency resolving capability. For example, assume that a transducer with a beamwidth of .5 mm is to be employed in a system intended to visualize flow in a vessel 1 cm in diameter using a 5 MHz carrier. Also suppose that three gray levels are sufficient. Then, using the plot of Figure 6.3, the acceptable solution points are seen to be those in the intersection of the regions above the $B = .05$ curve and above the $N = 3$ curve. If minimum bandwidth were the requirement, then the point at the intersection of the two curves would be selected. A one megahertz signal would be utilized and the maximum acceptable transducer angle would be 50 degrees. If minimum bandwidth were not the requirement, then any other point in the intersection region may be used.

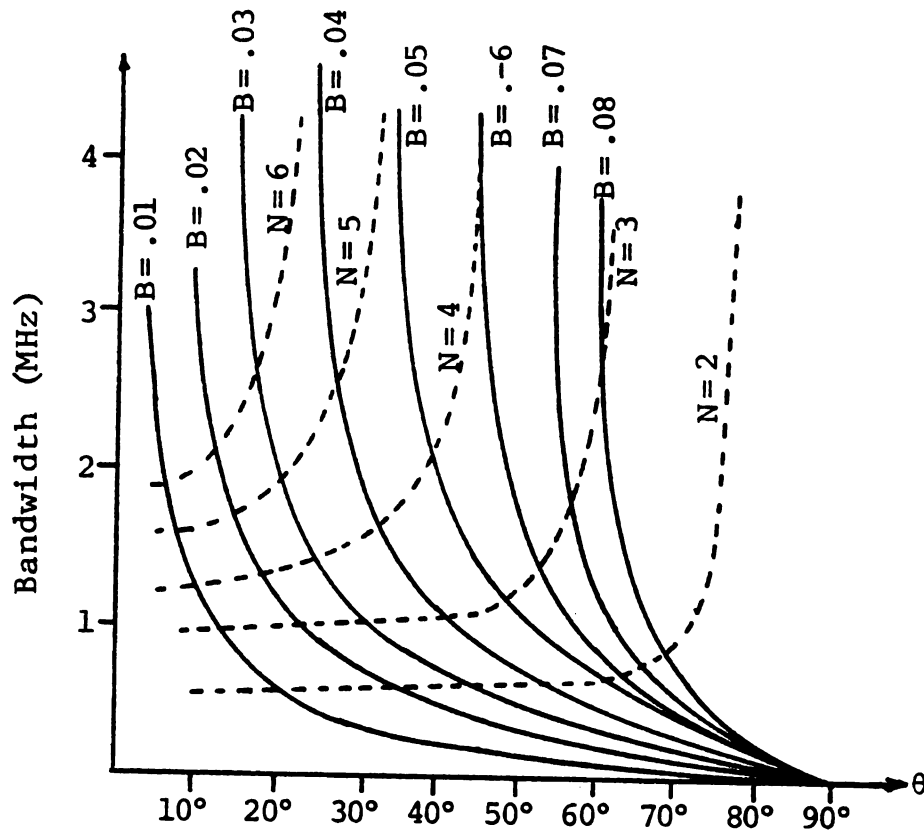


Figure 6.3 Design Curves for $f_c = 5$ MHz, $D = 1$ cm

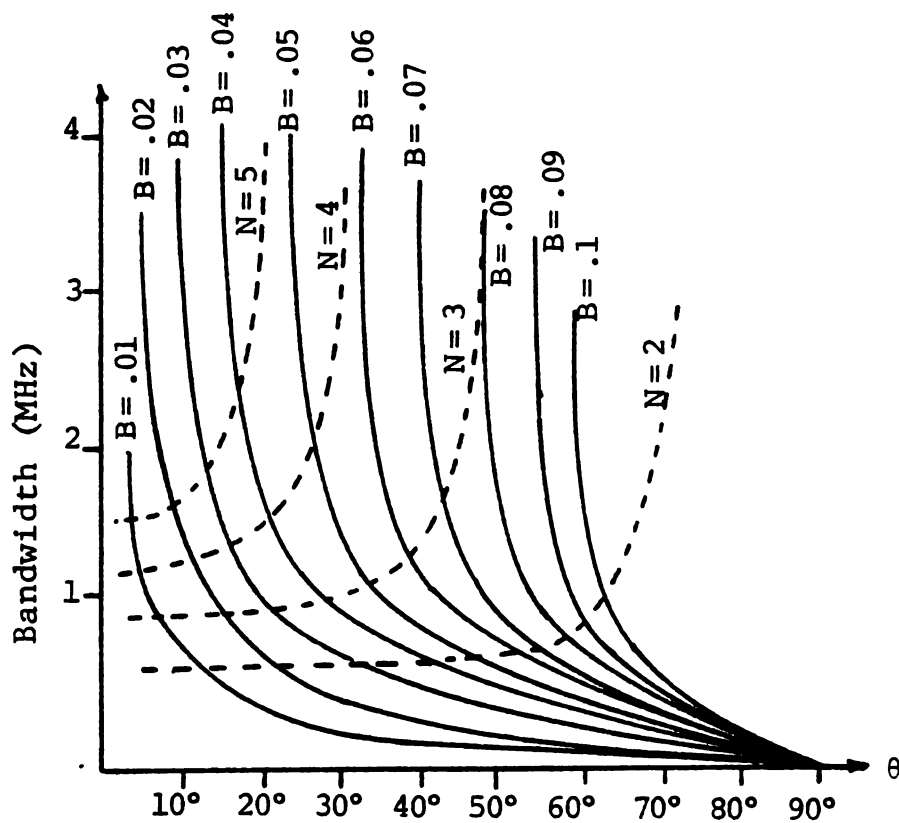


Figure 6.4 Design Curves for $f_c = 3$ MHz, $D = 1$ cm

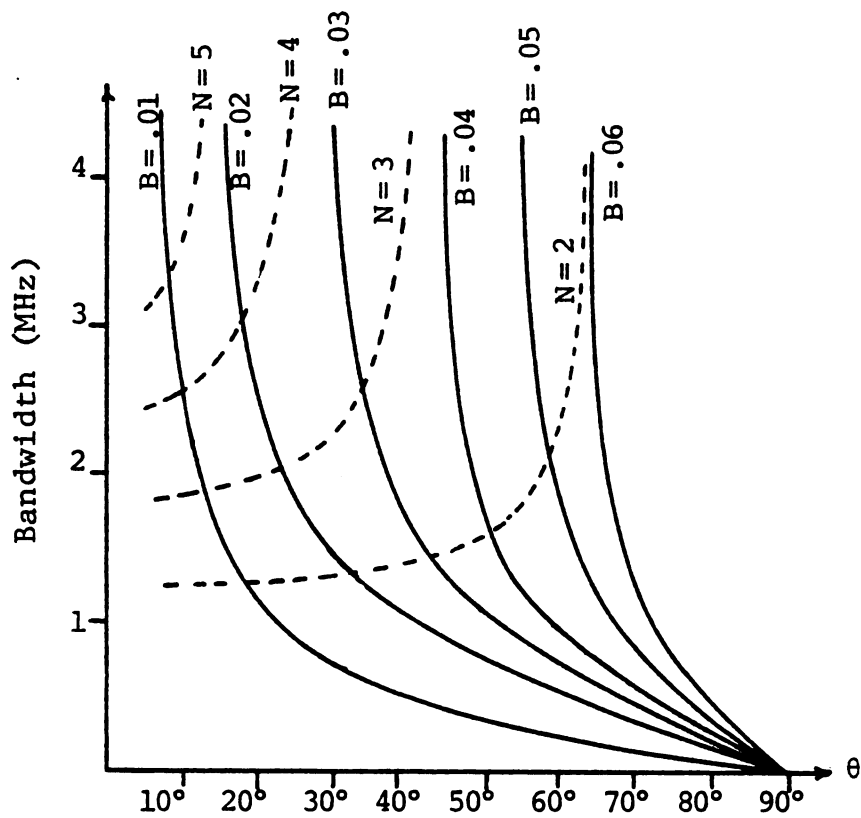


Figure 6.5 Design Curves for $f_c = 5$ MHz, $D = .5$ cm

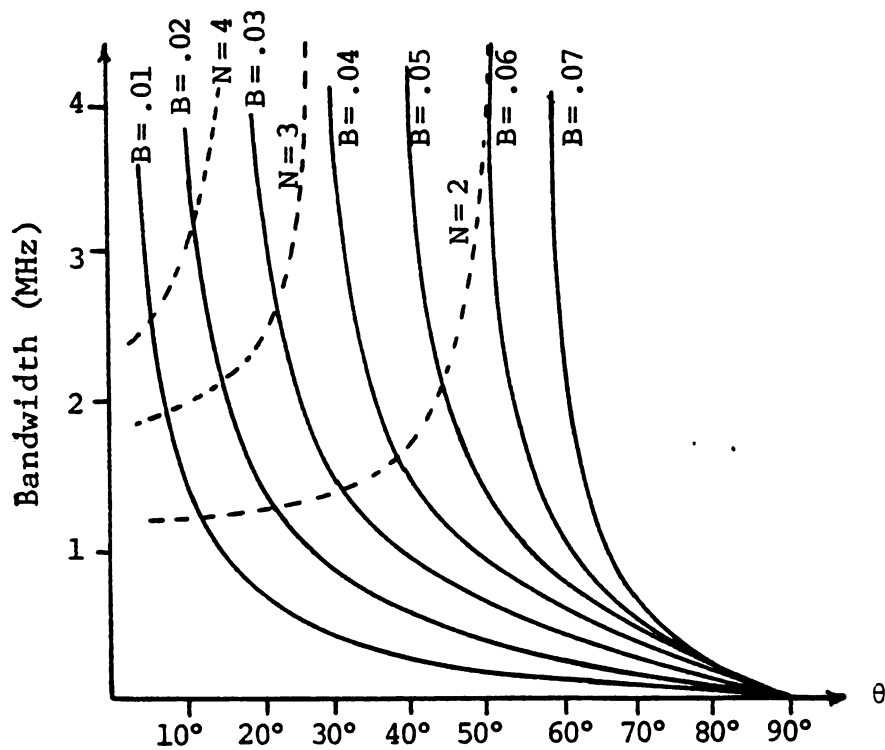


Figure 6.6 Design Curves for $f_c = 3$ MHz, $D = .5$ cm

By carefully studying these plots, raising questions, rereading the derivation and studying them some more, a tremendous intuition about the complex interrelationships involved can be developed. These plots are quite important and quite unique to true correlation processing.

Receiver Performance

In this section the performance of the correlation type estimator shown in Figure 6.1 is evaluated. What follows is important in that it supports the possibility of blood flow imaging using a periodic pulse train as the transmitted signal and it is in keeping with the most important goal of this dissertation; that is to provide insight into the fundamental processes involved and how they affect the performance of a correlation type blood flow measurement system.

Before developing analytical expressions for receiver performance, a short discussion on the sources of error as well as the differences between the function of the flow estimator of Figure 6.1 and the detector described in Chapter Five will be presented.

The correlation detector shown in Figure 5.4 performs the specific task of deciding whether or not a target with the appropriate velocity existed at the specified range during the time of observation. The decision is made by

comparing the correlated energy with a threshold which is determined by the statistics of the scattering process and any additive noise.

The estimator described in this chapter consists of a bank of correlators, each being similar to the correlation detector. However, the final decision criteria is quite different. For the estimator, the decision is to choose the correlator with highest correlated energy output.

In general, there are three sources of correlated energy output for each correlator.

1. Desired Signal Energy
2. Clutter Returns
3. Noise

Since the periodic pulse train described in Chapter Three has been selected as the transmitted signal, clutter returns are negligible. However, at the output of each of the correlators there will be an additive noise component due to receiver noise, transducer noise, etc. If this noise is assumed to be white and Gaussian, and if the reference signals to the individual correlators are orthogonal, then the noise contributions in each correlator are uncorrelated and therefore statistically independent. Actually, the signals to the individual correlators are not completely orthogonal, as is easily shown.

$$\begin{aligned}
\langle \tilde{f}_i, \tilde{f}_j \rangle &= \int_0^T \tilde{f}_i(t) \tilde{f}_j^*(t) e^{-j(\omega_i - \omega_j)t} dt \\
&= \tilde{\phi}(0, \omega_i - \omega_j)
\end{aligned} \tag{6.19}$$

Thus the inner product of $\tilde{f}_i(t)$ and $\tilde{f}_j(t)$ (where $\tilde{f}_i(t)$ and $\tilde{f}_j(t)$ are the reference signals to the i^{th} and j^{th} correlator, respectively) is just the value of the time frequency autocorrelation function evaluated along the Doppler axis at $\omega_i - \omega_j$. As previously discussed, this is small but, in general, not zero. Thus the noise is only approximately uncorrelated.

Assuming one (and, of course, only one) of the correlators is perfectly matched to the target Doppler, and assuming that each of the correlators is equally likely to be matched, the probability of error is given by:

$$P_E = P(\ell_m < \ell_1 \text{ or } \ell_m < \ell_2 \text{ or } \dots \text{ or } \ell_m < \ell_N) \tag{6.20}$$

Alternatively, one could compute the probability of error by subtracting the probability of being correct from one.

$$P_E = 1 - P_c \tag{6.21}$$

The probability of being correct is equal to the probability that ℓ_i is less than ℓ_m for all i not equal to m .

That is:

$$P_c = \int_{\ell_m=0}^{\infty} \int_{\ell_i=0}^{\ell_m} \rho(\ell_m, \ell_1, \dots, \ell_N) d\ell_1 \dots d\ell_N d\ell_m \quad 6.22$$

Because of the near orthogonality of the reference signals to the individual correlators, the correlator outputs are nearly independent. With this assumption, the probability of being correct may be simplified to read:

$$P_c = \int_{\ell_m=0}^{\infty} \rho(\ell_m) \left[\int_{\ell_i=0}^{\ell_m} \rho(\ell_i) d\ell_i \right]^{N-1} d\ell_m \quad 6.23$$

The density functions governing ℓ_m and ℓ_i have already been determined in equations 5.64 and 5.65, respectively. Substituting these expressions into equation 6.26,

$$P_c = \int_{\ell_m=0}^{\infty} \frac{1}{\bar{E}_c + N_o} e^{-\frac{\ell_m}{\bar{E}_c + N_o}} \left[\int_{\ell_i=0}^{\ell_m} \frac{1}{N_o} e^{-\frac{\ell_i}{N_o}} d\ell_i \right]^{N-1} d\ell_m \quad 6.24$$

After carrying out the integration in brackets this expression reduces to:

$$P_c = \int_{\ell_m=0}^{\infty} \frac{1}{\bar{E}_c + N_o} e^{-\frac{\ell_m}{\bar{E}_c + N_o}} \left[1 - e^{-\frac{\ell_m}{N_o}} \right]^{N-1} d\ell_m \quad 6.25$$

Applying the binomial expansion theorem, this expression may be put in an integrable form.

$$P_c = \int_{\ell_m=0}^{\infty} \frac{1}{\bar{E}_c + N_o} e^{-\frac{\ell_m}{\bar{E}_c + N_o}} \sum_{i=0}^{N-1} \binom{N-1}{i} (-1)^i e^{\frac{-i\ell_m}{N_o}} d\ell_m \quad 6.26$$

After grouping terms and carrying out the necessary integration, a rather simple expression for the probability of correct decision results.

$$P_c = \sum_{i=0}^{N-1} \binom{N-1}{i} (-1)^i \frac{1}{1 + i(1 + \frac{\bar{E}_c}{K} \text{SNR})} \quad 6.27$$

$$\text{SNR} = \frac{K}{N_o}$$

The probability of error is simply $1 - P_c$ and equals:

$$P_E = - \sum_{i=1}^{N-1} \binom{N-1}{i} (-1)^i \frac{1}{1 + i(1 + \frac{\bar{E}_c}{K} \text{SNR})} \quad 6.28$$

Using a value of .8 for $\frac{\bar{E}_c}{K}$, the probability of error curves were generated for various values of N and are plotted in Figure 6.7. These curves show the theoretical performance of a properly designed imaging system. Returns observed in the lab using a conventional pulsed Doppler flowmeter indicate realistic signal-to-noise ratios in the range 10 to 20 db. Although the expected error rates associated with these signal-to-noise ratios do support the reasonableness

of blood flow imaging using the periodic pulse train, they also demonstrate the importance of designing the correlation receiver to operate near optimum.

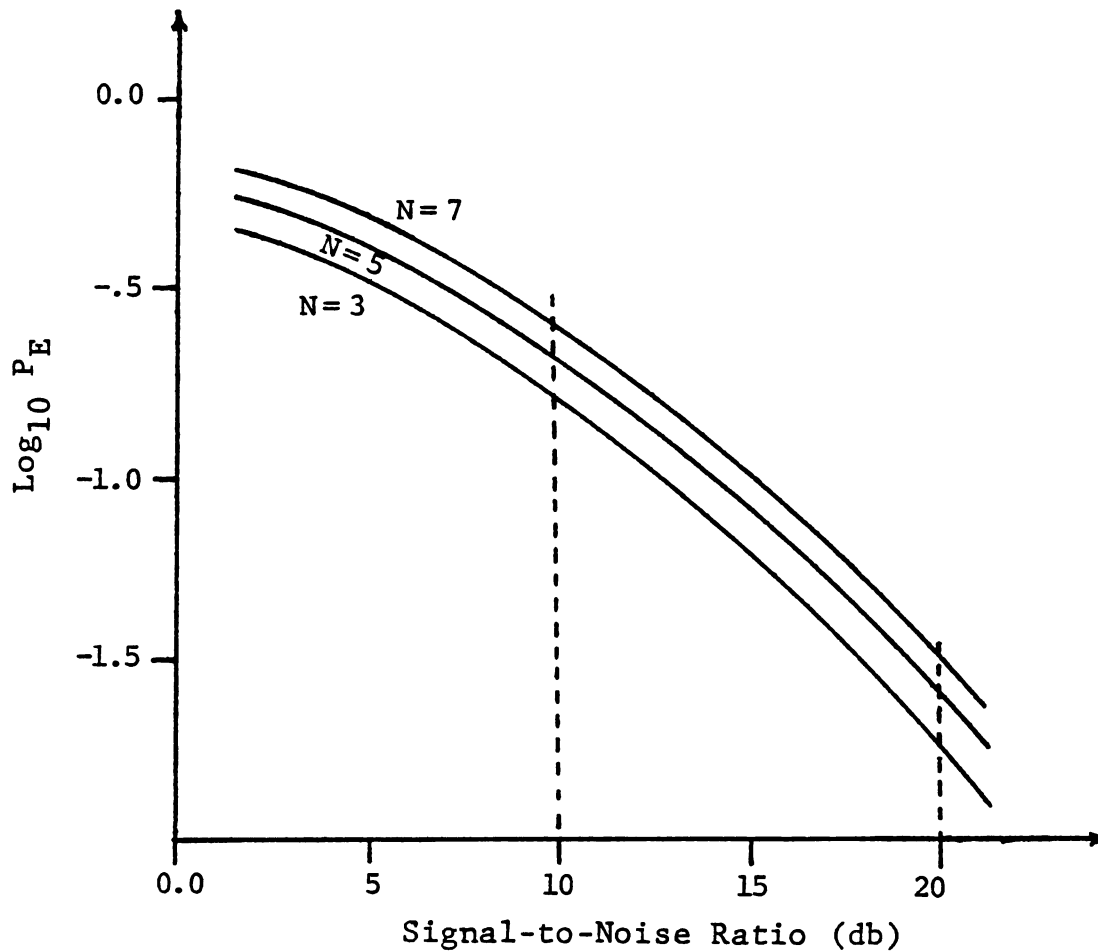


Figure 6.7 Probability of Error Curves

CHAPTER VII

TRANSDUCER CONSIDERATIONS

The work of previous chapters has focused primarily on defining and interrelating many signal and receiver processing requirements which must be met in order to obtain near optimum performance from the correlation receiver. In Chapter Six some very useful design curves were presented which, if applied intelligently, will guide the system designer through the maze of trade-offs while maintaining an optimum design. However, in all these discussions it has been assumed that an efficient method of coupling acoustic energy into and out of the body exists. Furthermore, there have been no restrictions placed on the bandwidth capabilities of these transduction devices or on the minimum achievable beamwidth. This chapter addresses these issues.

The system element which performs the electrical-to-acoustical and acoustical-to-electrical conversion is the transducer. Several different mechanisms have been discovered which are capable of performing this task. They include the moving coil transducer, the electrostatic transducer, the variable reluctance transducer, the magnetostrictive transducer, and the piezoelectric transducer. Of all these only

the piezoelectric transducer is commonly used in medical ultrasonics. There are many reasons for this, the most important being the fact that piezoelectric transducers exhibit excellent electromechanical properties. Specifically, they exhibit very high coupling coefficients which are a measure of the efficiency with which the transduction is carried out. A high coupling coefficient means that the transmitting efficiency is high, the receiving sensitivity is high, and that the transducer can operate over a wide frequency band.⁴⁰

A basic piezoelectric transducer is made by sandwiching a layer of material between two very thin conducting plates as shown in Figure 7.1.

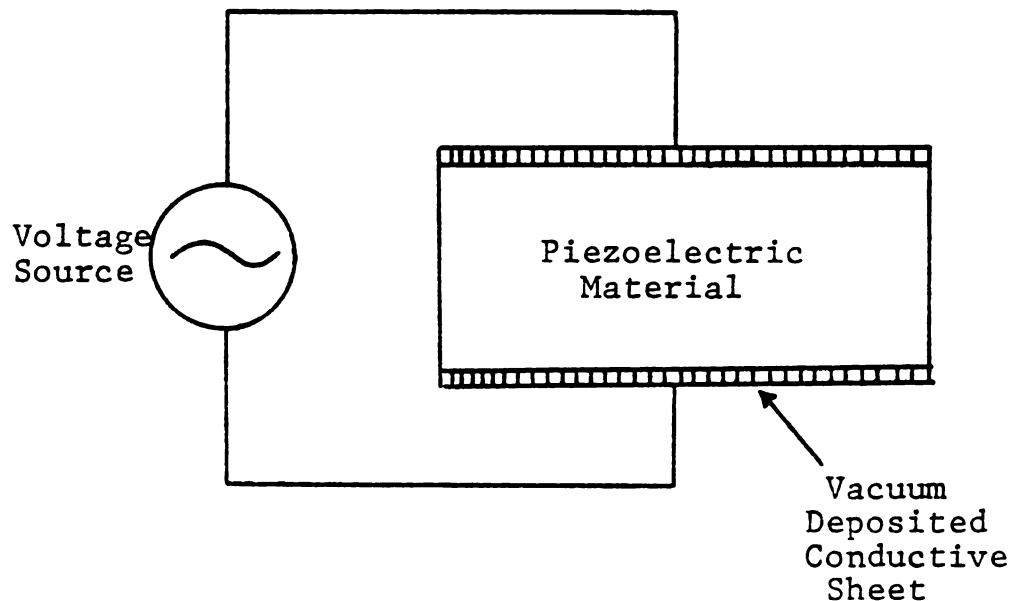


Figure 7.1 Basic Piezoelectric Transducer

If the material is piezoelectric, then applying a voltage to the plates causes the material to deform. Similarly, a pressure applied to the plates will cause the material to deform which in turn generates an electric potential difference across those plates. True piezoelectric materials occur naturally and, if cut properly, can perform satisfactorily in medical ultrasonics. (Quartz is an example of one such material.) However, much better properties have been found in synthetic piezoelectric materials. These materials are formed by heating certain ceramics above their Curie temperature. At these temperatures molecular bonds are broken and the molecular dipoles are free to align with an applied electric field. The material is then allowed to cool in the presence of that electric field. When the temperature drops below the Curie temperature, these dipoles are essentially "frozen" in position and a permanent electric field remains. Lead zirconate - lead titanate (PZT) is currently the most commonly used material in medical ultrasound and has a coupling coefficient of approximately .62.

In the construction of a complete transducer package these sandwich arrangements are epoxied to an absorbing backing material and a quarter wave matching layer is generally cemented to the exposed face. (See Appendix H for a discussion of quarter wave matching.) The purpose of the backing is to mass load the transducer and thereby spoil its Q.

Transducers have been made with Q's as low as about 1.6. At 5 MHz this corresponds to a maximum one-sided bandwidth capability in the neighborhood of 1.50 MHz, or a pulse width of approximately 0.7 μ s. Other transducer parameters of interest include the maximum allowable input power, efficiency, and beamwidth.

The efficiency of three commercial transducers was measured in the lab by reflecting a short burst of ultrasound from a thick steel plate at close range. The transducers were assumed to have the specified input impedance of 50 ohms so that the input and output power could be computed from the input and output peak voltages, respectively. The transducer efficiency was then calculated by solving the following equation.

$$\begin{aligned}
 P_{\text{out}} &= [P_{\text{received}}] \times [\text{Conversion Efficiency}] \\
 &= [P_{\text{in}} \times \text{Conversion Efficiency}] \\
 &\quad \times [\text{Conversion Efficiency}]
 \end{aligned}$$

This equation assumes equal transduction efficiencies for transmitting and receiving. The computed conversion efficiency of two of these transducers was on the order of 15%. The third transducer was determined inoperative.

Although maximum power capability of a piezoelectric transducer is an important parameter in some applications, for blood flow measurement systems a much more important question concerns the range of safe power levels. Unfortunately, not enough information is available at this time to determine an absolute safe power limit. However, it can be said that average input powers in the 250 to 750 milliwatt range have been used routinely.³

An appreciation for the constraints on beamwidth can be developed by observing the typical beam pattern shown in Figure 7.2.⁴²

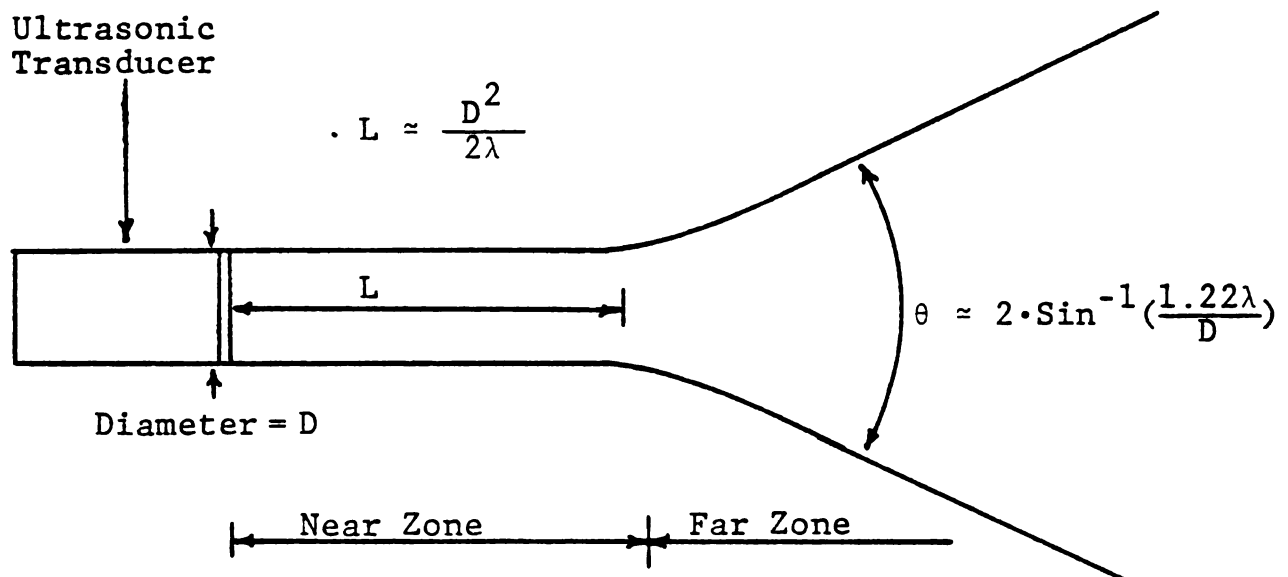


Figure 7.2 Typical Beam Profile

As shown in the figure, the so-called near field conditions exist up to a distance of approximately $D^2/2\lambda$ where D is the transducer diameter and λ is the wavelength of the carrier. While in the near field, the beamwidth remains approximately constant. It also should be noted that the intensity of energy in this zone varies tremendously as a function of spatial location. Also, the fact that required beamwidths are on the order of one millimeter presents a difficult problem. Figure 7.2 indicates that in order to achieve a one millimeter beamwidth, the transducer diameter would need to be approximately one millimeter. At five megahertz the near zone would end after about one millimeter. Furthermore, the angle of beam divergence would be over 20° . This is clearly unacceptable.

To overcome this fundamental limitation several techniques have been employed. To analyze these techniques, all of the concepts of geometric optics may be applied, including Snell's law of refraction. The method most widely employed is to focus the ultrasonic beam. In medical ultrasonics a focusing lens is concave rather than convex as it would be in the more familiar optical systems. This is because the speed of sound in lens materials is greater than in water or tissue. Generally a plano-concave lens is ground in polystyrene and cemented to the exposed face of the transducer.³ Figure 7.3 summarizes the constraints on the resulting focal region.⁴³

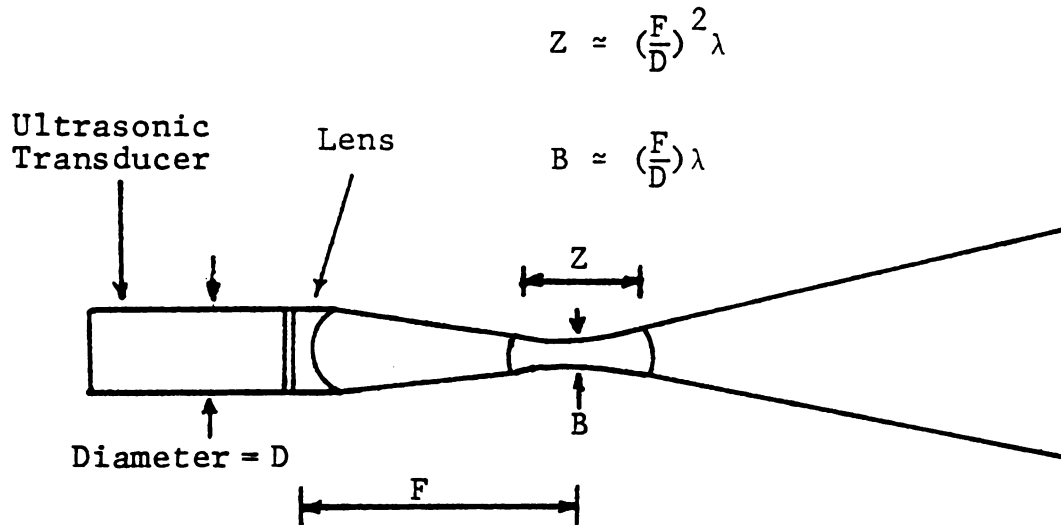


Figure 7.3 A Focused Beam Profile

Using typical numbers for the focal length F (~ 2.5 cm), the wave length λ (~ 0.03 cm), and the diameter of the transducer D (~ 1 cm), the length of the focal zone is easily computed to be approximately two millimeters, and the beam diameter is approximately .75 millimeters.

These appear to be acceptable numbers for mapping the lumen of smaller vessels. Unfortunately, they are only marginally acceptable for observing larger vessels.

As this example demonstrates, it is difficult to produce the narrow, elongated focal zone required for blood flow imaging using conventional focused transducers. Two attempts at solving this problem are discussed next. The first method

is one developed and evaluated as part of this research effort, the dual element transducer. The other method is a more traditional array technique.

The dual element transducer proposed by Jethwa is composed of a central disk and an outside annular ring, as shown in Figure 7.4.

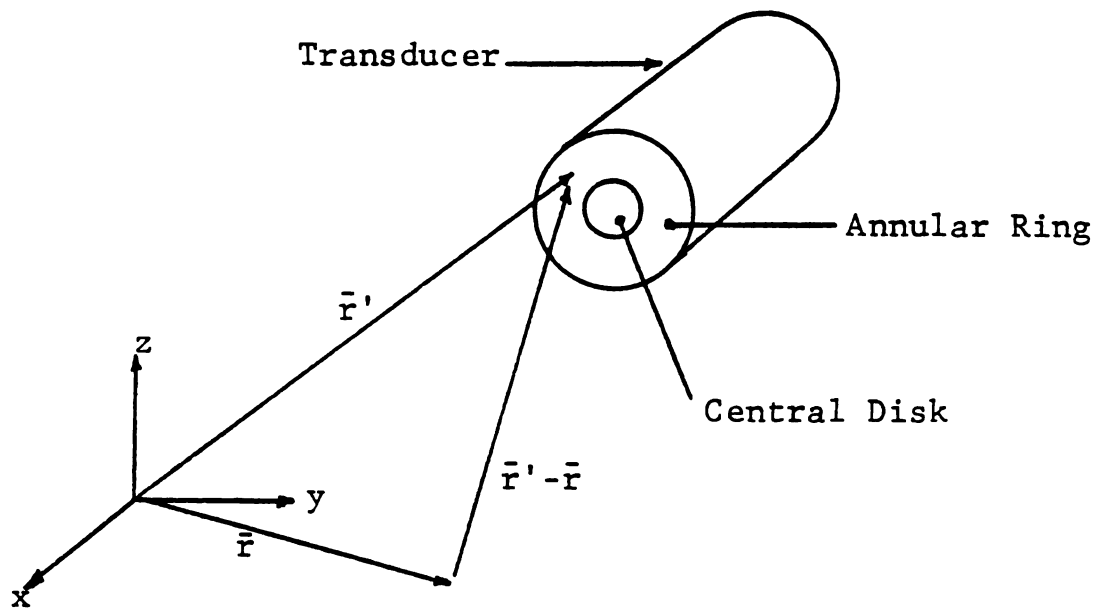


Figure 7.4 Dual Element Transducer

Using the geometry shown in the figure and assuming a uniform velocity distribution across the outside annular ring, the spatial response of the transducer can be derived. To do this, consider each $dx' dz'$ area located at \bar{r}' on the transducer face, as an individual transducer. Each of these elemental transducers will act as a point source and project

sound uniformly in all forward directions. At the spatial location \bar{r} , the velocity wave will be sinusoidal with a delay of $\frac{|\bar{r}-\bar{r}'|}{c}$ (see equation H5). Additionally, the intensity of the wave will have decreased by a factor of $(\sqrt{2\pi}|\bar{r}-\bar{r}'|)^{-2}$. Therefore, the instantaneous displacement of the material supporting the acoustic wave will be of the form:

$$d\xi(\bar{r}, \bar{r}', t) = \frac{\xi_{\max}}{\sqrt{2\pi}|\bar{r}-\bar{r}'|} e^{j\omega(t - \frac{|\bar{r}-\bar{r}'|}{c})} dV'$$

Assuming the material to be linear, the total displacement will be the sum of all displacements caused by all elemental transducers across the annular ring. That is:

$$\xi(\bar{r}, t) = \int_{\substack{\text{transducer} \\ \text{face}}} \frac{\xi_{\max}}{\sqrt{2\pi}|\bar{r}-\bar{r}'|} e^{j\left[\omega\left(t - \frac{|\bar{r}-\bar{r}'|}{c}\right)\right]} dV'$$

7.1

Using equation H13 it is quickly verified that the intensity of the wave at \bar{r} is simply

$$I(\bar{r}) = \frac{\omega^2 \xi_{\max}^2 \rho_0 V}{2} \left| \int \frac{1}{|\bar{r}-\bar{r}'|} e^{-\frac{2\pi|\bar{r}-\bar{r}'|}{\lambda}} dx' dy' \right|^2 \quad 7.2$$

Two dual element transducers were built to operate at 5 MHz. One with an outside diameter of 1.0 centimeter and a central disk of diameter .635 centimeters. For the other these dimensions were approximately doubled. Using a digital computer, the theoretical beam pattern for the annular ring of the smaller transducer was computed. A portion of the pattern is plotted in Figure 7.5.

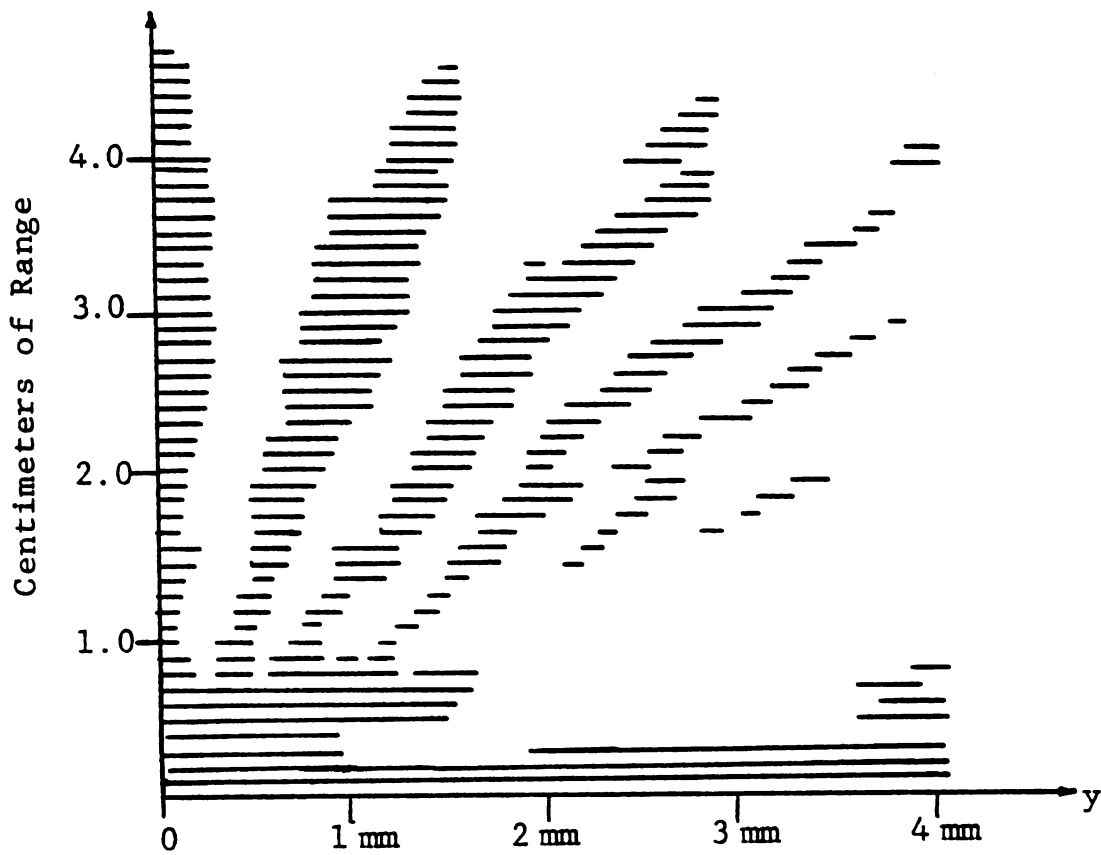


Figure 7.5 Annular Ring Beam Pattern

In this figure the darker shaded regions are regions where power levels exceed half the maximum power in the

cer

hal

and

is

nee

ere

of

two

bea

the

enc

typ

ele

arr

central focal zone. As indicated, the focal zone (defined as half power points) begins at approximately 1.75 centimeters and extends to near five centimeters. The width of this zone is approximately .75 millimeters. This would appear to be nearly an ideal beam pattern for blood flow imaging. However, there are several high energy sidelobes in the vicinity of the main lobe and separated by angles on the order of only two degrees. If these lobes are taken collectively as the beam, then at the desired range of two to three centimeters the beamwidth is nearly six millimeters. Laboratory experience has shown the dual element transducer and the focused type to provide about the same level of performance.

The second method of beam forming uses an array of N elements usually spaced by a distance of $\lambda/2$. A typical arrangement is shown in Figure 7.6.⁴⁴

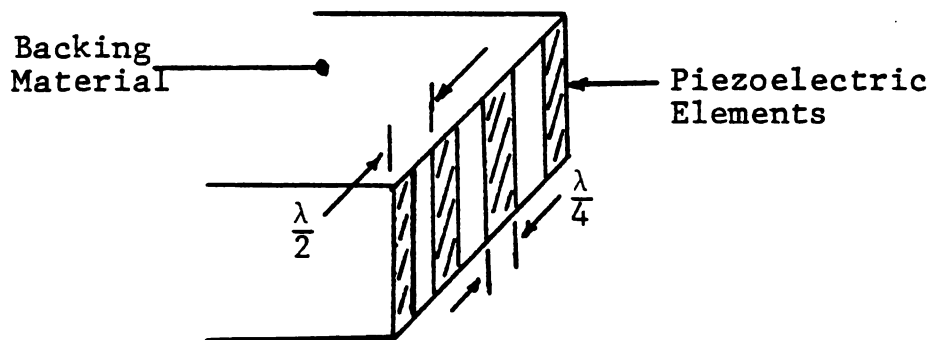


Figure 7.6 Typical Transducer Array

The procedure for computing the beam pattern is identical to that which was employed for computing the beam pattern of the dual element transducer. A generalized beam pattern for such an array is shown in Figure 7.7.

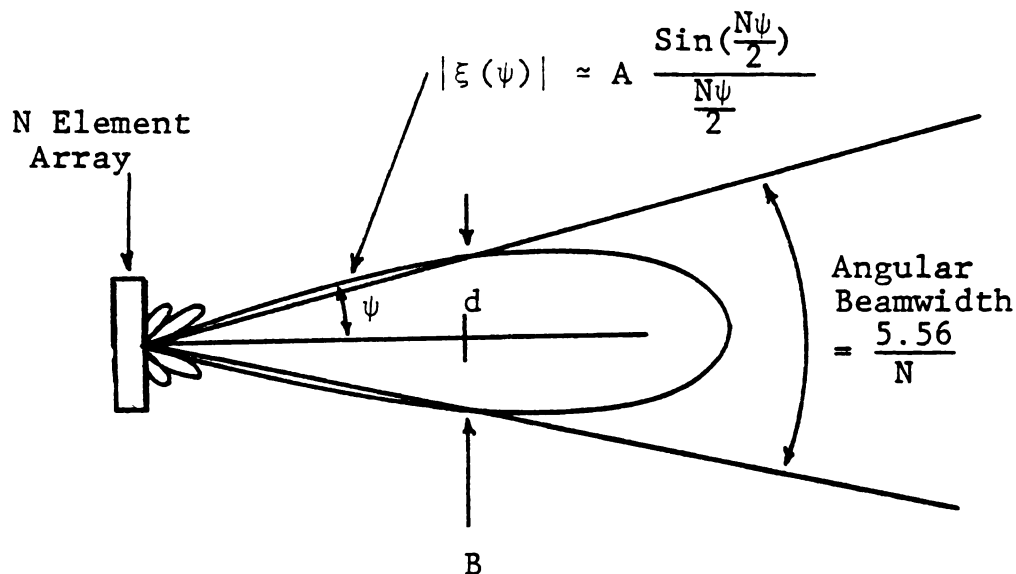


Figure 7.7 Generalized Array Beam Pattern

An important feature of this array pattern is its half power angular beamwidth, which is inversely related to the number of elements and is given approximately as:

$$\text{Angular beamwidth} \approx \frac{5.56}{N} \text{ radians}$$

7.3

The width of the beam, B , at a distance, d , is related to the angular beamwidth by

$$\text{Angular beamwidth} \approx 2 \cdot \tan^{-1} \left(\frac{B/2}{d} \right) \quad 7.4$$

At distances and beamwidths required for visualizing blood flow, the arctangent is approximately its argument. With this approximation an approximate expression for the required number of elements can be derived.

$$N \approx 5.56 \frac{d}{B}$$

Thus for an actual beamwidth of one millimeter at 2.5 centimeters, the required number of elements is approximately one hundred forty. At 5 MHz this would correspond to a transducer width of approximately two centimeters.

Array type transducers are currently being utilized in ultrasonic imaging.⁴¹ Their greatest advantage may be that by properly phasing the elements the beam can be steered in space. This would be of particular interest for application in a flow imaging system intended to display two-dimensional images.

CHAPTER VIII

SYSTEM IMPLEMENTATION

The analysis thus far has been conducted in the sterile environment of the complex signal domain. For the most part, implementation details have not been considered and certainly the requirements and benefits of a particular operating scenario have been ignored. In this chapter these real world factors and their effects are discussed with regard to system implementation and operation.

First, consider a likely operating scenario. Since the ultimate goal for the blood flow imaging system is to aid in the detection of cardiovascular disease, it will most likely be used by a physician in a clinical setting, much the way X-ray machines and ultrasonic tissue visualization systems are currently employed. The fact that a human operator is in the system loop can be used to great advantage if the operator is supplied with the proper displays and controls. For example, in the system previously described all the processing depended upon the maximum velocity of blood in the vessel, which is itself one of the major unknowns. Without knowledge of the maximum Doppler, there is no apparent way to determine the required signal duration. For instance,

suppose the signal duration is too long ($f_{d_{\max}}$ assumed too small). Then, as targets in the center of the vessel are observed, none of the correlators in the bank will be matched and the output will be a random variable governed by a nearly uniform probability distribution. This may give the false impression that turbulence exists in the vessel. By making the maximum Doppler an operator controlled input, the physician could adjust the maximum Doppler accordingly, and thereby indirectly determine the correct signal duration.

Another major system design question concerns the number of correlators to be used in the correlation bank. The design curves in Figures 6.3 to 6.6 suggest a combination of parameters which guarantee the optimality of the matched correlator over the entire vessel. By carefully examining those curves, one quickly realizes that if this type of optimality is desired, then only a very crude image might be displayed. For example, suppose the design constraints were to indicate that only two correlators should be implemented. Then there will be excellent estimation of the Doppler associated with those regions of the vessel where the target perfectly matches one of the two correlators. However, for that rather substantial region remaining, the output will jitter between these two states. The nearer the target Doppler is to one of the correlators, the higher the probability of the output being in that state. Figure 8.1 illustrates this effect across the diameter of a typical vessel for a two correlator system.

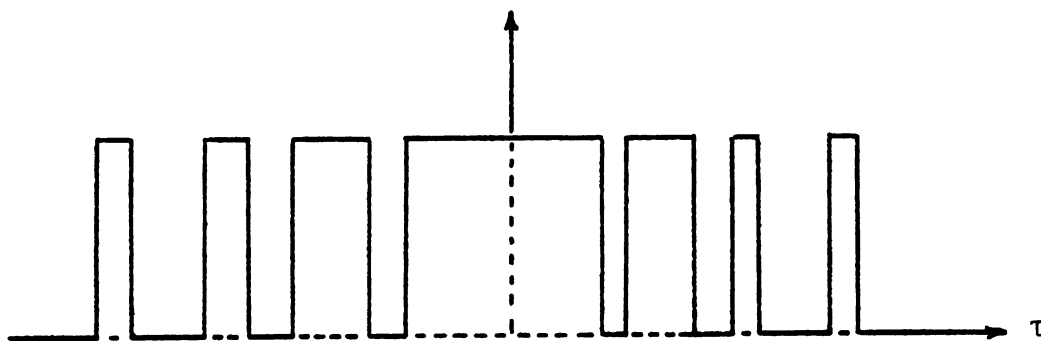


Figure 8.1 Expected Output of a Two Correlator System

Clearly this display is difficult to interpret. One method of solving the display problem would be to introduce more than two correlators into the bank while leaving the signal duration unchanged. Increasing the number of correlators to four would require that the frequency spacing between them be halved. Figure 8.2 demonstrates the effect this would have on the output.

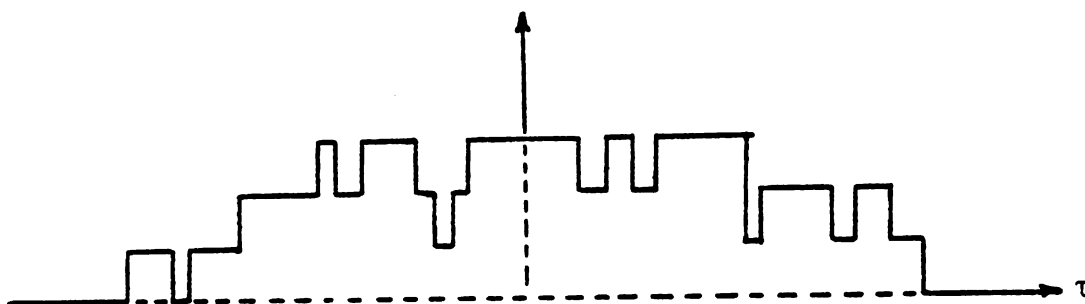


Figure 8.2 Effect of Doubling the Number of Correlators

This is obviously a much more "usable" display. The system Doppler resolution remains as before. However, it is easier for the observer to "see" the average value in Figure 8.2 than in 8.1. (They are the same.) In general, if the value read from the design curves indicates a resolution of N_1 gray levels and N_2 gray levels are desired, then the frequency of successive correlators in the bank should be separated by

$$\Delta f = \frac{1}{N_2} \cdot \left(\frac{N_1}{T} \right) = \frac{f_{d \max}}{N_2} \quad 8.1$$

It is important to realize that although the actual number of gray levels has been increased for display purposes, the system's global Doppler resolution remains the same. Again, the interpretive ability of the human operator has been exploited.

Another potential difficulty in using the instrument is locating the desired vessel. It could be difficult for an operator to locate a vessel by observing the visual display alone. This difficulty results from the fact that if the flowmeter is attempting to image flow in stationary tissue, none of the correlators match the target and the display is totally random, rather than dark as desired.

One potential solution might be to require the output of the selected correlator to be above some threshold level. Unfortunately, the value in this solution is at best questionable. The difficulty results from the fact that the average energy out of any mismatched correlator, due to returns from tissue, is greater than the average energy at the output of a correlator matched to a portion of the flowing blood. This can be seen by recalling that the average pedestal height of the ambiguity function, associated with a periodic pulse train, is the inverse of the number of pulses transmitted (typically .01 to .1). However, the scattering cross section of tissue is on the order of one hundred times the scattering cross section of blood. Therefore, if the proposed threshold were set high enough to darken the display in tissue, it would also be set high enough to darken the display when desirable targets are present.

One workable solution which could be implemented would be to process the received signal by two methods. One method would be the blood flow imaging system. The other would be a conventional pulsed Doppler flowmeter designed to provide an audible output. In this way the operator could "hear" when a vessel has been located.

The most fundamentally important components of the system **are** the correlators in the correlation bank. A canonical form

for each of the correlators was given in Chapter Five, Figure 5.4. Figure D.8 of Appendix D showed how this correlator would be implemented using real operations, and is repeated here for convenience.

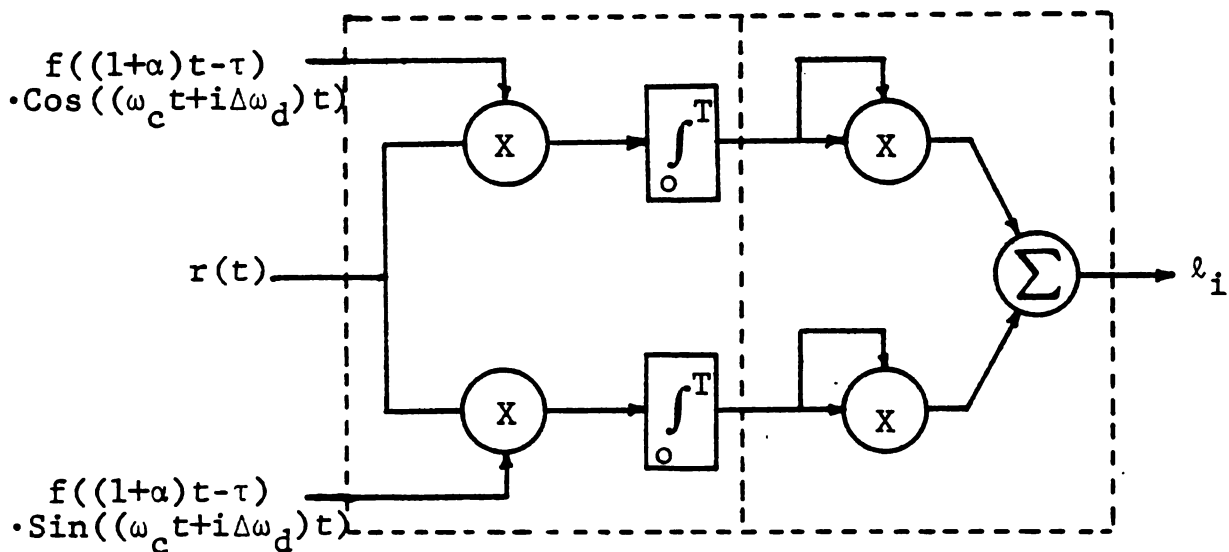


Figure 8.3 Bandpass Correlator

As seen in the figure, the real world operations are slightly more involved than their complex counterpart. Also, the figure indicates that quadrature pairs of the reference signals are required. This necessarily adds some measure of complexity to the reference signal generation unit. Additionally, the integrators must have the capability of being reset to zero (dumped).

To help the reader gain some appreciation for the difficulties involved in designing a blood flow imaging instrument, a typical design example is presented which is based on the design of a proposed system.

Suppose that it is desired to image flow in vessels 1.0 cm in diameter at a range of 2.5 cm. The first design question concerns the choice of carrier frequency. For reasons discussed in Chapter Three, five megahertz is selected.

The next parameters to be determined are the transducer focal zone and diameter. Clearly the transducer should have a focal length of 2.5 cm. After iterating through the design curves of Figure 6.5 and the transducer constraints of Figure 7.3, a transducer diameter of one centimeter was selected. The focal width for this transducer is approximately .75 mm, while the focal zone length is a very poor 2 mm. (The reader is strongly encouraged to actually carry out this iterative procedure.)

The lowest Q transducers available are capable of transmitting a .66 μ s pulse of 5 megahertz carrier. This corresponds to a one sided bandwidth of 1.5 megahertz. From the design curves of Figure 6.5 this system is capable of providing resolution in the 2.8 gray level area. This implies a signal duration of approximately $2.8 f_{d_{\max}}$, and is usable up

to angles of approximately 60° before performance is degraded. Even though the gray level resolution is only 2.8 gray levels, the frequency separation of the correlators will be chosen as $f_{d_{\max}}/5$. The reasons for this are strictly for display purposes as previously discussed.

Figure 8.4 shows the basic block diagram of a true correlation blood flow imaging system.

The overall system operation will be described by examining the individual blocks and observing how they interrelate to form an integrated operational system. The primary responsibility of the central controller is to provide the necessary timing to all other subfunctions. The operator inputs to the central controller through the control display unit are: the minimum range to be observed, the maximum range to be observed, and the maximum expected Doppler to be encountered. The central controller then sets the transmitted signal duration and correlator integration time at

$$T = \frac{2.8}{f_{d_{\max}}} \quad 8.2$$

Also, the oscillator bank is set up to provide quadrature pairs of carriers at $5 \text{ MHz} + n \cdot \Delta f_d$, where $n = 1, 2, \dots, 5$ and $\Delta f_d = f_{d_{\max}}/5$.

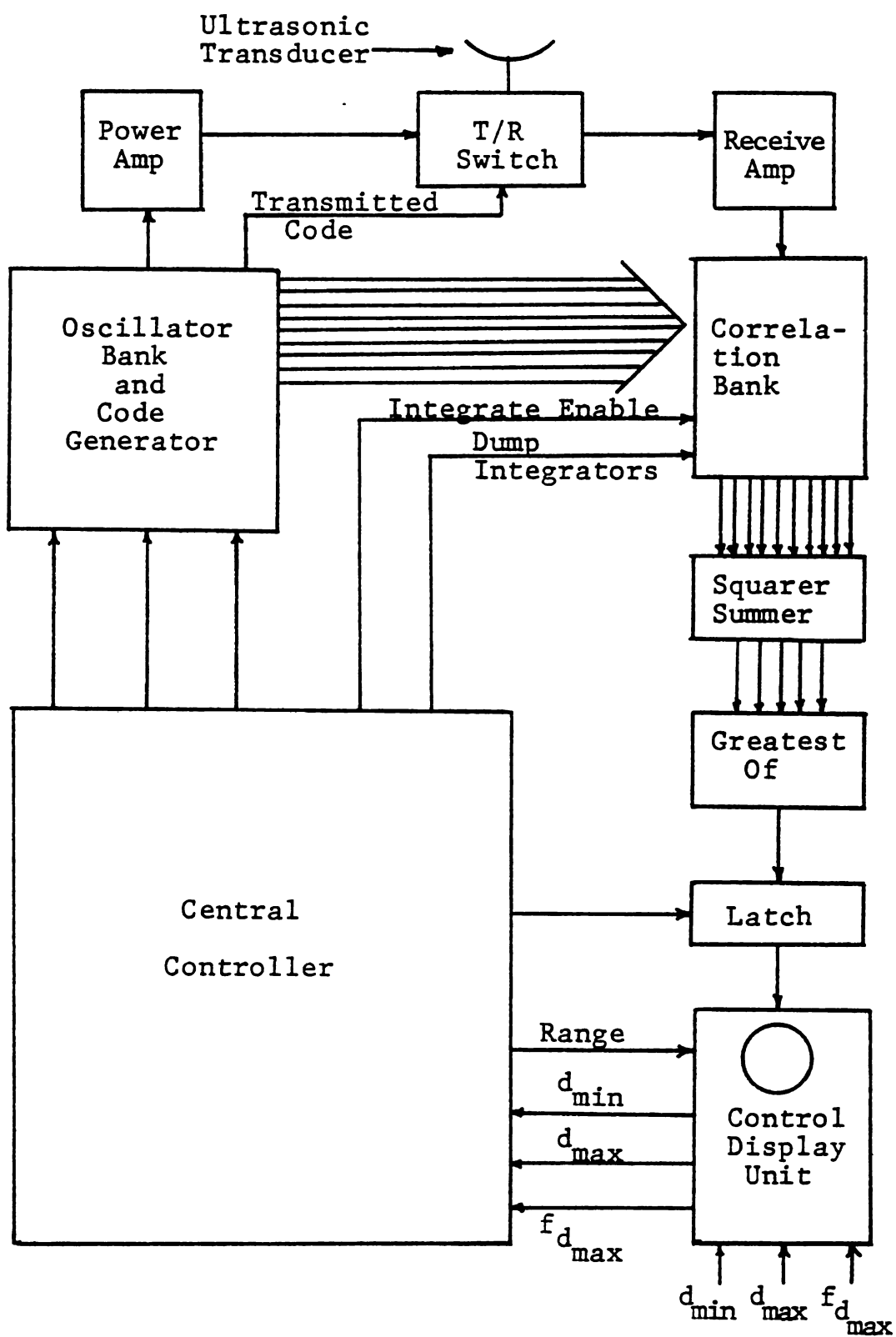


Figure 8.4 Blood Flow Imaging System

At
mitted
the f
mitte
deri
coun
mul
nic
res
vi
pu
am
bo
an
st
di
tr

obs
all
int
tra.
+ n
ner
Deri
this

At time, $t = 0$, the central controller resets the transmitted code phase to zero. The five megahertz carrier from the five megahertz oscillator is pulse modulated by the transmitter pulse generator. The PRF of the pulse generator is derived from the five megahertz clock through a divide by 500 counter. The output of the divider triggers a monostable multivibrator which is set to produce a pulse of width .66 microseconds. Resetting the code phase to zero amounts to resetting the counter. Taken as a whole, the operations provide a train of carrier burst each of .66 μ s duration at a pulse repetition frequency of ten kilohertz. This signal is amplified by the power amplifier and transmitted into the body by the transmitting transducer. Additionally, the transmitted code is used to control the Transmit/Receive (T/R) switch. This switch isolates the receiver from the transducer during transmission and isolates the transmitter from the transducer otherwise.

At a delay corresponding to the minimum range to be observed, the central controller resets the code phase of all the reference pulse generators to zero and zeros all ten integrators in the correlation bank. The reference pulse trains are derived from separate oscillators running at 5 MHz $+ n \cdot \Delta f_d$, $n = 1, 2, \dots, 5$. This is accomplished in the same manner as for the transmitted pulse train, by dividing by 500. Deriving the pulse trains from their associated carriers in this manner automatically time scales the complex envelope

so that true correlation is being performed. These five quadrature pairs of pulse modulated carriers are fed to the five individual correlators in the correlation bank. Each correlator is composed of two mixers and two integrators as shown in Figure 8.3. In the correlation bank these reference signals are correlated with an amplified version of the received signal.

During the entire correlation interval the integrator outputs are being squared and quadrature components combined in the squarer/summer to produce five outputs which are measures of the correlated energy at each Doppler. Also, the "greatest of" detector is continually comparing these outputs and providing a binary representation corresponding to the correlator of maximum output.

T seconds after the integrators are dumped, the buffer latch at the output of the "greatest of" detector receives a latch pulse from the central controller. At that time the current output of the "greatest of" detector is stored by the latch for use by the control display unit. Also at that time, the transmit code phase is reset to zero and the cycle is repeated except that delay is incremented to correspond to the next target in space. Incrementing through range continues until the maximum range to be observed is reached and the entire cycle is repeated.

A typical control display unit might consist of a CRT type display which converts the digital range and Doppler information to analog voltages which are used to control the electron beam. If the range information deflects the beam vertically and the Doppler information deflects the beam horizontally, a conventional flow profile is generated. By using Doppler to intensity modulate the beam, this system could be extended to display two-dimensional images of vessel cross section.

CHAPTER IX

SUMMARY AND CONCLUSIONS

In this final brief chapter, the material presented in this dissertation is reviewed and some final comments are made concerning it. Additionally, some comments are included on ultrasonic blood velocity measurements in general, its problems and its potential directions.

To review the material presented, first consider the goal. It was stated in the introduction that the true goal of this dissertation was to convey as much information as possible about what was learned concerning the fundamental nature of processes which affect the design and performance of correlation type blood flow measurement systems. Generally speaking, this knowledge was obtained as support to the parallel effort of constructing a practical system. Since that time, when the initial idea of using random noise failed, there have been many failures, each generating new ideas, asking more questions, and demanding more answers. As a result, the body of knowledge surrounding blood flow measurement has grown. This dissertation basically presented that information in the order and environment that it was first learned.

After an initial brief history on the events which led to the beginnings of this research, the investigation began by examining those physical attributes of the human body which are important for gaining an overall perspective as well as those specific details which directly affect modeling decisions and other assumptions. At this point the flow of thought begins to leave the real world and enters the world of approximations and mathematical characterizations. Based on physical descriptions, the flowing blood is characterized by the way it acts on an artificial complex signal. To do this it was necessary to define a target. That target definition was in turn based on the stated measurement objectives and the nature of correlation processing. Finally, a characterization emerged as the covariance function of the scattering process. Also, based on the available information, a model for the surrounding tissue was developed at the end of Chapter Three. This model was called the Relative Doppler/Range scattering function.

In Chapter Four the tissue model was utilized to evaluate the performance of a variety of potential signals in the presence of clutter. The signals investigated were representative of those signals actually implemented in the laboratory system. It seems ironic that for all the analytical effort, the simple periodic pulse train was selected as the most reasonable choice. Virtually all other candidate signals were eliminated because of the tremendous energy in the clutter returns.

In Chapter Five, the conditions which must be met to insure the optimality of correlation processing were discussed. Transit time effects were studied by deriving a receiver which is optimum for detecting this fluctuating target. The structure and performance of that receiver was compared with the correlation detector. Finally, it was determined that for signal durations less than the correlation time of the scattering process, the correlation receiver is optimum. For true correlation processing this is just the transit time of red blood cells across the beam. This result is significant in another regard as well. It finally puts to rest any claims that the Doppler resolving capability of a correlation type blood flow measurement system can be improved without bound by increasing the effective signal duration.

Also included was a unique approach to comparing the true correlation and the conventional correlation receiver. It was shown that true correlation processing may provide substantial resolution improvement over the current conventional systems. This is a rather significant finding. However, its significance may be small when compared to the significance of the results of Chapter Six.

In the last half of Chapter Six the error probabilities for the theoretical blood flow imaging system are determined. Under typical conditions of signal and noise power the error

rates certainly support the feasibility of the flow imaging system. However, in the first half of that chapter some extremely important and enlightening resolution constraint curves were generated. The importance of these curves cannot be over-emphasized. The implications of these results will be discussed shortly.

Chapter Seven examined some of the current capabilities of ultrasonic transducers. In particular, the fundamental limitations of using focused transducers were indicated and two techniques which attempt to overcome those limitations were discussed.

Finally, in Chapter Eight these ideas were combined and used to carry out a very typical design example patterned after an actual hardware system design. An interesting technique for making the visual display more acceptable to the human operator was suggested. However, it must be emphasized again that the actual resolving capability of the instrument remains as indicated by the design curves of Chapter Six.

The design example chosen was selected to visualize flow in a one centimeter vessel. Even in this case two very real problems were encountered. One concerned the design of a focused transducer capable of having a narrow focal zone extending over the entire vessel. The other problem concerned

the resolving capability of the instrument. By attempting to reach a reasonable trade-off between resolution, beamwidth, bandwidth and maximum usable angle, the designer soon discovers that an instrument of somewhat poor resolving capability must be accepted.

At first it might appear that the transducer requirements are more realizable in small vessels. This is not true. In order to maintain the same Doppler resolving capability, the beamwidth must be made correspondingly smaller. This is accomplished by increasing the diameter of the transducer or bringing the focal zone nearer. Both of these have the effect of shortening the focal zone to the point where it no longer extends across the vessel diameter.

Some or all of the difficulties associated with using focused transducers may be eliminated by using array related techniques. However, a much larger problem remains. That is improving the instrument's velocity resolving capabilities. Again it might appear that the answer lies in good transducer design. By studying the design curves of Chapter Six, it is quickly verified that better resolution can be achieved by using narrower and narrower beams. This also is a two edged sword. By reducing the beamwidth to improve Doppler resolution, the maximum usable angle has decreased. In fact, all

that is accomplished by reducing the beamwidth is to shift the burden of partitioning the vessel into sufficiently small targets from the signal processing to the transducer. Certainly at zero angle this partitioning is determined entirely by the beamwidth. Additionally, the minimum attainable beamwidth is directly related to the wavelength of the carrier and, as discussed in an earlier chapter, there are practical limits on transmitted carrier frequency.

As stated in the Introduction and earlier in this chapter, the major goal of this dissertation has been to convey as much information as possible about what was learned concerning the fundamental nature of processes which affect the design and performance of correlation type blood flow measurement systems. Using the knowledge gained in pursuit of this goal, a conclusion may be drawn which potentially affects the entire future direction of ultrasonic blood flow measurement. That is, if correlation processing is to be employed to determine the velocity of blood at a particular location within the vessel, then an instrument of relatively poor Doppler resolving capability must be accepted.

If higher velocity resolution instruments are to be realized, it appears as though techniques other than simple correlation detection will have to be employed. One approach might be to synchronize the instrument with the cardiac cycle

and thereby provide some measure of post-detection integration. However, the practicality of this technique is questionable. It might be time to break the ties with estimating Doppler profiles using correlation receivers altogether and start using the available information more efficiently. For example, the target might be redefined, not as a small subsection of the vessel, but as the entire vessel. And the entire measurement objective might change. The objective might be to estimate a specific characteristic of the target. Is the flow laminar or not? What is the mean velocity of the blood? What is the peak velocity in the aorta? etc. To accomplish these types of objectives, one might make use of knowledge such as average vessel sizes, expected flow profiles or the fact that with high probability, flow in the circulatory system is laminar.

In any specific instance the optimum choice of signal and signal processing could be significantly different from that investigated in this dissertation. One of the major objections to such an approach has traditionally been that the resulting processing would be much too complicated to implement. However, with the continued development of high speed microprocessors, this is rapidly becoming a practical alternative.

APPENDICES

The appendices A through G are tutorial in nature and are intended to provide the reader with sufficient background in Detection/Estimation Theory, in the context of blood flow imaging. Much of the notation and normalizations used in these appendices are those used in "Detection Estimation Theory", Part One and Part Three, by H. L. VanTrees. For a broader and more complete treatment of classical Detection/Estimation theory the reader is strongly advised to consult the above mentioned reference.

Appendix H is intended to familiarize the reader with the terms and equations used to describe simple acoustic wave propagation while Appendix I discusses fluid flow in circular cylindrical tubes. Both of these appendices provide useful background and could be read before the main text.

The remaining appendices are detailed mathematical derivations of results used in the main body and as such should be consulted only as required.

APPENDIX A

Vector Representation of Signals

Consider the class of functions which are zero for $t < 0$ and for $t > T$, and continuous on the interval $0 < t < T$. A typical sample function is shown in Figure A1.

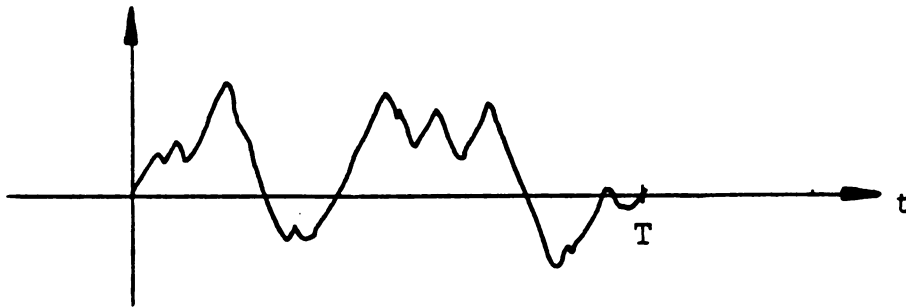


Figure A1. Typical Sample Function From a Random Process

Valuable intuition may be gained by visualizing any function in this class as a vector in an infinite dimensional space with each point on the t axis ($0 < t < T$), representing a different coordinate direction in an infinite dimensional orthogonal coordinate system. The value of the function at each instant of time represents the

magnitude of the unit vector in that coordinate direction. With this conceptualization, the operations involving addition and dot product on continuous time functions may be interpreted in the same manner as their finite dimensional counterparts. The following analogies demonstrate this for the dot product operation.

Analogies

$$A \cdot B = \sum \tilde{A}_i \tilde{B}_i^* \quad \tilde{f}(t) \cdot \tilde{g}(t) = \int_0^T \tilde{f}(t) \tilde{g}^*(t) dt \quad A.1$$

$$|\bar{A}|^2 = \sum |\tilde{A}_i|^2 \quad |\tilde{f}(t)|^2 = \int_0^T \tilde{f}(t) \tilde{f}^*(t) dt \quad A.2$$

The \sim over a function indicates that it is a complex function and the asterisk indicates the complex conjugate operation.

As with finite dimensional vectors, an infinite dimensional vector, $\tilde{f}(t)$, may be represented by any complete orthonormal set of unit vectors (CON set). These unit vectors will be designated $\tilde{\phi}_1(t)$, $\tilde{\phi}_2(t)$, $\tilde{\phi}_\infty(t)$. Notice that it takes an infinite set of unit vectors to span an infinite dimensional space. The definitions of orthonormal and complete are summarized as follows.

$$\text{orthonormal} \Rightarrow \int_0^T \tilde{\phi}_i(t) \tilde{\phi}_j^*(t) dt = \begin{cases} 0, & i \neq j \\ 1, & i = j \end{cases} \quad \text{A.3}$$

$$\text{complete} \Rightarrow \lim_{N \rightarrow \infty} \int_0^T [f(t) - \sum_{i=1}^N \tilde{f}_i \tilde{\phi}_i(t)] dt = 0 \quad \text{A.4}$$

for all $f(t)$ with finite energy

where the coefficients, \tilde{f}_i , are computed as follows:

$$\int_0^T \tilde{f}(t) \tilde{\phi}_j^*(t) dt = \int \sum \tilde{f}_i \tilde{\phi}_i(t) \tilde{\phi}_j^*(t) dt \quad \text{A.5}$$

$$= \sum \tilde{f}_i \underbrace{\int_0^T \tilde{\phi}_i(t) \tilde{\phi}_j^*(t) dt}_{\substack{1 \text{ for } i=j \\ 0 \text{ for } i \neq j}}$$

$$\tilde{f}_i = \int_0^T \tilde{f}(t) \tilde{\phi}_i^*(t) dt \quad \text{A.6}$$

The well known Fourier Series is an example of one particular orthogonal function expansion, with the expansion functions being complex exponentials.

APPENDIX B

Complex Signal Notation for Narrowband Processes

Let the transmitted carrier be $\cos(\omega_c t)$, then a transmitted signal with the most general kind of modulation can be written as

$$\begin{aligned} s_t(t) &= \sqrt{2} M(t) \cos(\omega_c t + \phi(t)) & \text{B.1} \\ &= \sqrt{2} M(t) [\cos(\omega_c t) \cos(\phi(t)) \\ &\quad - \sin(\omega_c t) \sin(\phi(t))] \end{aligned}$$

Let

$$\begin{aligned} X(t) &= M(t) \cos(\phi(t)) & \text{B.2} \\ Y(t) &= M(t) \sin(\phi(t)) \end{aligned}$$

Then $s_t(t)$ may be written as

$$\begin{aligned} s_t(t) &= \sqrt{2} [X(t) \cos(\omega_c t) - Y(t) \sin(\omega_c t)] & \text{B.3} \\ &= \text{Re} \{ \sqrt{2} [X(t) + jY(t)] [\cos(\omega_c t) \\ &\quad + j \sin(\omega_c t)] \} \end{aligned}$$

Defining the complex envelope as:

$$X(t) + jY(t) = \tilde{f}(t) = \text{complex envelope} \quad \text{B.4}$$

the transmitted signal is:

$$s_t(t) = \text{Re} \{ \sqrt{2} \tilde{f}(t) e^{j\omega_c t} \} \quad \text{B.5}$$

Also, from equations B.4 and B.2, $\tilde{f}(t)$ may be written as

$$\tilde{f}(t) = M(t) e^{j\phi(t)} \quad \text{B.6}$$

Thus for signals which are "narrowband" about some arbitrary carrier frequency ω_c , the quadrature components $X(t)$ and $Y(t)$, the amplitude modulation $M(t)$, and the phase modulation $\phi(t)$, may be found by performing the operations indicated in equations B.7 through B.10. The operation designated as $[\cdot]_{LP}$ implies an ideal low pass filter operation and assumes the signal is sufficiently narrowband so that negligible aliasing occurs.

$$\left. \begin{aligned} X(t) &= [\sqrt{2} s(t) \cos(\omega_c t)]_{LP} \\ Y(t) &= [\sqrt{2} s(t) \sin(\omega_c t)]_{LP} \end{aligned} \right\} \begin{array}{l} \text{Quadrature} \\ \text{Components} \end{array} \quad \begin{array}{l} \text{B.7} \\ \text{B.8} \end{array}$$

$$M(t) = [X^2(t) + Y^2(t)]^{\frac{1}{2}} \quad \text{B.9}$$

$$\phi(t) = \tan^{-1} \frac{Y(t)}{X(t)} \quad \text{B.10}$$

Let the Fourier transform of $s_t(t)$ be

$$S_t(f) = F\{s_t(t)\} \quad \text{B.11}$$

where $F\{\cdot\}$ is the Fourier transform operation.

Since $s_t(t)$ is real:

$$S(f) = S^*(-f) \quad \text{B.12}$$

or

$$|S(f)|^2 = |S(-f)|^2 \quad \text{B.13}$$

A typical signal spectrum is shown in Figure B1.

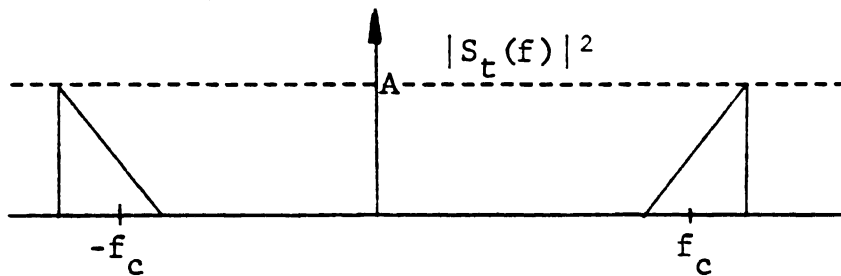


Figure B1. Typical Signal Spectrum

No

Sc

al

1

t

A

Si

Note that in general

$$\operatorname{Re}\{\tilde{A}\} = \frac{1}{2} \{\tilde{A} + \tilde{A}^*\}$$

so that from equation B.5

$$s_t(t) = \frac{\sqrt{2}}{2} [\tilde{f}(t)e^{j2\pi f_c t} + f^*(t)e^{-j2\pi f_c t}] \quad \text{B.14}$$

and therefore the Fourier transform of $s_t(t)$ may be written in terms of the Fourier transform of the complex envelope as:

$$\begin{aligned} S_t(f) &= F\{s_t(t)\} \\ &= \frac{1}{\sqrt{2}} F(f-f_c) + \frac{1}{\sqrt{2}} F^*(-f-f_c) \end{aligned} \quad \text{B.15}$$

As an example, the spectrum of the complex envelope of the typical signal shown in figure B1 is shown in Figure B2.

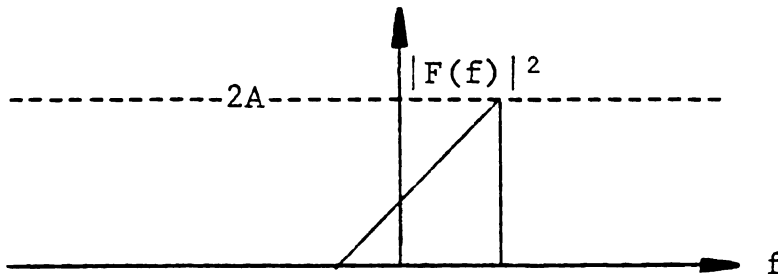


Figure B2. Spectrum of Complex Envelope

A few important examples of the complex envelope of typical signals are given below.

A. Amplitude Modulation:

$$1) \quad s_t(t) = \sqrt{2} M(t) \cos(2\pi f_c t) \quad \text{B.16}$$

$$\tilde{f}(t) = M(t) \quad \text{B.17}$$

$$2) \quad s_t(t) = \sqrt{2} M(t) \sin(2\pi f_c t) \quad \text{B.18}$$

$$\tilde{f}(t) = M(t) e^{-j \frac{\pi}{2}} \quad \text{B.19}$$

3) On/Off Sequence

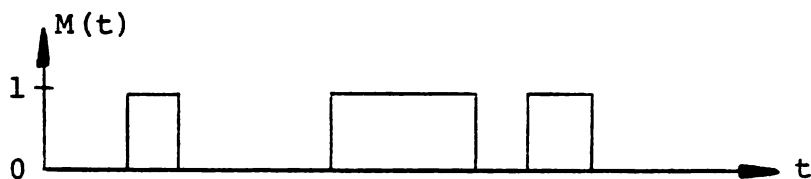


Figure B3. Sample On/Off Sequence

$$s_t(t) = \sqrt{2} M(t) \cos(2\pi f_c t) \quad \text{B.20}$$

$$\tilde{f}(t) = M(t) \quad \text{B.21}$$

B. Phase Modulation:

$$1) \quad s_t(t) = \sqrt{2} \cos[(2\pi f_c t) + \phi(t)] \quad \text{B.22}$$

$$\tilde{f}(t) = e^{j\phi(t)} \quad \text{B.23}$$

2) Binary-Phase Sequence

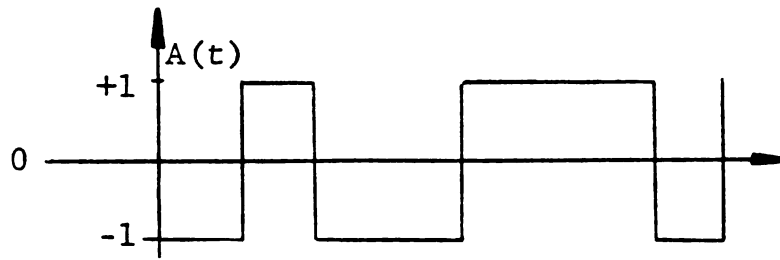


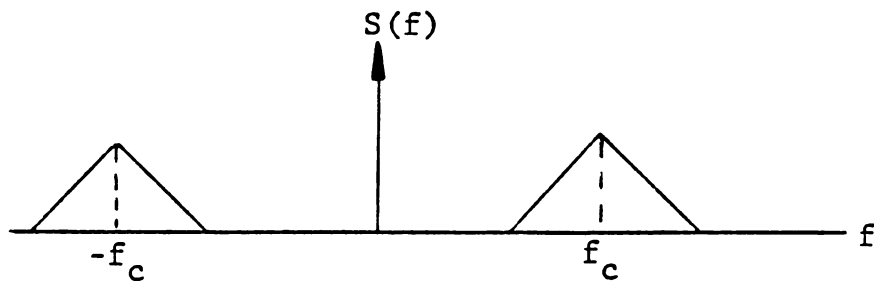
Figure B4. Sample Binary-Phase Sequence

$$s_t(t) = \sqrt{2} A(t) \cos(2\pi f_c t) \quad \text{B.24}$$

$$\tilde{f}(t) = e^{j\pi[1-A(t)]/2} \quad \text{B.25}$$

Notes:

1. The choice of f_c is somewhat arbitrary.
2. $\tilde{f}(t)$ is real if we choose f_c such that $[S(f-f_c)]_{LP}$ is symmetric as illustrated in Figure B5.

Figure B5. Symmetric $[S(f-f_c)]_{LP}$

$$3. \quad \tilde{f}(t) = [\sqrt{2} s_t(t) e^{-j2\pi f_c t}]_{LP} \quad \text{B.26}$$

Complex Representation of Transfer Functions

By definition, the system transfer function, $H(\omega)$, is the Fourier transform of the system impulse response, $h(t)$. In this section it is assumed that the system transfer function is narrowband about ω_c , as illustrated in Figure B6.

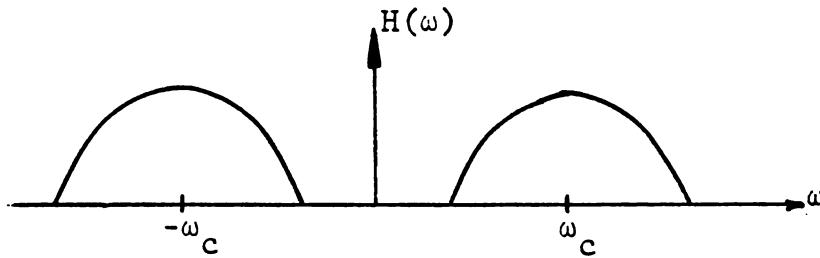


Figure B6. Example of a Narrowband Transfer Function

The complex impulse response $\tilde{h}(t)$, can be defined by the following relationship:

$$h(t) = \text{Re} [2\tilde{h}(t)e^{j\omega_c t}] \quad \text{B.27}$$

where

$$h(t) = h_c(t) - jh_s(t)$$

$$h_c(t) = [h(t) \cos(\omega_c t)]_{LP}$$

$$h_s(t) = [h(t) \sin(\omega_c t)]_{LP}$$

Notice that equation B.5 and equation B.27 are different by a factor of 2. This normalization is chosen so that equation B.28 will be consistent with conventional system theory. That is, the complex envelope of the response of $\tilde{h}(t)$ to $\tilde{f}(t)$ is the familiar convolution integral.

$$\tilde{y}(t) \cong \int_{-\infty}^{\infty} \tilde{h}(t-\tau) \tilde{f}(\tau) d\tau \quad \text{B.28}$$

and the actual response is written as

$$y(t) = \text{Re} \{ \sqrt{2} \tilde{y}(t) e^{j\omega_c t} \} \quad \text{B.29}$$

APPENDIX C

Bandpass Random Processes

If $n(t)$ is a random time function (Stochastic process) essentially band limited, it may be written in terms of its complex envelope (see Appendix B) as:

$$\tilde{n}(t) = [\sqrt{2} n(t) e^{-j\omega_c t}]_{LP} \quad C.1$$

$$n(t) = \text{Re} \{ \sqrt{2} \tilde{n}(t) e^{j\omega_c t} \} \quad C.2$$

As with deterministic signals,

$$\tilde{n}(t) = n_c(t) - jn_s(t) \quad C.3$$

$$n_c(t) = [\sqrt{2} n(t) \cos(\omega_c t)]_{LP} \quad C.4$$

$$n_s(t) = [\sqrt{2} n(t) \sin(\omega_c t)]_{LP} \quad C.5$$

For stationary processes

$$\tilde{S}_{\tilde{n}}(f) = 2[S_n(f + f_c)]_{LP} \quad C.6$$

Figure C1 illustrates the relationship between the actual spectrum for a random process and its complex counterpart.

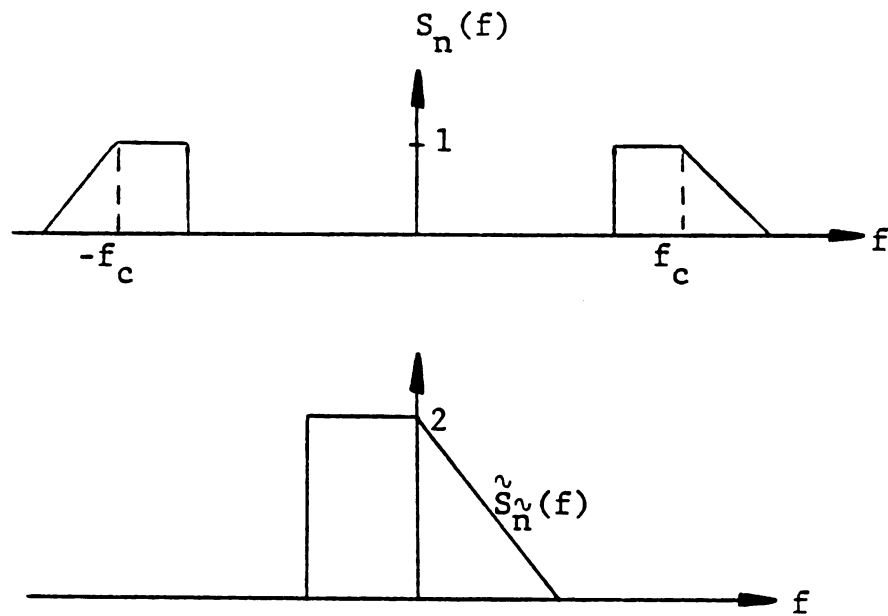


Figure C1. Example of a Complex Envelope Spectrum

where

$$\tilde{S}_n(f) = |F\{\tilde{n}(t)\}|^2$$

Two very important properties of $\tilde{n}(t)$ are:

$$1) \quad E\{\tilde{n}(t_1)\tilde{n}(t_2)\} = 0 \quad \text{for all } t_1 \text{ and } t_2 \text{ if } f_c > \text{BW}$$

[BW = bandwidth of $s(t)$]

$$2) \quad F^{-1}\{[2S_n(f+f_c)]_{LP}\} = \tilde{R}_n(t_1-t_2) \triangleq E\{\tilde{n}(t)\tilde{n}^*(t-(t_1-t_2))\}$$

where $\tilde{R}_n(t_1, t_2)$ is by definition the correlation function for the complex process.

Also, the covariance function for the complex process will be defined as $\tilde{K}_n^v(t_1, t_2)$.

If the process is stationary

$$\tilde{R}_n^v(t_1, t_2) = \tilde{R}_n^v(\tau) \quad \tau = t_1 - t_2 \quad \text{C.7}$$

$$\tilde{K}_n^v(t_1, t_2) = \tilde{K}_n^v(\tau) \quad \tau = t_1 - t_2 \quad \text{C.8}$$

If the process is also zero mean, the covariance function equals the correlation function.

$$\tilde{K}_n^v(\tau) = \tilde{R}_n^v(\tau) \quad \text{for zero mean stationary processes} \quad \text{C.9}$$

Only zero mean stationary processes will be considered. This implies that all processing will occur during a time interval for which the process is stationary. (This will be an important constraint when working with time dependent blood flow and suggests extensions of the work reported herein.)

Using the identity, $\text{Re}\{\tilde{A}\} = (\tilde{A} + \tilde{A}^*)/2$, the relationship between $\tilde{K}_n^v(\tau)$ and $K_n(\tau)$ can be derived as follows.

$$\begin{aligned}
K_n(t, t-\tau) &= E\{n(t)n(t-\tau)\} \\
&= E\left\{\left[\frac{\sqrt{2} \hat{n}(t)e^{j2\pi f_c t} + \sqrt{2} \hat{n}^*(t)e^{-j2\pi f_c t}}{2}\right]\right. \\
&\quad \left.\times \left[\frac{\sqrt{2} \hat{n}(t-\tau)e^{j2\pi f_c (t-\tau)} + \sqrt{2} \hat{n}^*(t-\tau)e^{-j2\pi f_c (t-\tau)}}{2}\right]\right\} \\
&= \operatorname{Re} [K_n^{\sim}(\tau)e^{j2\pi f_c \tau}] \\
&\quad + \operatorname{Re}[E\{\hat{n}(t)\hat{n}(t-\tau)e^{j2\pi f_c (t-\tau)}\}]
\end{aligned}$$

Using property one

$$E\{\hat{n}(t)\hat{n}(t-\tau)e^{j2\pi f_c (t-\tau)}\} = 0 \quad \text{for } f_c > \text{BW} \quad \text{C.10}$$

Thus,

$$\boxed{K_n(\tau) = \operatorname{Re} [K_n^{\sim}(\tau)e^{j2\pi f_c \tau}]} \quad \text{C.11}$$

Now, since

$$S_n(f) = F^{-1}\{K_n(\tau)\}$$

$$= F^{-1} \left\{ \frac{\tilde{K}_n(\tau) e^{j2\pi f_c \tau} + \tilde{K}_n^*(\tau) e^{-j2\pi f_c \tau}}{2} \right\}$$

$$S_n(f) = \frac{\tilde{S}_n(f - f_c) + \tilde{S}_n(-f - f_c)}{2}$$

C.12

The relationship expressed by equation C.12 is illustrated in Figure C1.

Included here are some additional comments on complex processes.

1. $\tilde{K}_n(\tau)$ is real if $\tilde{S}_n(f)$ is even.

2. $K_n(\tau) = \text{Re}[\tilde{K}_n(\tau) e^{j2\pi f_c \tau}]$

3. $K_c(\tau) = E[n_c(\tau)n_c(t-\tau)]$

$$K_c(\tau) = K_s(\tau) = \frac{1}{2} \text{Re}[\tilde{K}_n(\tau)]$$

$K_c(\tau)$ and $K_s(\tau)$ are even.

4. $K_{sc}(\tau) = -K_{cs}(\tau) = -K_{sc}(-\tau) = \frac{1}{2} \text{Im}[\tilde{K}_n(\tau)]$

$$K_{sc}(0) = 0$$

$K_{sc}(\tau)$ is odd.

5. All complex covariance functions are Hermitian; i.e.,

$$\tilde{K}_n(\tau) = \tilde{K}_n^*(-\tau)$$

Complex White Process

White noise, $w(t)$, has a two sided spectral height = $N_0/2$, i.e.,

$$F\{E[w(t)w(t+\tau)]\} = F\{\frac{N_0}{2} \delta(\tau)\} = \frac{N_0}{2} \quad \text{C.13}$$

Band limited white noise, $w_B(t)$, has a spectrum similar to that shown in Figure C2.

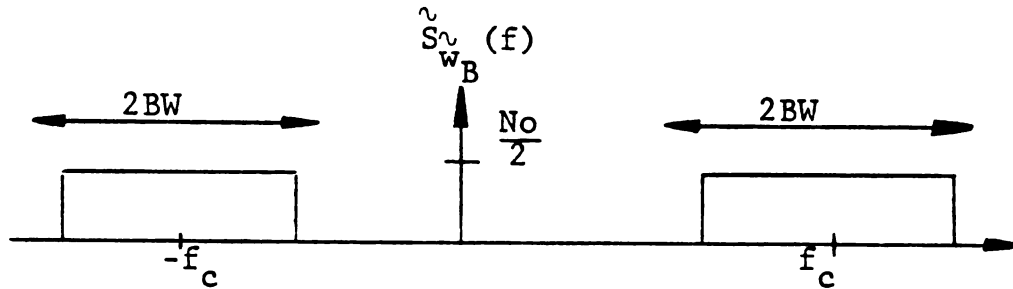


Figure C2. Example of Band Limited White Noise

The spectrum of $\tilde{w}_B(t)$ is $[2S_{w_B}(f+f_c)]_{LP}$

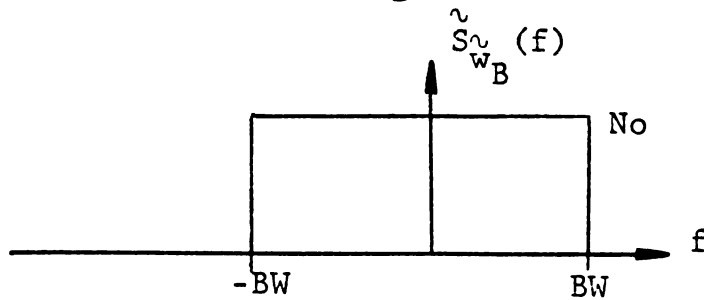


Figure C3. Spectrum of $\tilde{w}_B(t)$

and the complex covariance function of $\tilde{w}_B(t)$ is:

$$\begin{aligned}\tilde{K}_{w_B}(\tau) &= F^{-1}\{[2S_{w_B}(f+f_c)]_{LP}\} \\ &= N_0 \frac{\sin(2\pi \cdot BW \cdot \tau)}{\pi \tau}\end{aligned}$$

If BW is larger than other bandwidths of the system, the process appears white. That is,

$$\tilde{K}_{w_B}(\tau) \approx N_0 \delta(\tau) = 2K_w(\tau) \quad \text{C.14}$$

Complex Gaussian Process

Before describing a complex Gaussian process it is helpful to be familiar with a real Gaussian process. The Stochastic process, $x(t)$, is a Gaussian process if for any $g(t)$, y is a Gaussian random variable, where:

$$y = \int_0^T g(t)x(t)dt \quad \text{C.15}$$

That is,

$$p_y(y) = \frac{1}{\sqrt{2\pi\sigma^2}} e^{-\frac{(y-m)^2}{2\sigma^2}} \quad \text{C.16}$$

$$m = E\{y\}$$

$$\sigma^2 = E\{(y-m)^2\}$$

Though not a definition, for the purposes of this dissertation it will be sufficient to know that the complex envelope of any zero mean Gaussian process is a legitimate complex Gaussian process. This implies that the quadrature components of a Gaussian process are themselves Gaussian processes with identical mean and covariance functions. If the quadrature components of a zero mean Gaussian process are sampled at the same time, then those samples are jointly Gaussian random variables.

But since by property 4

$$E[n_c(t_1)n_s(t_1)] = K_{cs}(0) = 0$$

the quadrature components are uncorrelated and therefore statistically independent such that:

$$p(N_c, N_s) = \frac{1}{2\pi\sigma^2} e^{-\left[\frac{N_c^2 + N_s^2}{2\sigma^2}\right]} \quad \text{C.17}$$

In other words,

$$\begin{aligned} \Pr[N_c < n_c(t_1) < N_c + dN_c, N_s < n_s(t_1) < N_s + dN_s] \\ = p(N_c, N_s) dN_c dN_s \end{aligned}$$

Converting to polar coordinates

$$\begin{aligned}
 |N|^2 &= N_c^2 + N_s^2 \\
 \phi &= \tan^{-1} \left(\frac{N_s}{N_c} \right) \\
 dN_c dN_s &= N d\phi dN \\
 p_{N,\phi}(N, \phi) &= \frac{1}{2\pi} \frac{N}{\sigma^2} e^{-\frac{N^2}{2\sigma^2}}
 \end{aligned} \tag{C.18}$$

where

$$\begin{aligned}
 \sigma^2 &= E[n_c^2(t_1)] \\
 &= E[n_s^2(t_1)] \\
 &= K_c(o) = K_s(o) = \frac{1}{2} \tilde{K}_n(o)
 \end{aligned} \tag{C.19}$$

For white noise

$$K_c(o) = K_s(o) = \frac{N_o}{2} \tag{C.20}$$

Also, note that

$$\tilde{K}_n(o) = E[\hat{n}(t_1)^2] = 2\sigma^2 = 2E\{(n(t_1))^2\} \tag{C.21}$$

It is evident from the form of $p(N, \phi)$ that ϕ and N are independent random variables with probability density functions.

$$p(N) = \frac{N}{\sigma^2} e^{-\frac{N^2}{2\sigma^2}} = \text{Rayleigh} \quad \text{C.22}$$

$$E[N] = \sqrt{\frac{\pi\sigma^2}{2}} \quad \text{C.23}$$

$$E[N^2] = \tilde{K}_{\tilde{n}}(0) = 2\sigma^2 \quad \text{C.24}$$

$$p(\phi) = \frac{1}{2\pi} \quad \phi \in [0, 2\pi] \quad \text{C.25}$$

For future reference it is also worth noting that if $\tilde{x}(u)$ is the complex envelope of the zero mean Gaussian process $x(u)$, then \tilde{y} is a complex Gaussian random variable whenever related to $\tilde{x}(u)$ through an integral of the form

$$\tilde{y} = \int_0^T \tilde{y}(u) \tilde{x}(u) du \quad \text{C.26}$$

APPENDIX D

Hypothesis Testing for Bloodflow Imaging

To begin, a situation will be described which is similar to that which occurs in imaging blood flow. Suppose that at time $t = 0$, a transmitter may or may not be switched on. If it is switched on, the signal that is transmitted is a sample function from a Gaussian random process. If it is not switched on, nothing is transmitted. Before the signal is received, white Gaussian noise of spectral height $N_0/2$ is added to it. (The transmitted signal lasts for T seconds.) The decision which must be made is whether or not the transmitter was switched on.

The complex envelope of the transmitted signal is a sample function from a complex Gaussian process and is represented as $\tilde{s}_t(t)$.

The received signal is

$$\tilde{r}(t) = \begin{cases} \tilde{w}(t) & H_0 \text{ (transmitter off)} \\ \tilde{s}_t(t) + \tilde{w}(t) & H_1 \text{ (transmitter on)} \end{cases} \quad \text{D.1}$$

As described in Appendix A, $\tilde{r}(t)$ may be represented as a vector in "signal space" with the set $\{\tilde{\phi}_i(t)\}$ as the set of basis vectors (functions) in the following manner.

$$\tilde{r}(t) = \sum_{i=1}^{\infty} \tilde{r}_i \tilde{\phi}_i(t) \quad \text{D.2}$$

where

$$\begin{aligned} \tilde{r}_i &= \int_0^T \tilde{r}(t) \tilde{\phi}_i^*(t) dt \\ &= \text{the component of } \tilde{r}(t) \text{ in the} \\ &\quad \text{direction of } \tilde{\phi}_i(t) \end{aligned}$$

and \tilde{r}_i is a complex Gaussian random variable.

Then $\tilde{r}(t)$ and $[\tilde{r}_1, \tilde{r}_2, \dots, \tilde{r}_\infty]^T$ may be considered two representations of the same vector in signal space.

Conceptually, the set of $[\tilde{r}_i]$ may be generated by one of a couple of methods. First and most obvious is the correlator implementation shown in Figure D1.

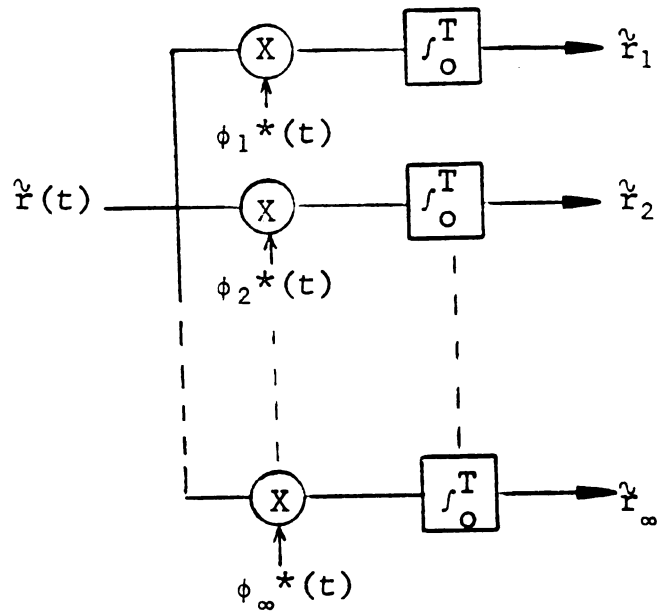


Figure D1. Correlator Implementation

An equivalent method using matched filters is shown in Figure D2.

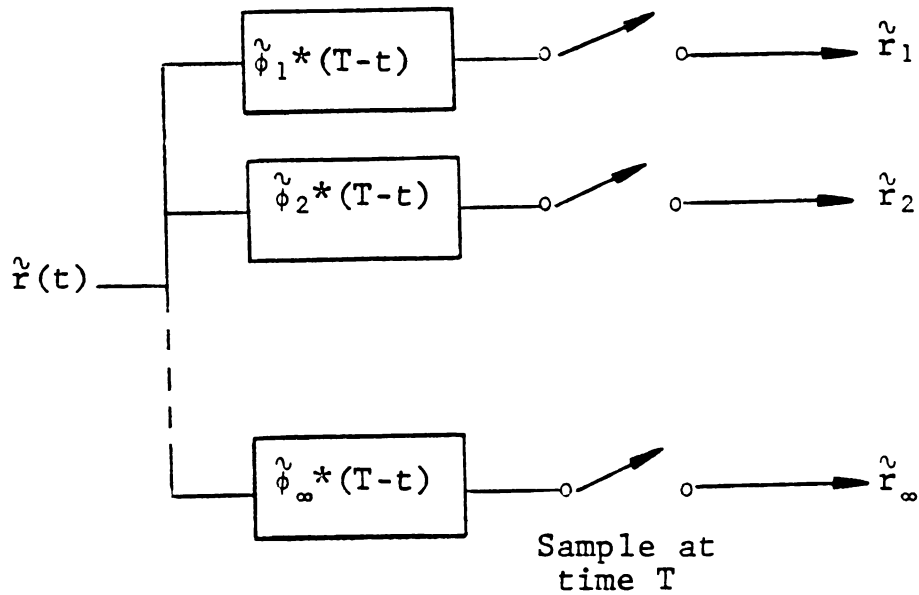


Figure D2. Matched Filter Implementation

For notational convenience let

$$\bar{\mathbf{r}} = [\hat{r}_1, \hat{r}_2, \dots, \hat{r}_\infty]^T$$

Suppose that the vector $\bar{\mathbf{r}}$ has been received and a decision about the state of the transmitter must be made. To minimize the probability of error H_1 will be chosen if it is more probable than H_0 ; i.e., if

$$P(H_1 | \bar{\mathbf{r}}) > P(H_0 | \bar{\mathbf{r}})$$

$$\frac{p(H_1, \bar{\mathbf{r}})}{p(\bar{\mathbf{r}})} > \frac{p(H_0, \bar{\mathbf{r}})}{p(\bar{\mathbf{r}})}$$

$$p(\bar{\mathbf{r}} | H_1) P(H_1) > p(\bar{\mathbf{r}} | H_0) P(H_0)$$

$$\underbrace{\frac{p(\bar{\mathbf{r}} | H_1)}{p(\bar{\mathbf{r}} | H_0)}}_{\text{Likelihood ratio } \Lambda(\bar{\mathbf{r}})} \underset{H_0}{\overset{H_1}{\geq}} \underbrace{\frac{P(H_0)}{P(H_1)}}_{\text{Threshold, } \gamma'}$$

Therefore this hypothesis test may be written as

$$\Lambda(\bar{\mathbf{r}}) \underset{H_0}{\overset{H_1}{\geq}} \gamma'$$

D.3

Note that this simply is a special case of the Bayes test. For Bayes test the threshold is slightly more complicated to reflect the costs associated with making a decision.

$$\gamma'' = \frac{P(H_0)[C_{10} - C_{00}]}{P(H_1)[C_{01} - C_{11}]}$$

where

C_{00} = the cost associated with correctly deciding H_0 is true

C_{11} = the cost associated with correctly deciding H_1 is true

C_{01} = the cost associated with incorrectly deciding H_0 is true when in fact H_1 is true

C_{10} = the cost associated with incorrectly deciding H_1 is true when in fact H_0 is true

Since $\Lambda(\bar{R})$ is a function of random variables, Λ is itself a random variable with probability density

$$p(\Lambda) = p(\Lambda | H_1)P(H_1) + p(\Lambda | H_0)P(H_0)$$

D.4

The false alarm and detection probabilities may be written as

$$P_F = \int_{\gamma}^{\infty} p(\Lambda | H_0) d\Lambda \quad D.5$$

$$P_D = \int_{\gamma}^{\infty} p(\Lambda | H_1) d\Lambda \quad D.6$$

If the apriori probabilities, $P(H_0)$ and $p(H_1)$ are not known, then the threshold, γ' , for minimum probability of error is now known.

A reasonable alternative would be to specify an acceptable P_F or P_D and solve the appropriate error expression given in equations D.5 and D.6 for γ' . The test still takes the form

$$\Lambda(\bar{R}) \begin{matrix} H_1 \\ \geq \\ H_0 \end{matrix} \gamma'$$

By choosing γ' in this way, the Neyman-Pearson decision rule has been specified. In fact, this decision rule maximizes (minimizes) P_D (P_F) given that we have chosen γ' to provide a particular P_F (P_D).

A set of curves known as the Receiver Operating Characteristics (ROC) relate P_D , P_F , γ' , and SNR in a specific application. A typical example is shown in Figure D3.

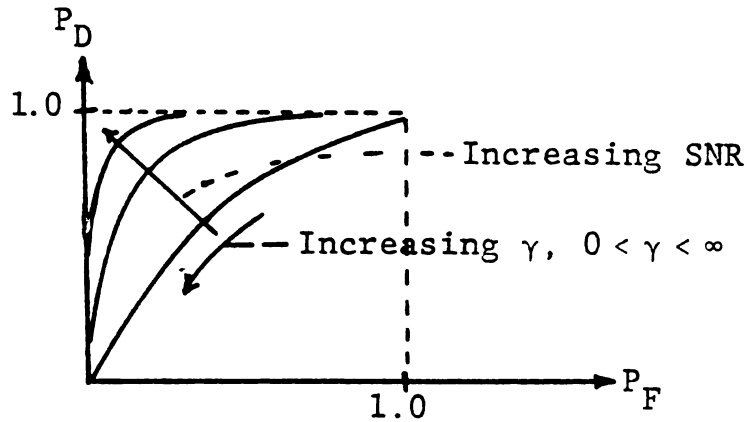


Figure D3. Typical Receiver Operating Characteristics

Note the curves in any ROC are concave down and lie above the $P_F = P_D$ line.

The specific case where the components of $\bar{\mathbf{R}}$ are complex Gaussian random variables will be examined next.

First, it is convenient to choose a coordinate system such that the components of $\tilde{\mathbf{r}}(t)$ (i.e., the components of $\bar{\mathbf{R}}$) are uncorrelated. To do so it is important to recognize that the components of a complex white noise process are uncorrelated in any orthogonal coordinate system. Therefore, referring to equation D.1, it is only necessary to find an appropriate coordinate system for $\tilde{\mathbf{S}}_t(t)$.

Thus, for the components of $\bar{\mathbf{R}}$ to be uncorrelated, the equality of equation D.7 must be satisfied.

$$E\{\tilde{S}_i \tilde{S}_j^*\} = \lambda_i \delta_{ij} \quad \text{D.7}$$

Substituting for the components of $\tilde{S}_t(t)$

$$\begin{aligned} \lambda_i \delta_{ij} &= E\left\{\int_0^T \tilde{S}_t(t) \tilde{\phi}_i^*(t) dt \left[\int_0^T \tilde{S}_t(u) \tilde{\phi}_j^*(u) du\right]^*\right\} \\ &= E\left\{\int_0^T \tilde{S}_t(t) \tilde{\phi}_i^*(t) dt \int_0^T \tilde{S}_t^*(u) \tilde{\phi}_j(u) du\right\} \\ \lambda_i \delta_{ij} &= \int_0^T \tilde{\phi}_i^*(t) \int_0^T \underbrace{E\{\tilde{S}_t(t) \tilde{S}_t^*(u)\}}_{\tilde{K}_S^*(t,u)} \tilde{\phi}_j(u) du dt \\ &\quad \text{for zero mean} \end{aligned}$$

$$= \int_0^T \tilde{\phi}_i^*(t) \int_0^T \tilde{K}_S^*(t,u) \tilde{\phi}_j(u) du dt$$

For this equality to hold for a specific j and any i , it is sufficient that

$$\int_0^T \tilde{K}_S^*(t,u) \tilde{\phi}_j(u) du = \lambda_j \tilde{\phi}_j(t) \quad \text{D.8}$$

This is a sufficient requirement because the set of functions, $\{\phi_i(t)\}$, which solve the above integral equation form an orthogonal set.

Again note the similarity between the above integral "Eigenfunction" equation and the matrix Eigenvector equation:

$$[K]\bar{\phi} = \lambda \bar{\phi}$$

$$\sum_j K_{ij} \phi_j = \lambda \phi_i \quad \text{for all } i$$

The set of functions $\{\phi(t)\}$ are called Eigenfunctions of $\tilde{K}_S(t,u)$ and the set $\{\lambda_i\}$ are called the associated Eigenvalues.

Other important properties of the Eigenfunctions and Eigenvalues of $\tilde{K}_S(t,u)$ are:

$$1. \quad \tilde{K}_S(t,u) = \sum_{i=1}^{\infty} \lambda_i \phi_i(t) \phi_i^*(u) \quad [\text{Mercers Theorem}]$$

2. λ_i is the expected energy in the $\phi_i(t)$ component of $\tilde{S}_t(t)$ and the total expected energy in $\tilde{S}_t(t)$ is

$$\begin{aligned} E\left\{\int_0^T \tilde{S}_t(t) \tilde{S}_t^*(t) dt\right\} &= \int_0^T \tilde{K}_S(t,t) dt \\ &= \sum_{i=1}^{\infty} \lambda_i \end{aligned}$$

3. Because $\tilde{K}_S(t,u)$ is Hermitian, the Eigenvalues, λ_i , are real (this is not surprising in light of 2).

$$4. \quad \int \phi_i(t) \phi_j^*(t) dt = \delta_{ij} \quad \text{as already stated.}$$

5. There exists at least one $\tilde{\phi}(t)$ and real $\tilde{\lambda}$ which satisfies

$$\tilde{\lambda}\tilde{\phi}(t) = \int_0^T \tilde{K}_S^{\tilde{\lambda}}(t,u)\tilde{\phi}(u)du$$

There may be only one. For example

$$\tilde{K}_S^{\tilde{\lambda}}(t,u) = \tilde{f}(t)\tilde{f}^*(u)$$

6. For a real bandpass process, the real Eigenvectors and Eigenfunctions are related to the complex Eigenvectors and Eigenfunctions as follows:

$$\lambda_1 = \frac{\tilde{\lambda}_1}{2} \quad \phi_1(t) = \text{Re}[\sqrt{2} \tilde{\phi}_1(t)e^{j\omega_c t}]$$

$$\begin{aligned} \lambda_2 = \lambda_1 = \frac{\tilde{\lambda}_1}{2} \quad \phi_2(t) &= \text{Re}[\sqrt{2} \tilde{\phi}_1(t)e^{-j(\pi/2)} e^{j\omega_c t}] \\ &= \text{Re}[\sqrt{2} \tilde{\phi}_1(t)e^{j(\omega_c t - \pi/2)}] \end{aligned}$$

$$\lambda_3 = \frac{\tilde{\lambda}_2}{2} \quad \phi_3(t) = \text{Re}[\sqrt{2} \tilde{\phi}_2(t)e^{j\omega_c t}]$$

$$\lambda_4 = \lambda_3 \quad \phi_4(t) = \text{Re}[\sqrt{2} \tilde{\phi}_2(t)e^{j(\omega_c t - \pi/2)}]$$

$$7. \quad \sum_{i=1}^{\infty} \tilde{\phi}_i^*(u)\tilde{\phi}_i(t) = \delta(t-u)$$

The resulting expansion of $\tilde{S}_t(t)$ in terms of the Eigenfunctions of $\tilde{K}_S^{\tilde{\lambda}}(t,u)$ is known as the Karhunen-Loeve expansion.

$$\tilde{S}_t(t) = \sum_{i=1}^{\infty} \tilde{S}_i \tilde{\phi}_i(t) \quad \text{D.9}$$

Or equivalently, the real process may be expanded as in equation D.10.

$$S_t(t) = \sum_{i=1}^{\infty} S_i \phi_i(t) \quad \text{D.10}$$

Where the set, $\{\phi_i(t)\}$, is given in property 6 above. The coefficients are given below.

$$S_1 = \text{Re}(\tilde{S}_1) \quad , \quad S_2 = \text{Im}(\tilde{S}_1) \quad \text{D.11}$$

$$S_3 = \text{Re}(\tilde{S}_2) \quad , \quad S_4 = \text{Im}(\tilde{S}_2)$$

etc.

When H_1 is true

$$\tilde{r}(t) = \tilde{S}_t(t) + \tilde{w}(t)$$

If $\tilde{r}(t) : H_1$ is expanded in terms of the Eigenfunctions of $\tilde{K}_g(t,u)$, the resulting coefficients are zero mean independent complex Gaussian random variables with a joint probability density function given as

$$p(\bar{R}|H_1) = \prod_{i=1}^{\infty} \frac{|\tilde{r}_i|}{2\pi\sigma^2} e^{-\frac{|\tilde{r}_i|^2}{2\sigma^2}} \quad D.12$$

where

$$2\sigma^2 = \tilde{\lambda}_i + N_0$$

Similarly, on H_0

$$\tilde{r}(t) = \tilde{w}(t)$$

and

$$p(\bar{R}|H_0) = \prod_{i=1}^{\infty} \frac{|\tilde{r}_i|}{\pi N_0} e^{-\frac{|\tilde{r}_i|^2}{N_0}} \quad D.13$$

The resulting likelihood ratio is given in equation D.14.

$$\begin{aligned} \Lambda(\bar{R}) &= \frac{p(\bar{R}|H_1)}{p(\bar{R}|H_0)} = \frac{e^{-\sum_{i=1}^{\infty} \frac{|\tilde{r}_i|^2}{\tilde{\lambda}_i + N_0}} \cdot \prod_{i=1}^{\infty} \frac{|\tilde{r}_i|}{\pi(\tilde{\lambda}_i + N_0)}}{e^{-\sum_{i=1}^{\infty} \frac{|\tilde{r}_i|^2}{N_0}} \cdot \prod_{i=1}^{\infty} \frac{|\tilde{r}_i|}{\pi N_0}} \\ &= e^{+\sum_{i=1}^{\infty} \frac{|\tilde{r}_i|^2}{N_0} - \frac{|\tilde{r}_i|^2}{\tilde{\lambda}_i + N_0}} \cdot \prod_{i=1}^{\infty} \frac{N_0}{\tilde{\lambda}_i + N_0} \end{aligned} \quad D.14$$

The likelihood ratio test is

$$\Lambda(\bar{R}) = \underset{H_0}{\overset{H_1}{\geq}} \gamma'$$

Since $\ln(\cdot)$ is a monic function an equivalent test would be

$$\underbrace{\ln[\Lambda(\bar{R})]}_{\text{Log Likelihood Ratio}} = L(\bar{R}) \underset{H_0}{\overset{H_1}{\geq}} \ln \gamma'$$

$$\ln[\Lambda(\bar{R})] = \sum_{i=1}^{\infty} \frac{\tilde{\lambda}_i}{(\tilde{\lambda}_i + N_0)N_0} |\tilde{r}_i|^2 + \sum_{i=1}^{\infty} \ln \frac{N_0}{\tilde{\lambda}_i + N_0}$$

An equivalent test becomes

$$\ell = \sum_{i=1}^{\infty} \frac{\tilde{\lambda}_i}{(\tilde{\lambda}_i + N_0)N_0} |\tilde{r}_i|^2 \underset{H_0}{\overset{H_1}{\geq}} \ln \gamma' - \sum \ln \frac{N_0}{\tilde{\lambda}_i + N_0} = \gamma \quad \text{D.15}$$

In concept, an implementation of the optimum detection scheme is shown in Figure D4.

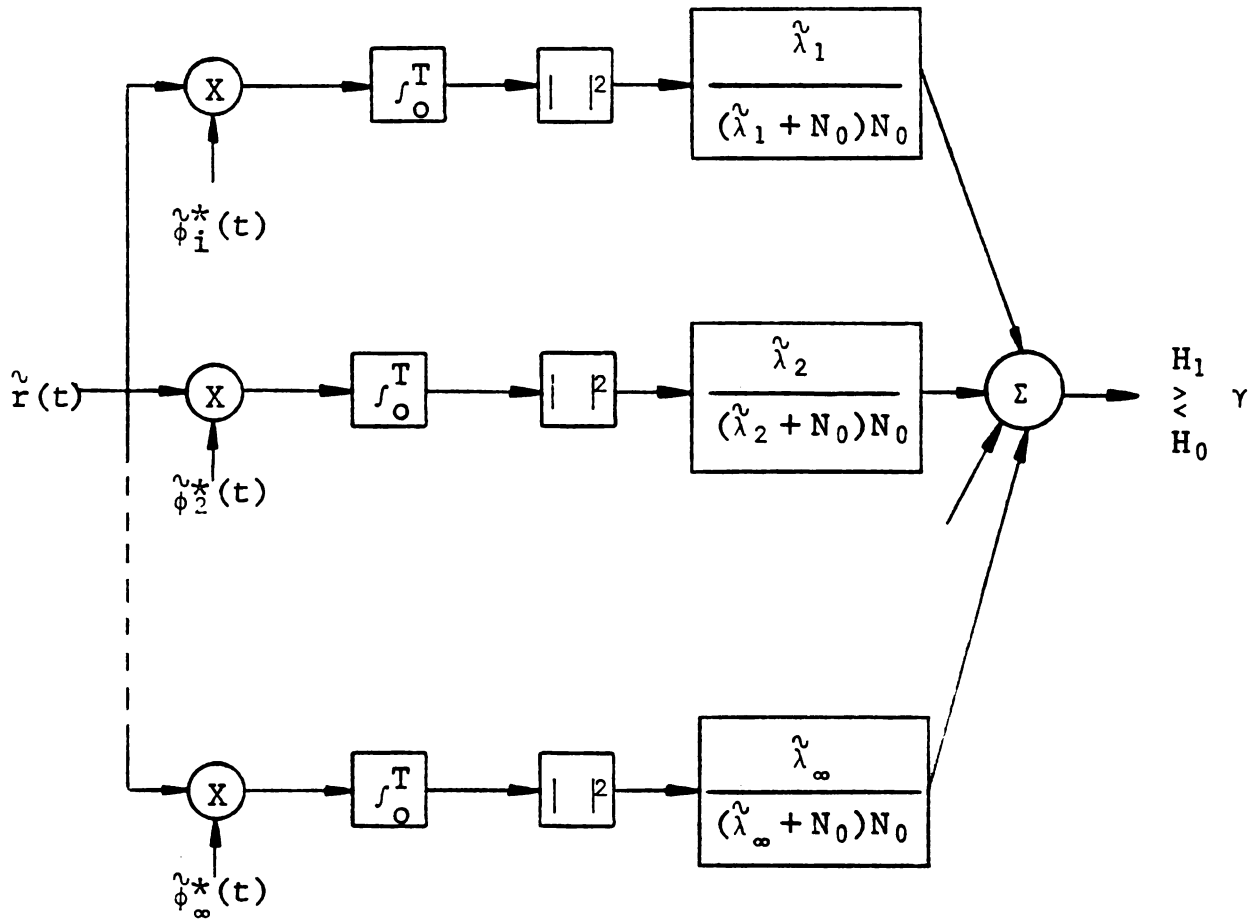


Figure D4. Optimum Detector Implementation

From equation D.15, ℓ may be rearranged as follows.

$$\begin{aligned}
 \ell &= \sum_{i=1}^{\infty} \frac{\tilde{\lambda}_i}{(\tilde{\lambda}_i + N_0)N_0} |\tilde{r}_i|^2 \\
 &= \sum_{i=1}^{\infty} \frac{\tilde{\lambda}_i}{(\tilde{\lambda}_i + N_0)N_0} \left[\int_0^T \tilde{r}(t) \tilde{\phi}_i^*(t) dt \right] \left[\int_0^T \tilde{r}(u) \tilde{\phi}_i^*(u) du \right]^*
 \end{aligned}$$

$$= \int_0^T r^*(u) \int_0^T \tilde{r}(t) \left[\sum_{i=1}^{\infty} \frac{\tilde{\lambda}_i}{(\tilde{\lambda}_i + N_0)N_0} \tilde{\phi}_i^*(t) \tilde{\phi}(u) \right] dt du$$

Defining the term in brackets as $\tilde{h}_0(t, u)$, an equivalent expression for ℓ is:

$$\ell = \int_0^T r^*(u) \int_0^T \tilde{h}_0(t, u) r(t) dt du \quad \text{D.16}$$

From equation D.16 it is seen that another form of the optimum receiver is shown in Figure D5.

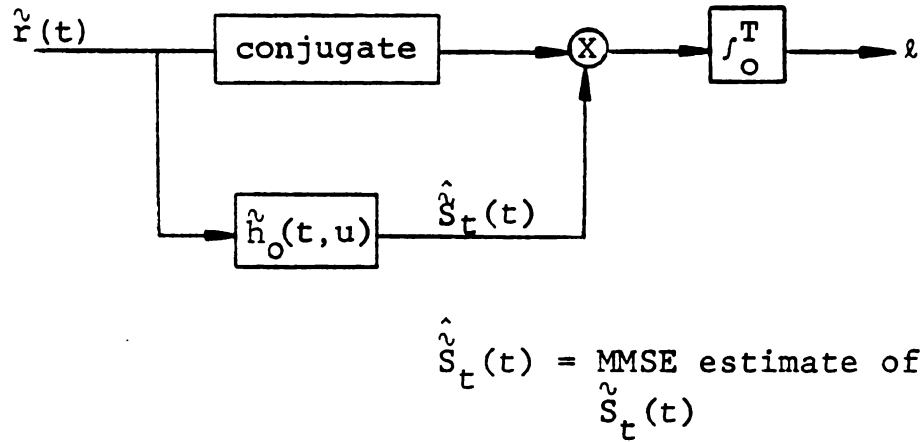


Figure D5. Filter Correlator Optimum Receiver

Thus the optimum receiver as shown in Figure D5 takes the form of a correlation receiver which correlates the complex envelope of the received signal with the minimum mean square

er

fr

E

S

error estimate of $\hat{S}_t(t)$. Actually it is possible to solve for $\hat{h}_0(t,u)$ without explicitly finding Eigenfunctions and Eigenvalues. With a lot of work it can be shown that $\hat{h}_0(t,u)$ solves:

$$N_0 \hat{h}_0(t,u) + \int_0^T \hat{h}_0(t,Z) \hat{K}_S(Z,u) dZ = \hat{K}_S(t,u) \quad D.17$$

At this point a few examples might help build up a little intuition. Two examples of particular interest will be used.

1. The transmitted signal is completely random and there is no additive white noise ($N_0 = 0$).
2. The transmitted signal is deterministic except for an unknown amplitude and phase.

$$\hat{S}_t(t) = b f(t)$$

Case 1:

With $N_0 \rightarrow 0$

$$\begin{aligned} \hat{h}_0(t,u) &= \lim_{N_0 \rightarrow 0} \frac{1}{N_0} \sum_{i=1}^{\infty} \frac{\lambda_i}{\lambda_i + N_0} \hat{\phi}_i^*(t) \hat{\phi}_i(u) \\ &= 1 \\ &= \lim_{N_0 \rightarrow 0} \frac{1}{N_0} \sum_{i=1}^{\infty} \hat{\phi}_i^*(t) \hat{\phi}_i(u) = \lim_{N_0 \rightarrow 0} \frac{1}{N_0} \delta(t-u) \end{aligned}$$

This is just the transfer function for a resistance-less wire.

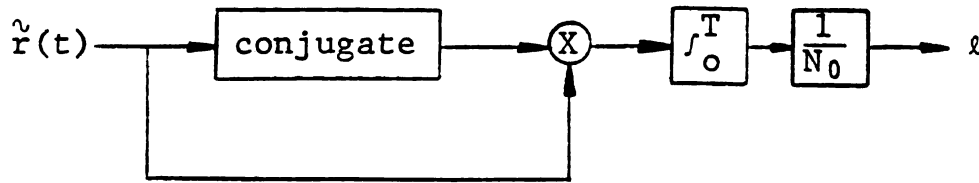


Figure D6. Optimum Receiver for N_0 Near Zero

Note that for any finite signal energy, as $N_0 \rightarrow 0$, $l \rightarrow \infty$. This means that in the absence of noise if there is any energy in the received signal, H_1 is chosen (i.e., decide the transmitter was turned on).

Case 2:

$$\tilde{S}_t(t) = \tilde{b}\tilde{f}(t) \quad E[\tilde{b}^2] = 2\sigma_b^2$$

$$E[\tilde{S}_t(t) \tilde{S}_t^*(u)] = \tilde{K}_S(t, u) = 2\sigma_b^2 \tilde{f}(t) \tilde{f}^*(u)$$

The Eigenfunctions solve

$$\lambda \tilde{\phi}(t) = \int_0^T 2\sigma_b^2 \tilde{f}(t) \tilde{f}^*(u) \tilde{\phi}(u) du$$

Let

$$\tilde{\phi}(u) = \tilde{f}(u)$$

$$\lambda \tilde{\phi}(t) = 2\sigma_b^2 \tilde{f}(t) \underbrace{\int_0^T \tilde{f}^*(u) \tilde{f}(u) du}_{= 1 \text{ by assumption}}$$

Thus it is seen that the only Eigenfunction of $\tilde{K}_S(t,u)$ is $\tilde{f}(t)$ and $\lambda = 2\sigma_b^2$.

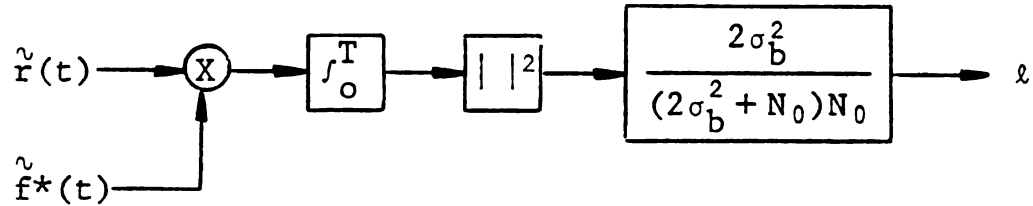


Figure D7. Optimum Receiver for Random Amplitude and Phase

Or

$$\left| \int_0^T \tilde{r}(t) \tilde{f}^*(t) dt \right|^2 \underset{H_0}{\overset{H_1}{\gtrless}} \alpha$$

This is basically a correlation receiver. The actual band-pass processing would be:

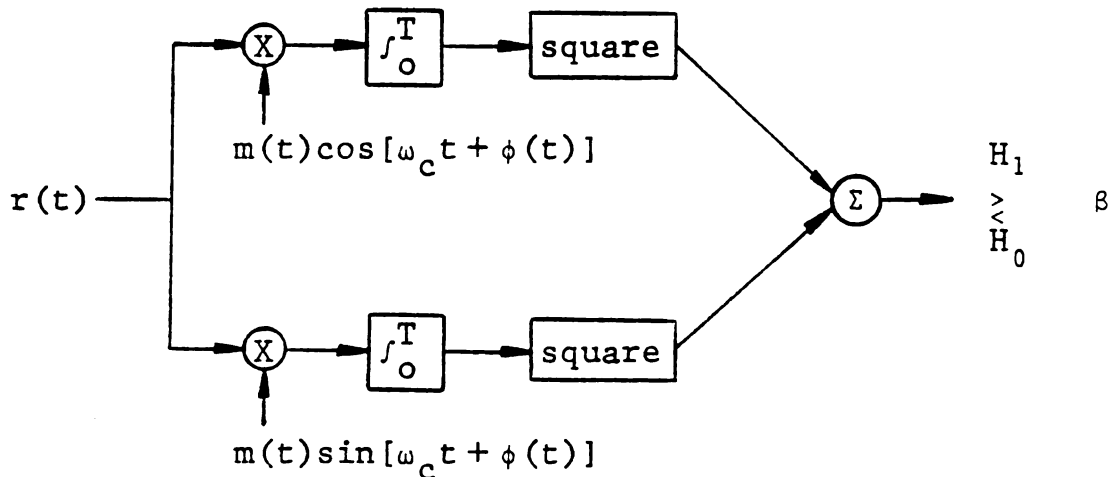


Figure D8. Bandpass Processing for Case 2

Note that this quadrature detection scheme for Case 2 is required because the absolute carrier phase is completely unknown.

APPENDIX E

Estimation Theory

To illustrate the ideas involved in estimating some parameter of a waveform, the example introduced in Appendix D will be continued. However, this time it will be assumed that there are two unknown parameters. Namely, the time of transmission is unknown and the carrier frequency is unknown.

$$\tilde{r}(t) = \tilde{S}_t(t-\tau) e^{j\omega_d t} + \tilde{w}(t) \quad \text{E.1}$$

or

$$r(t) = \text{Re}[\sqrt{2} \tilde{S}_t(t-\tau) e^{(\omega_d + \omega_c)t} + \sqrt{2} e^{j\omega_c t} \tilde{w}(t)] \quad \text{E.2}$$

Here τ and ω_d are unknown and in this specific example, τ and ω_d will be related to the range and velocity of a portion of the flowing blood within the vessel.

Suppose the "best" estimate of τ and ω_d is desired, given that $\tilde{r}(t)$ has been received.

One possible estimation procedure might be to choose those values of τ and ω_d which maximize the aposteriori probability (i.e., find those values of τ and ω_d that are most probable).

Or in other words, maximize $p(\omega_d, \tau | \bar{R})$. This is the "Maximum A Posteriori Probability" estimate or MAP estimate. Equivalently, one could maximize $\ln p(\omega_d, \tau | \bar{R})$.

By using Bayes Theorem and writing the log of products as the sum of logs, it is easily verified that a MAP estimate would maximize the expression of equation E.3.

$$\begin{aligned} \ln[p(\omega_d, \tau | \bar{R})] &= \ln[p(\bar{R} | \omega_d, \tau)] \\ &+ \ln[p(\omega_d)] + \ln[p(\tau)] - \ln[p(\bar{R})] \end{aligned} \quad \text{E.3}$$

If $p(\omega_d)$ and $p(\tau)$ are not known, or if they are uniform, or if ω_d and τ are not considered random variables, then based on equation E.3 it seems reasonable to find the values of ω_d and τ which would most likely cause us to receive the vector \bar{R} . In other words, maximize $\ln[p(\bar{R} | \omega_d, \tau)]$ over all ω_d and τ .

An equivalent procedure would be to maximize the log likelihood ratio of equation E.4.

$$\ln \left[\frac{p(\bar{R} | \omega_d, \tau)}{p(\bar{R} | H_0)} \right] = \ln \Lambda(\omega_d, \tau) \quad \text{E.4}$$

This is the so-called Maximum Likelihood estimate or "ML" estimate.

A possible solution is

$$\left. \frac{\partial}{\partial \tau} \ln \Lambda(\tau, \omega_d) \right|_{\tau = \tau_{ML}} = 0 \quad \text{E.5}$$

$$\left. \frac{\partial}{\partial \omega_d} \ln \Lambda(\tau, \omega_d) \right|_{\omega_d = \omega_{ML}} = 0 \quad \text{E.6}$$

At this point, the only reason to normalize by $p(\bar{R}|H_0)$ is so that existing results from the detection theory, which were developed in Appendix D, can be used directly in Appendix F.

APPENDIX F

Detection of a Point Target

First, assume that the transmitted signal is

$$\begin{aligned} S_t(t) &= \sqrt{2P_t} \cos(\omega_c t) \\ &= \operatorname{Re}[\sqrt{2P_t} e^{j\omega_c t}] \end{aligned} \quad \text{F.1}$$

Now assume that the target is a point target (its largest dimension $\ll \lambda$) and has many reflecting surfaces. [For example, many red blood cells (RBC's) within a small volume dv .] The return from that dv is (without additive noise):

$$S_r(t) = \operatorname{Re}[\sqrt{2P_t} \sum_{i=1}^K g_i e^{j[\omega_c(t-\tau)+\theta_i]}] \quad \text{F.2}$$

g_i includes effects of losses or gains incurred in the transmitting and receiving transducers, all propagation losses, and the scattering cross section of the i^{th} RBC. θ_i is a random phase associated with reflection from the i^{th} RBC.

$$S_r(t) = \operatorname{Re}[\sqrt{2P_t} e^{j\omega_c(t-\tau)} \sum_{i=1}^K g_i e^{j\theta_i}] \quad \text{F.3}$$

By the central limit theorem, for large K

$$\sum_{i=1}^K g_i e^{j\theta_i} \rightarrow \tilde{b} \quad \text{F.4}$$

where \tilde{b} is a complex Gaussian random variable. Thus $S_r(t)$ may be written as

$$S_r(t) = \text{Re}[\sqrt{2P_t} \tilde{b} e^{j\omega_c(t-\tau)}]$$

Now assume the transmitted signal to be:

$$\begin{aligned} S_t(t) &= \text{Re}[\sqrt{2E_t} \tilde{f}(t) e^{j\omega_c t}] \\ &= \text{Re}[\sqrt{2E_t} e^{j\omega_c t} \int_{-\infty}^{\infty} \tilde{F}(j\omega) e^{j\omega t} \frac{d\omega}{2\pi}] \end{aligned} \quad \text{F.5}$$

If the reflection process is linear and frequency independent, then:

$$\begin{aligned} S_r(t) &= \text{Re}[\sqrt{2E_t} \tilde{b} e^{j\omega_c(t-\tau)} \int_{-\infty}^{\infty} \tilde{F}(j\omega) e^{j\omega(t-\tau)} \frac{d\omega}{2\pi}] \\ &= \text{Re}[\sqrt{2E_t} \tilde{b} \tilde{f}(t-\tau) e^{j\omega_c(t-\tau)}] \end{aligned} \quad \text{F.6}$$

If the target remains within the transducer beam for time t , and has radial velocity V_r , its range is given by:

$$R(t) = R_0 - V_r \cdot t \quad \text{F.7}$$

If a particular part of the received signal is received at time t , it was transmitted at time $t - \tau(t)$, where $\tau(t)$ is the two-way propagation delay of that part of the signal received at time t . Therefore, that portion of the signal received at time t was reflected from the target at time $[t - \tau(t)/2]$. At that time, the target's range was

$$R(t - \frac{\tau(t)}{2}) = R_0 - V_r \cdot (t - \frac{\tau(t)}{2}) \quad \text{F.8}$$

and therefore, since $\tau(t) = 2R(t)/C$, where C is the velocity of sound in tissue,

$$\tau(t) = \frac{2R(t - \frac{\tau(t)}{2})}{C} = \frac{2[R_0 - V_r \cdot (t - \frac{\tau(t)}{2})]}{C} \quad \text{F.9}$$

or solving for $\tau(t)$

$$\tau(t) = \frac{\frac{2R_0/C}{1 + \frac{V_r}{C}} - \frac{\frac{2V_r \cdot t}{C}}{1 + \frac{V_r}{C}}}{1} \quad \text{F.10}$$

In the case of blood flow measurement,

$$V_{\max} \approx 10^2 \text{ cm/sec}$$

$$C \approx 1.5 \times 10^5 \text{ cm/sec}$$

$$\frac{V}{C} \approx \frac{1}{1.5} \times 10^{-3} \approx .67 \times 10^{-3} \ll 1$$

So that,

$$\tau(t) \approx \frac{2R_0}{C} - \frac{2V_r \cdot t}{C} \quad \text{F.11}$$

If τ is defined as

$$\tau = \frac{2R_0}{C}$$

Then delay as a function of time may be written as

$$\tau(t) = \tau - \frac{2V_r \cdot t}{C} \quad \text{F.12}$$

and the received signal may be written as

$$\begin{aligned} S_r(t) &= \text{Re} \left[\sqrt{2E_t} \tilde{b} \tilde{f}(t - \tau + \frac{2V}{C} t) e^{j\omega_c(t - \tau + \frac{2V}{C} t)} \right] \\ &= \text{Re} \left[\underbrace{\sqrt{2} \sqrt{E_t} \tilde{b} \tilde{f}(t - \tau + \frac{2V}{C} t) e^{j\omega_c \frac{2V}{C} t}}_{\tilde{S}_r(t)} e^{j\omega_c t} \right] \quad \text{F.13} \end{aligned}$$

Thus the complex envelope of the received signal with additive noise may be written as;

$$\tilde{r}(t) = \sqrt{E_t} \tilde{b} \tilde{f}[(1 + \alpha(\omega_d))t - \tau] e^{j\omega_d t} + \tilde{w}(t) \quad \text{F.14}$$

where

$$\alpha = \frac{2V}{C}$$

$$\omega_d = \omega_c \cdot \alpha$$

Notice that this is very similar to the problem discussed in the previous appendices. Here the complex envelope of the received signal consists of the sum of a sample function from a complex Gaussian process and a sample function from a complex Gaussian white noise process. If the Eigenfunctions of $\tilde{K}_{S_r}^{\gamma}(t,u)$ are chosen as the expansion functions for $\tilde{r}(t)$, then the individual coefficients will be uncorrelated and therefore statistically independent (because Gaussian). Thus the $\tilde{\phi}_i$'s and λ_i 's must solve the following integral equation.

$$\lambda_i \tilde{\phi}_i(t) = \int_{-\infty}^{\infty} \tilde{K}_{S_r}^{\gamma}(t,u) \tilde{\phi}_i(u) du$$

where

$$\begin{aligned} \tilde{K}_{S_r}^{\gamma}(t,u) &= E[\sqrt{E_t} \tilde{b} \tilde{f}[(1+\alpha)t-\tau] e^{j\omega_d t} \\ &\quad \cdot \sqrt{E_t} \tilde{b} \tilde{f}^*[(1+\alpha)u-\tau] e^{-j\omega_d u}] \\ &= E_t 2\sigma_b^2 \tilde{f}[(1+\alpha)t-\tau] e^{j\omega_d t} \tilde{f}^*[(1+\alpha)u-\tau] e^{-j\omega_d u} \end{aligned}$$

F.15

As demonstrated in a previous example, there is only one Eigenfunction and one Eigenvalue associated with $\tilde{K}_{S_r}^{\gamma}(t,u)$. They are:

$$\tilde{\phi}(t) = \tilde{f}[(1+\alpha(\omega_d))t-\tau] e^{j\omega_d t}$$

$$\lambda = 2\sigma_b^2 E_t = \bar{E}_R$$

Equation E.4 states that for a ML estimate, the following log likelihood ratio is to be maximized over all ω_d and τ .

$$\ln \left[\frac{p(\bar{r} | \omega_d, \tau)}{p(\bar{r} | H_0)} \right] = \ln \Lambda(\omega_d, \tau)$$

Noting the one-to-one correspondence between $\ln[\Lambda(\omega_d, \tau)]$ and $\ln \Lambda(\bar{R})$ implemented in equation D.15, the log likelihood ratio may be written immediately as

$$\ln[\Lambda(\omega_d, \tau)] = \frac{1}{N_o} \frac{\bar{E}_R}{N + \bar{E}_R} |L(\tau, \omega_d)|^2 \quad \text{F.17}$$

$$L(\tau, \omega_d) = \int_{-\infty}^{\infty} \tilde{r}(t) \tilde{f}[(1 + \alpha(\omega_d))t - \tau] e^{-j\omega_d t} dt \quad \text{F.18}$$

An equivalent estimation procedure would be to simply ignore the constant in equation F.17 and maximize $|L(\tau, \omega_d)|^2$ over all τ and ω_d .

APPENDIX G

Ambiguity Functions

Generalized Ambiguity Function

From equations F.14 and F.18, $L(\tau, \omega)$ may be written as

$$\begin{aligned}
 L(\tau, \omega) &= \int_{-\infty}^{\infty} [\sqrt{E_t} \tilde{b} \tilde{f}[(1+\alpha(\omega_a))t - \tau_a] e^{j\omega_a t} + \tilde{w}(t)] \\
 &\quad \cdot [f^*(1+\alpha(\omega))t - \tau] e^{-j\omega t} dt \\
 &= \int_{-\infty}^{\infty} \sqrt{E_t} \tilde{b} \tilde{f}[(1+\alpha(\omega_a))t - \tau_a] \\
 &\quad \tilde{f}^*[(1+\alpha(\tau))t - \tau] e^{j(\omega_a - \omega)t} dt + \tilde{n}(\tau, \omega) \quad G.1
 \end{aligned}$$

where

$$\tilde{n}(\tau, \omega) = \int_{-\infty}^{\infty} \tilde{w}(t) f^*[(1+\alpha(\omega))t - \tau] e^{-j\omega t} dt$$

and τ_a and ω_a are the actual delay and frequency shift of the received signal.

Note that

$$\begin{aligned}
 |\tilde{A} + \tilde{B}|^2 &= (\tilde{A} + \tilde{B})(\tilde{A}^* + \tilde{B}^*) = |A|^2 + \tilde{B}\tilde{A}^* + \tilde{A}\tilde{B}^* + |B|^2 \\
 &= |A|^2 + 2\text{Re}[\tilde{A}\tilde{B}^*] + |B|^2
 \end{aligned}$$

so that

$$|L(\tau, \omega)|^2 = E_t |\tilde{b}|^2 |\tilde{\phi}'(\tau, \omega)|^2 + \sqrt{E_t} \tilde{b} \tilde{\phi}'(\tau, \omega) \tilde{n}^*(\tau, \omega) + |\tilde{n}(\tau, \omega)|^2 \quad G.2$$

Here:

$$E_t |\tilde{b}|^2 |\tilde{\phi}'(\tau, \omega)|^2 = E_t |\tilde{b}|^2 \left| \int_{-\infty}^{\infty} \tilde{f}[(1+\alpha(\omega_a))t - \tau_a] \cdot \tilde{f}^*[(1+\alpha(\omega))t - \tau] e^{j(\omega_a - \omega)t} dt \right|^2 \quad G.3$$

and is the only term present in the absence of noise.

The function $\theta'(\tau, \omega) = |\phi'(\tau, \omega)|^2$ is the output of a true correlation receiver in the absence of noise and is called the generalized ambiguity function.

It is worth noting that the output of such a "true" correlation receiver is a surface in the τ, ω plane which contains three components.

The first term of $|L(\tau, \omega)|^2$ is a positive function with a maximum at the point in the τ, ω plane where the target is located, (τ_a, ω_a) . The other two terms are due to noise.

An error occurs whenever the noise terms cause the surface to have an absolute maximum value anywhere but at τ_a and ω_a . Therefore, an ideal generalized ambiguity function would appear to be a delta function centered at (τ_a, ω_a) .

Since the generalized ambiguity function is directly related to the output of a "true" correlation receiver, it could provide a convenient way to examine the resolution and performance capabilities of such a detection system.

Doppler Approximation

As has already been stated, the received signal is (see equation F.14):

$$\tilde{r}(t) = \tilde{b}\sqrt{E_t} \tilde{f}[(1+\alpha)t-\tau]e^{j\omega_d t} + \tilde{w}(t)$$

Notice that the transmitted signal is Doppler shifted and the envelope is scaled in time.

The Doppler Approximation assumes that the received signal may be treated as a Doppler shifted version of the transmitted signal; i.e., it neglects the stretching or compression of the complex envelope. However, this is not always a reasonable assumption. Consider the following.

For a waveform $\tilde{f}(t)$, which is non-zero on the interval $0 < t < T$, $\tilde{f}(t)$ and $\tilde{f}(t + \frac{2V}{C} t)$ differ the most at time $t = T$. If the bandwidth of $\tilde{f}(t)$ is BW , then $\tilde{f}(t)$ does not change appreciably for time differences much less than $\frac{1}{BW}$. Therefore, if

or

to

at

20

1

1

$$\frac{2VT}{C} \ll \frac{1}{BW}$$

or

$$BW \cdot T \ll \frac{C}{2V}$$

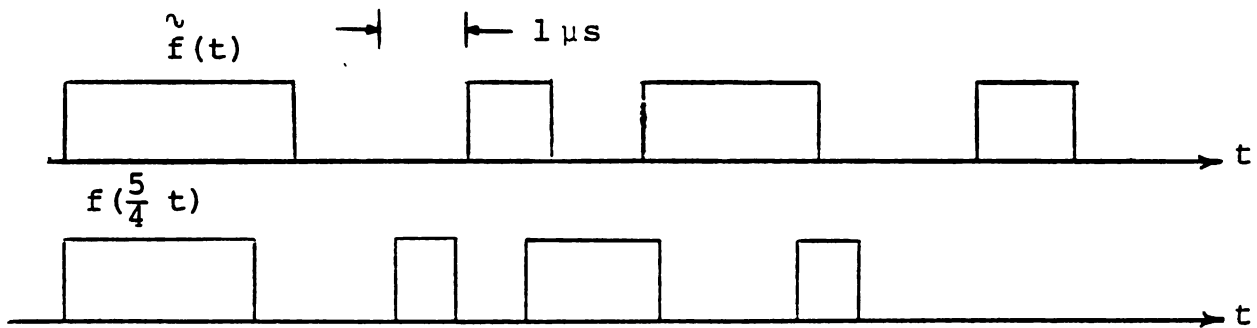
G.4

Then

$$f(t) \approx f[(1 + \alpha(\omega))t]$$

and the Doppler approximation is valid.

The significance of this criterion when applied to pseudorandom binary phase signals is particularly interesting.



Here

$$\alpha = \frac{1}{4} = \frac{2V}{C}$$

$$T_B \approx 1 \mu s \Rightarrow BW \approx \frac{1}{10^{-6}} = 1 \text{ Mhz}$$

Figure G1. Example of Compression in Binary Phase Signals

In this example,

$$BW \cdot T \ll \frac{1}{\alpha} = 4 \Rightarrow T \ll 4 \mu s$$

That is, for the Doppler approximation to be valid, T must be much less than $4 \mu s$.

In general, for binary phase modulated phase signals, if the bit period for the transmitted signal is T_B , then the bit period for the received signal is

$$\frac{1}{1+\alpha} T_B \tag{G.5}$$

The difference is:

$$T_B - \frac{1}{1+\alpha} T_B = T_B \left(\frac{\alpha}{1+\alpha} \right) \tag{G.6}$$

At the end of N bit periods, $\tilde{f}(t)$ and $\tilde{f}((1+\alpha)t)$ would differ by:

$$N \cdot T_B \left(\frac{\alpha}{1+\alpha} \right) \text{ seconds} \tag{G.7}$$

for a difference of 1 bit period,

$$N \cdot T_B \left(\frac{\alpha}{1+\alpha} \right) = T_B \tag{G.8}$$

Solving for N,

$$N = \frac{1+\alpha}{\alpha} \quad \text{G.9}$$

Thus, for $f(t)$ to remain nearly inphase with $f((1+\alpha)t)$, the constraint on N is

$$N \ll \frac{1+\alpha}{\alpha} \quad \text{G.10}$$

The following argument shows that this intuitively derived constraint for B phase signals is consistent with the criterion required for the Doppler approximation to be valid.

$$T_B N = T \ll T_B \frac{1+\alpha}{\alpha} \quad \text{G.11}$$

$$T \ll \frac{1}{BW} \frac{1 + \frac{2V}{C}}{\frac{2V}{C}} \quad \text{G.12}$$

$$BW \cdot T \ll \frac{C+2V}{2V} = \frac{C}{2V} + 1 \quad \text{G.13}$$

But it was previously assumed that

$$\frac{C}{2V} \gg 1$$

And, as anticipated,

$$BW \cdot T \ll \left(\frac{C}{2V}\right) \quad \text{G.14}$$

Thus, equation G.10 is consistent with our previous result and provides interesting insight into applying the Doppler approximation to B phase code modulated waveforms.

Ambiguity Function

If it can be assumed that the Doppler approximation is valid (for most of the signals employed in this research it cannot), then

$$\tilde{r}(t) = \tilde{b}\sqrt{E_t} \tilde{f}(t-\tau) e^{j\omega_d t} + \tilde{w}(t) \quad G.15$$

and

$$\theta(\tau, \omega) = \left| \int_{-\infty}^{\infty} \tilde{f}(t-\tau_a) \tilde{f}^*(t-\tau) e^{j(\omega_a - \omega)t} dt \right|^2 \quad G.16$$

Let

$$t' = t - \tau_a \quad t = t' + \tau_a$$

$$\omega' = \omega_a - \omega \quad Z = \tau_a - \tau$$

$$\begin{aligned} \theta(Z, \omega') &= \left| \int_{-\infty}^{\infty} \tilde{f}(t') \tilde{f}^*(t'+Z) e^{j\omega' t'} dt' \right|^2 \\ &= \left| \phi(Z, \omega') \right|^2 \end{aligned} \quad G.17$$

Using more conventional variables

$$\tilde{\phi}(\tau, \omega) \triangleq \int_{-\infty}^{\infty} \tilde{f}(t) \tilde{f}^*(t-\tau) e^{j\omega t} dt \quad \text{G.18}$$

$\phi(\tau, \omega)$ is the time frequency auto correlation function and $\theta(\tau, \omega)$ is the conventional ambiguity function.

$$\theta(\tau, \omega) = |\tilde{\phi}(\tau, \omega)|^2 \quad \text{G.19}$$

Even though the Doppler approximation is not strictly valid for many of the signals and physical situations of importance in this research, studying and being very familiar with $\theta(\tau, \omega)$ will provide valuable insight into fundamental limitations of a blood flow imaging system as well as providing guidance in choosing an appropriately transmitted signal.

Many properties of $\theta(\tau, \omega)$ have been derived. However, only six of the most useful ones will be listed.

$$\begin{aligned} 1. \quad \tilde{\phi}(0, \omega) &= \int_{-\infty}^{\infty} \tilde{f}(t) \tilde{f}^*(t) e^{j\omega t} dt = F\{|f(t)|^2\} \\ &= \text{Fourier transform of the squared} \\ &\quad \text{magnitude of the envelope} \end{aligned}$$

$$\begin{aligned}
 2. \quad \tilde{\phi}(\tau, 0) &= \int_{-\infty}^{\infty} \tilde{f}(t) \tilde{f}^*(t+\tau) dt \\
 &= \text{auto correlation of } \tilde{f}(t)
 \end{aligned}$$

$$3. \quad \theta(0, 0) = \phi(0, 0) = 1$$

$$4. \quad \int_{-\infty}^{\infty} \int_{-\infty}^{\infty} \theta(\tau, f) df d\tau = \int \int \theta(\tau, w) d\tau \frac{dw}{2\pi} = 1$$

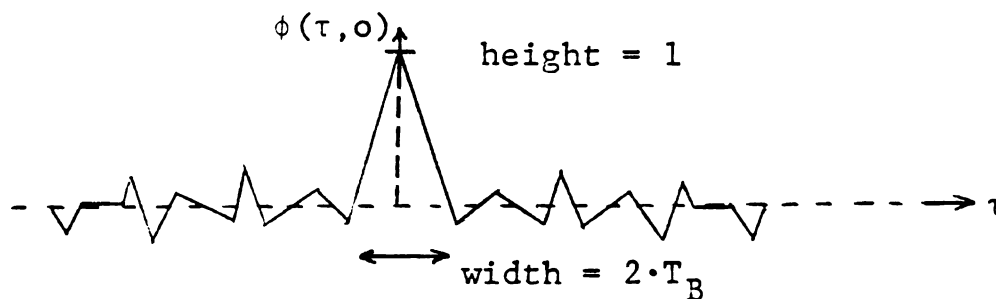
$$5. \quad \int_{-\infty}^{\infty} \theta(\tau, f) d\tau = \int_{-\infty}^{\infty} \theta(\tau, 0) e^{-j2\pi f\tau} d\tau$$

$$6. \quad \int_{-\infty}^{\infty} \theta(\tau, f) df = \int_{-\infty}^{\infty} \theta(0, f) e^{j2\pi f\tau} df$$

As an example, these properties will be used to investigate the shape of $\theta(\tau, w)$ for a pseudorandom binary phase sequence.

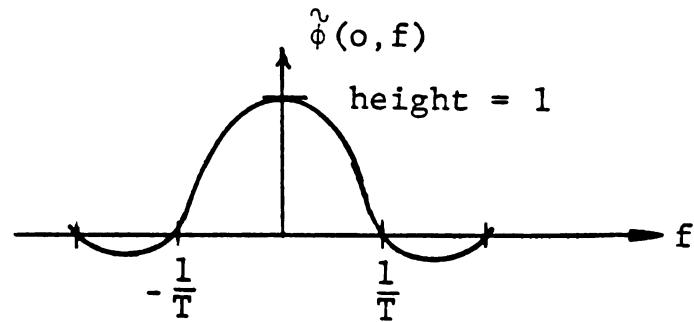
a. Along the $f = 0$ axis (Property 2)

$$\tilde{\phi}(\tau, 0) = \int \tilde{f}(t) \tilde{f}^*(t+\tau) dt$$



b. Along the $\tau = 0$ axis (Property 1)

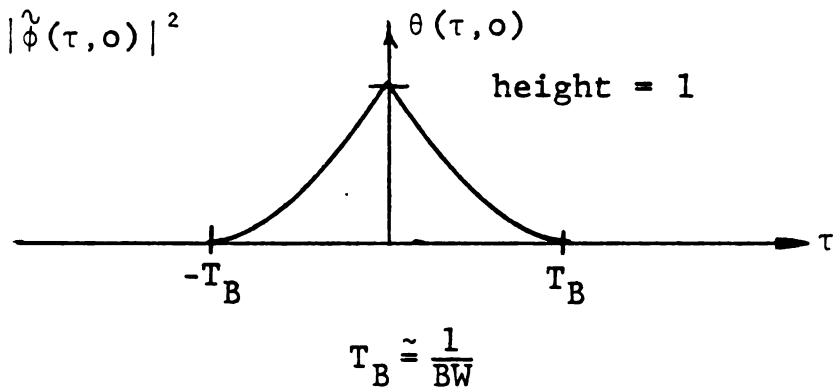
$$\tilde{\phi}(0, f) = F\{\tilde{f}(t)|^2\} = \text{sinc}(Tf)$$



$$\theta(\tau, f) = |\tilde{\phi}(\tau, f)|^2$$

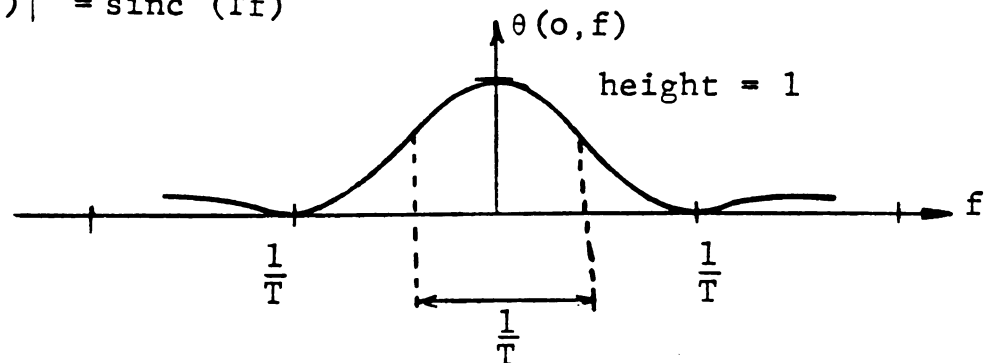
For a pseudorandom sequence:

$$\theta(\tau, 0) = |\tilde{\phi}(\tau, 0)|^2$$



where BW is the one-sided bandwidth in hertz.

$$\theta(0, f) = |\theta(0, f)|^2 = \text{sinc}^2(Tf)$$



Also, the average width of the central spike of $\theta(o, f)$ is approximately $1/2T$ while the average width of $\theta(\tau, o)$ is $1/2 BW$.

$$\theta(o, \frac{1}{4T}) = .81$$

$$\theta(\frac{1}{4BW}, o) = .66$$

Therefore, it appears that a system using a binary phase sequence as the transmitted signal can "resolve" targets separated in delay by approximately $\frac{1}{BW}$ or in Doppler by approximately $\frac{1}{T}$. These results are approximately true for all transmitted signals and a typical ambiguity function takes on the approximate shape and dimensions shown in Figure G2.

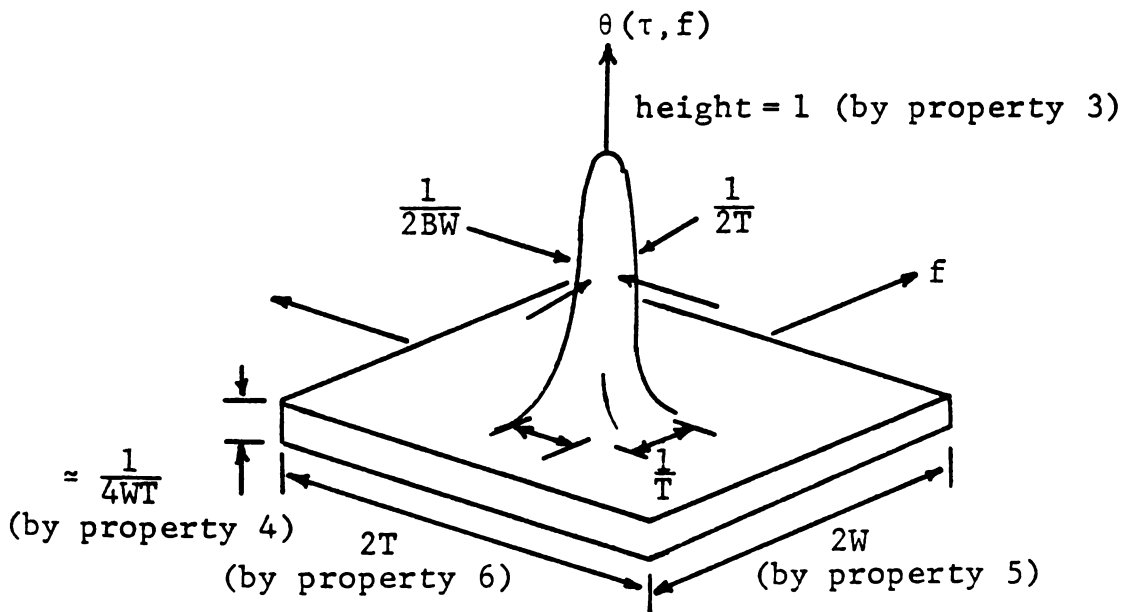


Figure G2. Approximate General Ambiguity Surface

It is important to emphasize that the ambiguity function shown in Figure G2 represents the response of a conventional correlation receiver to a point target mismatched in delay and Doppler under noiseless conditions when the Doppler approximation is valid. When the Doppler approximation is not valid and a conventional correlation receiver is used, then the ambiguity function may not be a reasonable measure of the signal's ability to resolve targets. However, if a true correlation receiver is used as previously described, and if $\alpha(\omega)$ is small for all expected target velocities (which is the case with blood flow imaging), then the assertion is made that the conventional ambiguity function still provides a valid measure of the signal's range resolving capability. The reasonableness of this assertion is made by the following argument.

Along the $\omega = 0$ axis, that is, when $\omega_a = \omega$, from equations G.2 and G.3, the output of the true correlation receiver in the absence of noise may be written as:

$$|L(\tau, 0)|^2 = \left| \int_{-\infty}^{\infty} \tilde{f}[(1+\alpha)t - \tau_a] f^*[(1+\alpha)t - \tau] dt \right|^2 \quad \text{G.20}$$

Equation G.20 describes the autocorrelation of $\tilde{f}[(1+\alpha)t]$. Clearly, if $\alpha \ll 1$, then the bandwidth of $\tilde{f}(t)$ is approximately the bandwidth of $\tilde{f}[(1+\alpha)t]$. Thus, the ability of the true correlation receiver to resolve targets separated in

init

vent

the

rec

mit

or

be

initial delay is nearly identical to that given by the conventional ambiguity function.

Unfortunately, the same assertion cannot be made for the Doppler resolving capability of a true correlation receiver without considering the specific signal to be transmitted. The Doppler resolving capability of specific signals or classes of signals using true correlation processing must be dealt with on an individual basis.

wit

wav

of

com

per

th

tw

in

pr

wa

d

i

s

v

a

n

APPENDIX H

Acoustic Wave Propagation

The purpose of this appendix is to familiarize the reader with the terms and equations used to describe simple acoustic wave propagation. It is not intended as a rigorous treatment of physical acoustics and the reader interested in a more complete treatment should consult an appropriate text.

The discussion will start by considering propagation in perfectly homogeneous, lossless material. Homogeneous implies that all macroscopic physical attributes associated with any two differential volume elements are identical. Lossless implies that the material simply supports acoustic wave propagation and does not extract energy from that acoustic wave (i.e., the presence of acoustic waves in the material does not raise its temperature). This is certainly an idealized material which does not exist in reality. However, studying wave propagation in such a simple media provides valuable insight into propagation in more complex media such as tissue.

The propagation of acoustic waves in lossless, isotropic media may be described by

$$\frac{\partial^2 \bar{\zeta}}{\partial t^2} = \frac{K + \frac{4}{3} G}{\rho_0} \nabla \nabla \cdot \bar{\zeta} - G \nabla \cdot \nabla \cdot \bar{\zeta} \quad \text{H.1}$$

where

$$\begin{aligned} K &= \text{adiabatic bulk modules } \Delta V \frac{dp}{dv} \\ G &= \text{modules of sheer rigidity} \\ \rho_0 &= \text{average density of the media} \\ \bar{\zeta} &= \text{instantaneous displacement} \end{aligned}$$

For fluids, the modulus of sheer rigidity, G , equals **zero**. Since tissue (including blood) is composed largely **of** water, it will be assumed that the body cannot support **sheer** waves. Thus, the vector wave equation for displacement **becomes**:

$$\frac{\partial^2 \bar{\zeta}}{\partial t^2} = \frac{K}{\rho_0} \nabla \nabla \cdot \bar{\zeta} \quad \text{H.2}$$

In one dimension, this wave equation reduces to

$$\frac{\partial^2 \zeta}{\partial t^2} = \frac{1}{\rho_0 \beta_s} \frac{\partial^2 \zeta}{\partial x^2} \quad \text{H.3}$$

Where the parameter β_s , has been introduced. By definition β_s is the adiabatic compressability of the medium, which is the reciprocal of K , the bulk modulus. The velocity of a plane wave satisfying equation H.3 is well known to be

$$V = \frac{1}{\sqrt{\rho_o \beta_s}} \quad \text{H.4}$$

If the coordinate origin is chosen appropriately, the solution to H.3 takes the form

$$\zeta = \zeta_{\max} \cos(kx - \omega t) \quad \text{H.5}$$

$$k = \frac{2\pi}{\lambda} = \frac{\omega}{V}$$

The bulk modulus, K , is a constant which relates the fractional change in volume to the applied pressure.

$$p = -K \frac{\Delta \text{Volume}}{\text{Volume}} \quad \text{H.6}$$

For plane wave propagation, as described by equation H.5, equation H.6 reduces to (using $\Delta \text{Volume} = dy \cdot dz \cdot d\zeta$; $\text{Volume} = dy \cdot dz \cdot dx$)

$$p = -K \frac{d\zeta}{dx} \quad \text{H.7}$$

Using equation H.5, it is seen that there exists a propagating pressure wave in spatial quadrature with the propagating displacement wave.

$$p = -K \frac{d\zeta}{dx} = p_{\max} \sin(kx - \omega t) \quad \text{H.8}$$

where

$$p_{\max} = K k \zeta_{\max} = \omega \rho_o V \zeta_{\max} \quad \text{H.9}$$

The time derivative of H.5 yields

$$\dot{\zeta} = \dot{\zeta}_{\max} \sin(kx - \omega t) \quad \text{H.10}$$

$$\dot{\zeta}_{\max} = \omega \zeta_{\max}$$

Also, it is seen that $\dot{\zeta}$ and p are related as follows

$$p = \rho_o V \dot{\zeta} \quad \text{H.11}$$

$$p_{\max} = \rho_o V \dot{\zeta}_{\max}$$

Additionally, the wave intensity I is defined as the time average acoustic wave power per unit area and is related to $\dot{\zeta}_{\max}$ and p_{\max} as

$$I = \frac{\dot{\zeta}_{\max} p_{\max}}{2} \quad \text{H.12}$$

$$I = \frac{\dot{\zeta}_{\max}^2 \rho_o V}{2} \quad \text{H.13}$$

$$I = \frac{p_{\max}^2}{2 \rho_o V} \quad \text{H.14}$$

Thus, an analogy exists between the electric field \bar{E} and pressure p , between the magnetic field intensity \bar{H} and time rate of displacement $\dot{\zeta}$, and between the characteristic wave impedance Z_0 and $\rho_0 V$. In fact, if the identification is made,

$$Z = \rho_0 V \quad \text{H.15}$$

the analogy continues. At the interface of two dissimilar tissue types, the reflection coefficient is defined as

$$R = \frac{Z_1 - Z_2}{Z_1 + Z_2} \quad \text{H.16}$$

The reflection coefficient in equation H.16 is the ratio of p_{\max} of the wave reflected from the tissue discontinuity to p_{\max} of the incident wave. The reflected intensity is

$$I_{\text{reflected}} = R^2 I_{\text{incident}} \quad \text{H.17}$$

while the transmitted intensity equals

$$\begin{aligned} I_{\text{transmitted}} &= (I_{\text{incident}} - I_{\text{reflected}}) \\ &= \frac{Z_1}{Z_2} T^2 I_{\text{incident}} \end{aligned} \quad \text{H.18}$$

where

$$T = \frac{2Z_2}{Z_1 + Z_2} \quad \text{H.19}$$

and is the ratio of p_{\max} of the transmitted wave to p_{\max} of the incident wave.

In most biological tissues, ρ_o is nearly constant so that the reflection coefficient R reduces to

$$R = \rho_o \frac{V_1 - V_2}{V_1 + V_2} \quad \text{H.20}$$

The reflection of acoustic energy at a material interface may be minimized by sandwiching a third layer between the two media.

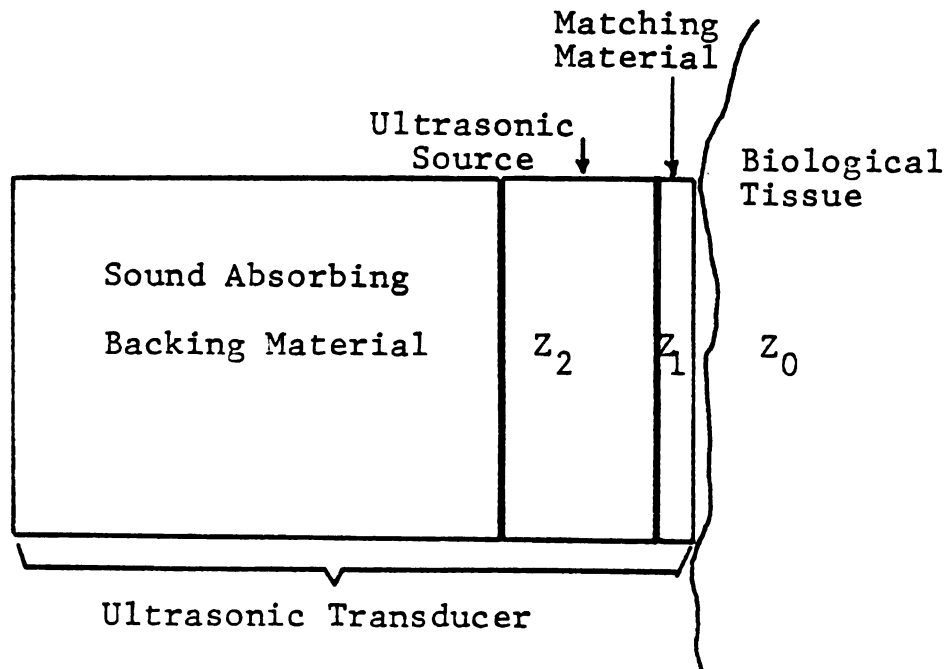


Figure H1. One Quarter Wave Matching Layer

One area where quarter wave matching is used extensively is to maximize energy transfer between the ultrasonic transducer and biological tissue as shown in Figure H1. If the characteristic impedance of the matching material Z_1 is between Z_0 and Z_2 , then the optimum width of the matching layer is one quarter wavelength. In addition, if Z_1 may be selected such that $Z_1 = \sqrt{Z_2 Z_0}$, then there will be 100% transmission of acoustical energy.

APPENDIX I

Blood Flow in Cylindrical Vessels

Figure I1 shows a length of cylindrical vessel and a cylindrical subsection of that vessel. The pressures of interest exerted on this cylindrical subsection are the sheer stress and fluid pressure at either end of the cylinder, as shown.

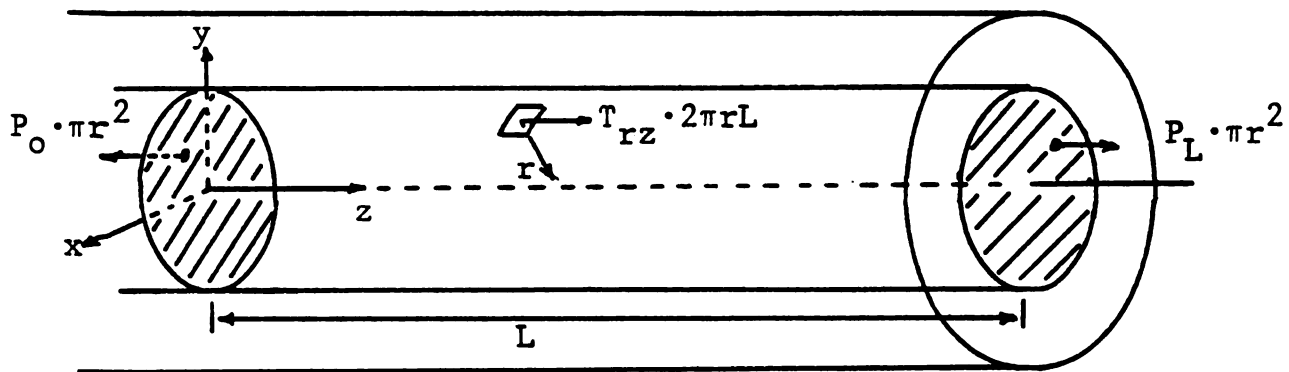


Figure I1. Section of Cylindrical Vessel

In the steady state, the sum of the forces acting on the subsection must equal zero. Thus,

$$P_O \pi r^2 - P_L \pi r^2 - T_{rz} 2\pi r L = 0 \quad \text{I.1}$$

where the sheer stress T_{rz} is the z-directed sheer force per unit area exerted by the fluid at r on the fluid at $r + dr$.

Solving equation I.1 for T_{rz} results in the relationship shown in equation I.2.

$$T_{rz} = \frac{P_o - P_1}{2L} r \quad \text{I.2}$$

Substituting for T_{rz} by using the defining relation for the viscosity μ of a Newtonian fluid given in equation I.3 results in a differential equation for the velocity of the fluid in the vessel as shown in equation I.4.

$$T_{rz} = -\mu \frac{\partial V_z}{\partial r} \quad \text{I.3}$$

$$\frac{dV_z}{dr} = - \frac{(P_o - P_1)}{2\mu L} r \quad \text{I.4}$$

The solution to equation I.4 is given as

$$V_z = K - \frac{P_o - P_1}{2\mu L} r^2 \quad \text{I.5}$$

By applying the boundary condition at the vessel wall, namely that the fluid velocity is zero at $r = a$, the unknown constant may be determined and equation I.5 reduces to equation I.6.

$$V_z(r) = - \frac{(P_o - P_1)}{4\mu L} (r^2 - a^2) \quad \text{I.6}$$

Also, by identifying the velocity at the center of the vessel as the maximum velocity, V_{\max} , equation I.6 may be further simplified.

$$V_z(r) = V_{\max} \left[1 - \left(\frac{r}{a} \right)^2 \right] \quad \text{I.7}$$

where

$$V_{\max} = \frac{a^2 (P_o - P_l)}{4\mu L} \quad \text{I.8}$$

The total volume flow rate, Q , is easily found by integrating the differential flow rate over the vessel cross section as follows:

$$\begin{aligned} Q &= \int_s \bar{V} \cdot \bar{ds} \\ &= \int_0^R \int_0^{2\pi} V_{\max} \left(1 - \frac{r^2}{a^2} \right) r dr d\theta \end{aligned} \quad \text{I.9}$$

Therefore,

$$Q = \frac{\pi a^2 V_{\max}}{2} \quad \text{I.10}$$

And finally, the average blood velocity is determined by dividing the total volume flow rate by the cross sectional area of the vessel.

$$V_{\text{avg}} = \frac{Q}{\pi a^2} = \frac{V_{\max}}{2} \quad \text{I.11}$$

APPENDIX J

Computation of the Elements of A

A symmetric unit energy periodic pulse train is assumed to be the transmitted signal.

$$\tilde{f}(t) = \sqrt{\frac{T_P}{T \cdot T_B}} \sum_{M=-\frac{T}{2T_P}}^{\frac{T}{2T_P}} \pi\left(\frac{t - MT_P}{T_B}\right) \quad J.1$$

For every α_{ij} , there will be a computation which takes the form of

$$\alpha \sim \frac{T_P}{T \cdot T_B} \int_{-\frac{T}{2}}^{\frac{T}{2}} g(\omega_n u) h(\omega_m u) \sum_M \pi\left(\frac{u - kT_P}{T_B}\right) dt \quad J.2$$

$$\omega_n = \frac{\pi n}{NT}$$

where $g(\cdot)$ and $h(\cdot)$ are either $\sin(\cdot)$ or $\cos(\cdot)$. Now, since $T_P \ll \frac{2T}{n}$, the effect of the pulse train is to sample the product $g(\omega_n)h(\omega_m u)$. That is,

$$\alpha \sim \sum_k g(\omega_n kT_P) h(\omega_m kT_P) T_B \cdot \frac{T_P}{T \cdot T_B} \quad J.3$$

Because $T_p \ll \frac{2\pi}{\omega_n}$ this summation may be approximated as an integral in the following manner.

Since

$$\sum_{k=-\frac{T}{2}}^{\frac{T}{2}} g(\omega_n u) h(\omega_m u) du \approx \sum_k g(\omega_n k T_p) h(\omega_m k T_p) T_p \quad J.4$$

then

$$\alpha \approx \frac{1}{T} \int_{-\frac{T}{2}}^{\frac{T}{2}} g(\omega_n u) h(\omega_m u) du \quad J.5$$

With this approximation, the computation of the elements of A is straightforward.

1. α_{11}

$$\alpha_{ij} = \frac{T_B}{T_P} \frac{1}{T} \int_{-\frac{T}{2}}^{\frac{T}{2}} a_o^k du = a_o^k \quad J.6$$

2. $\alpha_{1,2n}$

$$\begin{aligned} \alpha_{1,2n} &= k \sqrt{a_o a_n} \cdot \frac{1}{T} \int_{-\frac{T}{2}}^{\frac{T}{2}} \cos \left(\frac{n\pi}{NT} u \right) du \\ &= \frac{2k \sqrt{a_o a_n}}{T} \cdot \frac{NT}{n\pi} \left[\sin \left(\frac{n\pi}{NT} u \right) \right]_0^{\frac{T}{2}} \\ \alpha_{1,2n} &= \frac{2Nk \sqrt{a_o a_n}}{n\pi} \sin \left(\frac{n\pi}{2N} \right) \end{aligned} \quad J.7$$

$$3. \quad \alpha_{1, 2n+1}$$

$$\alpha_{1, 2n+1} = 0 \quad \text{J.8}$$

$$4. \quad \alpha_{2n, 2n}$$

$$\begin{aligned} \alpha_{2n, 2n} &= k a_n \frac{2}{T} \int_0^{\frac{T}{2}} \cos^2 \left(\frac{n\pi}{NT} u \right) du \\ &= k a_n \frac{2}{T} \cdot \frac{NT}{n\pi} \left[\frac{1}{2} x + \frac{1}{4} \sin 2x \right]_0^{\frac{n\pi}{2N}} \\ \alpha_{2n, 2n} &= \frac{2Nk a_n}{n} \left[\frac{n}{4N} + \frac{1}{4} \sin \left(\frac{n\pi}{N} \right) \right] \quad \text{J.9} \end{aligned}$$

$$5. \quad \alpha_{2n+1, 2n+1}$$

$$\begin{aligned} \alpha_{2n+1, 2n+1} &= k a_n \frac{2}{T} \int_0^{\frac{T}{2}} \sin \left(\frac{n\pi}{NT} u \right) du \\ \alpha_{2n+1, 2n+1} &= \frac{2Nk a_n}{n\pi} \left[\frac{n\pi}{4N} - \frac{1}{4} \sin \left(\frac{n\pi}{N} \right) \right] \quad \text{J.10} \end{aligned}$$

$$6. \quad \alpha_{2n, 2m}$$

$$\begin{aligned} \alpha_{2n, 2m} &= k \sqrt{a_n a_m} \frac{2}{T} \int_0^{\frac{T}{2}} \cos \left(\frac{n\pi}{NT} u \right) \cos \left(\frac{m\pi}{NT} u \right) du \\ &= k \sqrt{a_n a_m} \frac{1}{T} \int_0^{\frac{T}{2}} \cos \left(\frac{(n+m)\pi}{NT} u \right) + \cos \left(\frac{(n-m)\pi}{NT} u \right) du \end{aligned}$$

$$\begin{aligned}
&= k\sqrt{a_n a_m} \left[\frac{N}{(n+m)\pi} \sin\left(\frac{(n+m)\pi}{2N}\right) + \frac{N}{(n-m)\pi} \sin\left(\frac{(n-m)\pi}{2N}\right) \right] \\
\alpha_{2n, 2m} &= k\sqrt{a_n a_m} \frac{N}{\pi} \frac{\sin\left(\frac{(n+m)\pi}{2N}\right)}{n+m} + \frac{\sin\left(\frac{(n-m)\pi}{2N}\right)}{n-m} \quad \text{J.11}
\end{aligned}$$

$$7. \quad \alpha_{2n+1, 2m+1}$$

$$\begin{aligned}
\alpha_{2n+1, 2m+1} &= k\sqrt{a_n a_m} \frac{2}{T} \int_0^{\frac{T}{2}} \sin\left(\frac{n\pi}{NT}u\right) \sin\left(\frac{m\pi}{NT}u\right) du \\
&= k\sqrt{a_n a_m} \frac{1}{T} \int_0^T \cos\left(\frac{(n-m)\pi}{NT}u\right) - \cos\left(\frac{(n+m)\pi}{NT}u\right) du \\
\alpha_{2n+1, 2m+1} &= k\sqrt{a_n a_m} \frac{N}{\pi} \frac{\sin\left(\frac{(n-m)\pi}{2N}\right)}{n-m} - \frac{\sin\left(\frac{(n+m)\pi}{2N}\right)}{n+m} \quad \text{J.12}
\end{aligned}$$

$$8. \quad \alpha_{2n+1, 1} = \alpha_{1, 2n+1}$$

$$9. \quad \alpha_{2n, 1} = \alpha_{1, 2n+1}$$

$$10. \quad \alpha_{2n, 2mk} = 0$$

$$11. \quad \alpha_{2n+1, 2m} = 0$$

LIST OF REFERENCES

LIST OF REFERENCES

1. Franklin, D.L., "Techniques for measurement of blood flow through intact vessels," Med. Electron. Biol. Engrg. 3, 27-37, Pergamon Press (1965). Printed in Great Britain.
2. Wells, P. N. T. "Physical principles of ultrasonic diagnosis," Academic Press, London (1969).
3. Baker, D.W., "Pulsed ultrasonic Doppler blood-flow sensing," IEEE Trans. on Sonics and Ultrasonics, SU-17, 3, 170-185 (July 1970).
4. Peronneau, P. A. and F. Leger, "Doppler ultrasonic pulsed blood flowmeters," 86th Intl. Conf. on Medical and Biological Engineering, Chicago (1969).
5. McLeod, F. D. and M. Anliker, "Multiple gate pulse Doppler flowmeter," IEEE Ultrasonic Symposium (1971).
6. Gould, K. L, D. J. Mozersky, D. E. Hokanson, D. W. Baker, J. W. Kennedy, D. S. Summer and D. E. Strandness, Jr., "A non-invasive technic for determining patency of saphenous vein coronary bypass grafts, "Circulation XLVI, 595-600 (September 1972).
7. Haase, W. C., W. S. Foletta and J. D. Meindl, "A directional ratiometric ultrasonic blood flowmeter, IEEE Ultrasonic Symposium (November 1973).
8. Hottinger, C. F. and J. D. Meindl, "An ultrasonic scanning system for arterial imaging, "IEEE Ultrasonic Symposium (November 1973).
9. Erikson, K. R., F. J. Fry, and J. P. Jones, "Ultrasound in Medicine--A Review, "IEEE Trans. on Sonics and Ultrasonics SU-21, 3, 144-170 (July 1974).
10. Kalmus, H. P., "Electronic flowmeter system, "Rev. Scient. Instrum., 25, 201-206 (1954).
11. Haugen, M. G., W. R. Farral, J. F. Herrick and G. J. Baldes, "An ultrasonic flowmeter," Proc. Nat. Electron. Conf., II, 465-475 (1955).

12. Baldes, G. J., W. R. Farral, M. C. Haugen and J. F. Herrick, "A forum on an ultrasonic method for measuring the velocity of blood," pp. 1675-1676 in Ultrasound in Biology and Medicine (ed. E. Kelly) A.I.B.S., Washington (1957).
13. Franklin, D. L., D. W. Baker, E. M. Ellis and R. F. Rushmer, "A pulsed ultrasonic flowmeter," I.R.E. Trans., Med. Electron. Me-6, 204-206 (1959).
14. Franklin, D. L., D. W. Baker and R. F. Rushmer, "Pulsed ultrasonic transit time flowmeter," Ins. Rad. Engrs. Trans. Bio-Med. Electron., BME-9, 44-49.
15. Farrall, W. R., "Design considerations for ultrasonic flowmeters," I.R.E. Trans. Med. Electron. ME-6, 198-201 (1959).
16. Zernstroff, W. D., C. A. Castillo, C. W. Crumpton, "A phase shift ultrasonic flowmeter," Inst. Rad. Engrs. Trans. Bio-Med. Electron., BME-9, 199 (1962).
17. Nobel, F. W., T. C. Goldsmith, C. J. Waldsburger and T. E. Cook, "A new system for measurement of blood flow by ultrasonics," Digest of 15th Conf. on Engrg. in Med. and Biol., Chicago (1962).
18. Wetterer, E., "A critical appraisal of methods of blood flow determination in animals and man," I.R.E. Trans. Med. Electron. ME-9, 165-173 (1962).
19. Arts, M. G. J. and J. M. Roelvors, "On the instantaneous measurment of blood flow by ultrasonic means," Med. and Biol. Engrg. 10, 232-34 (1972).
20. Satomura, S., "Study of the flow pattern in peripheral arteries by ultrasonics," J. Acoust. Soc., Japan, 15, 151-158 (1959).
21. Franklin, D. L., W. A. Schlegel and R. F. Rushmer, "Blood flow measured by Doppler frequency shift of back-scattered ultrasound," Science 132, 564-565 (1961).
22. Baker, D. W., et al., "A sonic transcutaneous blood flowmeter," Proc 17th Am. Conf. on Engrg. Med. Biol., 76 (1964).
23. McLeod, F. D., "A Doppler ultrasonic physiological flowmeter," Proc. 17th Am. Conf. on Engrg. Med. Biol., 81 (1964).

24. McLeod, F. D., "A directional Doppler flowmeter,"
Digest of the 7th Conf. Med. Biol. Engrg.,
Stockholm, Sweden (1967).
25. Newhouse, V. L., G. Cooper, H. Feigenbaum, C. P. Jethwa
and M. Kaveh, "Ultrasonic blood velocity measurement
using random signal correlation techniques," 10th
Intl. Conf. on Medical and Biological Engineering
(invited), Dresden, Germany (August 1973).
26. Jethwa, C. P., M. Kaveh, G. Cooper and F. Saggio, "Blood
flow measurements using ultrasonic pulsed random
signal Doppler system," IEEE Trans. on Sonics and
Ultrasonics, SU-22, No. 1 (January 1975).
27. Barber, F, D. W. Baker, A.W.C. Nation, D. E. Stradness
and J. M. Reid, "Ultrasonic Duplex Scanner, IEEE
Trans. on Biomed. Eng. (March 1974).
28. Dunn, F, "Ultrasonic Attenuation, Absorption, and Velocity
in Tussue and Organs", Proceedings of the Seminar on
Ultrasonic Tissue Characterization, Gaithersburg, MD,
NBS Special Publication Number 453 (May 28-30, 1975).
29. Kak, A.C, and K. A. Dines, "Signal Processing of Broadband
Pulsed Ultrasound: Measurement of Attenuation of
Soft Biological Tissues", IEEE Trans. on Biomedical
Engineering, Vol. BME-25, No. 4, pp. 321-344 (July 1978).
30. Reid, J. M., R. A. Sieglemann, M. Nasser and D. W. Baker,
"The Scattering of Ultrasound by Human Blood", ICEMB,
(Chicago, ILL, 1969).
31. Milner W., "Cardiovascular System", in Medical Physiology,
ed. by V. B. Mountcastle, C. V. Mosby Co., St. Louis,
p. 840 (1974).
32. Milner, W., "Principles of Hemodynamics", in Medical
Physiology, ed. by V. B. Mountcastle, C. V. Mosby Co.,
St. Louis, p. 914 (1974).
33. Coulter, N. A. Jr., and J. R. Papenheimer, "Development
of Turbulence in Flowing Blood", Am. J. Physicol.
159: 401 (1941).
34. Shung, K. K., R. A. Sieglemann and J. M. Reid, "The
Scattering of Ultrasound by Red Blood Cells", ~~Proceed-~~
ings of the Seminar on Ultrasonic Tissue Character-
ization, Gaithersburg, MD, NBS Publication No. 453.
(May 28-30, 1975).

35. Bennet, W. R., "Distribution of the Sum of Randomly Phased Components", Quart. J. Appl. Math. 5, 385-393 (Jan., 1948).
36. Cooper, G. R. and R. J. Purdy, "Detection, Resolution and Accuracy in the Random Signal Radar", TR-EE68-16, Purdue University School of Electrical Engineering, (August 1968).
37. VanTrees, H. L., Detection, Estimation and Modulation Theory, Part 3, Wiley Publishing Co, P. 321.
38. Jethwa, C. P. and M. D. Olinger, "Blood Flow Detection by Ultrasonic Random Signal Doppler Flowmeter", Twenty Seventh Annual Conference on Engineering in Medicine and Biology, Philadelphia, PA (October 1974).
39. Siegel, M., B.Ho and M. Olinger, "Velocity Profiles in the Presence of Obstructions using a Random Noise Ultrasonic Blood Flowmeter", Ultrasonic Symposium, (1975).
40. Woollett, R. S., "Transducer Comparison Methods based on the Electromechanical Coupling Coefficient Concept", I.R.E. National Convention Record, Part 9, pp. 23-27, (1957).
41. Thurston, F. L. and O. J. VonRamm, "Electronic Beam Steering for Ultrasonic Imaging", in Ultrasound in Medicine, ed. by M. deVlieger, D. N. White and V. R. McCready, American Elsevier Publishing Co., Inc., New York, pp. 304-308, (1974).
42. Kossoff, G., D. E. Robinson and W. J. Garrett, "Ultrasonic Two Dimensional Visualization for Medical Diagnosis", J. A. S. A., 44, pp. 1310-1318, (1968).
43. Kossoff, G., "Design of Narrow-Beamwidth Transducers", J. A. S. A, 35, (1963).
44. Winder, A. A., "Sonar System Technology", IEEE Trans. on Sonics and Ultrasonics, pp. 291-332, (September 1975).

GENERAL REFERENCES

GENERAL REFERENCES

1. VanTrees, H. L., Detection, Estimation and Modulation Theory, Parts 1 and 3, Wiley Publishing Co., Inc.
2. Dunn, F., P. Edwards and W. J. Fry, "Absorption and Dispersion of Ultrasound in Biological Media", in Biological Engineering, ed. by H. P. Schwan, (Inter-University Electronics Ser.) McGraw Hill Publishing Co. (1969).
3. Rihaczek, A. W., "Radar Signal Design for Target Resolution", Proc. IEEE, pp. 116-128, (February 1965).
4. Reid, J. M., "The Scattering of Ultrasound by Tissues", Proceeding of the Seminar on Ultrasonic Tissue Characterization, Gaithersburg, MD, NBS Publication No. 453 (may 28-30, 1975).
5. Woodward, P. M., Probability and Information Theory, with Application to Radar, Pergamon Press, The MacMillan Co., New York.